



DISSERTATION 2017-18

□□□□□□□□ □□□□□□ □□

PREPARATION AND CHARACTERIZATION OF A NOVAL THERMOLUMINESCENT PHOSPHOR $\text{KCaPO}_4:\text{Dy}$ FOR RADIATION DETECTION.

By:

Mr. Ravi Kumar meena

B.Sc.(Hons.) Physics- IIIrd Year

Roll No.- 15079567068

Sri Venkateswara College, Delhi University.

Under the Supervision of

Dr. Anant Pandey

Assistant Professor, Department of Physics

Sri Venkateswara College, University of Delhi.

CONTENTS:



Purpose of the work.





Effect of holmium doping on structural, electrical and piezoelectric properties of lead-free (Ba,Ca)(Ti,Sn)O₃ ceramics

Chitra¹ · Radhapiyari Laishram² · Aditi Vashishtha¹ · Mukesh Kumar Singh¹ · Kamal Kant Chandra¹ · K. Chandramani Singh¹

Received: 6 October 2018 / Accepted: 3 January 2019
© Springer Science+Business Media, LLC, part of Springer Nature 2019

Abstract

Lead-free (Ba_{0.91}Ca_{0.09}Sn_{0.07}Ti_{0.93})O₃ (BCST) ceramics, doped with holmium (Ho) in the range 0–1.0 mol%, were synthesized using conventional solid-state sintering method. XRD analyses of these ceramic samples confirm single phase pure perovskite structure. Evidence of Ho³⁺ substituting Ba²⁺ via electronic charge compensation exists in the range 0–0.4 mol%, while ionic charge compensation mechanism dominates beyond 0.4 mol%. Crystallite size and lattice strain undergo systematic change, while the room temperature dielectric constant (ϵ_{rt}) decreases with increasing Ho content. The Curie temperature T_c and maximum dielectric constant (ϵ_m) at T_c remain almost unchanged. Remnant polarization (P_r), electromechanical coupling constant (k_p) and piezoelectric charge coefficient (d_{33}) exhibit increasing trend with increasing Ho content and reach their maximum values of 8.2 $\mu\text{C}/\text{cm}^2$, 25% and 220 pC/N respectively at 1.0 mol% of Ho content. The study reveals that doping of BCST system with appropriate quantity of Ho can improve its ferroelectric and piezoelectric properties.

1 Introduction

Lead-based piezoelectric ceramics, particularly PZT family, are widely used in sensors, actuators, ultrasonic motors, energy harvesting systems, speakers, transformers, and transducers due to their superior piezoelectric properties, high Curie temperature and relatively good temperature stability [1]. However, environmental concerns of the hazardous lead have necessitated the search for lead-free piezoelectric materials having the desired properties. Potential alternatives to lead-based ceramics include BaTiO₃ (BT), (K,Na)NbO₃ (KNN), (Bi,Na)TiO₃ (BNT), (Ba,Ca)(Ti,Zr)O₃ (BCTZ), (Ba,Ca)(Ti,Sn)O₃ (BCST), and (Ba,Ca)(Ti,Hf)O₃ (BCHT) [2–7]. Among these possibilities, BCTZ and BCST ceramics have attracted much attention in recent times after the reports of high piezoelectric properties observed in them [8–11]. The presence of morphotropic phase boundary (MPB) in PZT ceramics, which results in enhanced polarizability and ease in domain switching, is an important factor

for their extremely high dielectric, ferroelectric, and piezoelectric properties [12, 13]. Such a phase coexistence region can also be created in BCTZ and BCST systems which can lead to improvement of their piezoelectric properties [14]. It is reported that Ba(Zr_{0.2}Ti_{0.8})O_{3-x}(Ba_{0.7}Ca_{0.3})TiO₃ ceramics have excellent piezoelectric properties at the R–T boundary at $x=0.5$ [6]. Xue et al. reported that Ba(Sn_{0.12}Ti_{0.88})O_{3-x}(Ba_{0.7}Ca_{0.3})TiO₃ ceramics have great piezoelectric properties at the R–T boundary with $x=0.3$ [7]. The MPB of BCTZ is more vertical than that of BCST due to the difference in T_c among the end members BCT, BZT, and BTS (120 °C, 50 °C, and 30 °C, respectively). MPB would be a disadvantage at the Sn rich boundaries of BCST ceramics as it would reduce T_c and probably reduce the stability of the planar electro-mechanical coupling factor and piezoelectric properties with increasing temperature.

Addition of rare earth elements in dielectric ceramics such as BT stabilizes the temperature dependence of dielectric constant and lowers the dissipation factor [15, 16]. The incorporation of dopants in BT system is mainly determined by strain, charge, charge distribution and ionic size [17]. Assuming that local strain experienced by that ion is similar in both the sites, substitution is primarily dependent on ionic radius. In this case small rare earth ions will occupy the B-site as acceptors, large

✉ K. Chandramani Singh
kongbam@gmail.com

¹ Department of Physics, Sri Venkateswara College,
University of Delhi, New Delhi 110021, India

² Solid State Physics Laboratory, Lucknow Road, Timarpur,
Delhi 110054, India

one occupies A-site as donors and intermediate ions will occupy both sites with different partitioning for each ion [18, 19].

It is reported that BT doped with intermediate sized rare earth ions such as Dy, Ho and Y provide good electrical properties and higher reliability [15, 16]. Rare earth ion Ho^{3+} (radius ~ 0.1 nm) can substitute either Ba^{2+} (0.16 nm) or Ti^{4+} (0.06 nm) sites. When Ho^{3+} is substituted for Ba sites as a donor impurity, the extra charge is compensated by ionic charge compensation mechanism either by generation of cation vacancies (Ba^{2+} or Ti^{4+}) or by filling up the pre-existing oxygen vacancies and thereby making the material insulating; on the other hand when the charge compensation is electronic usually for low Ho concentration, it involves injection of charge in the crystal structure which provides a source of semiconductivity in the material. The solubility limit of Ho onto Ti sites of BT was found to be less than 3.0 mol% [20–22]. As holmium addition is less than 2 at.%, holmium substitutes both the two cation sites; however, holmium tends to substitute the Ba site under reducing conditions. The crystalline solubility limit of holmium is affected by Ba/Ti ratio. Compositions of $\text{Ba}/\text{Ti} < 1$ have low solubility limit of about 2 at.% and compositions of $\text{Ba}/\text{Ti} > 1$ have higher solubility limit of about 10 at.%. Under which conditions whether electronic or ionic charge compensation mechanism is preferred over other is still not clear. Preferred mechanism appears to be electronic at low dopant concentration and ionic at higher dopant concentration. There are different types of charge compensation mechanisms associated with $\text{BaO-TiO}_2\text{-HoO}_{3/2}$ ternary section composition [23], namely: (i) substitution of Ho onto Ti sites via creation of oxygen vacancies, (ii) double substitution of Ho onto both Ba and Ti sites, maintaining electroneutrality in the system, (iii) donor doping of Ho onto Ba with ionic compensation via creating either Ti vacancies or Ba vacancies or both. It has been observed that substitution of Ho at A site (Ba site) tends to increase the Curie temperature up to 2 mol% in $\text{Ba}_{1-x/2}\text{Ho}_x\text{Zr}_{0.025}\text{Ti}_{0.975}\text{O}_3$ ceramics synthesized by solid state reaction method and above 2 mol% the Curie temperature tends to decrease due to substitution of Ho ions at B site (Ti site) [24]. Reports also exist on the difficulty to optimize the concentration of acceptor or donor dopants in BT or BT based ceramics as the concentrations of electronic defects depends on sintering atmosphere as well as dopant amount [25, 26]. Despite all these studies, work on substitution of Ho in $(\text{Ba,Ca})(\text{Ti,Sn})\text{O}_3$ system has not so far been reported in literature.

In this paper, ceramics of $\text{Ba}_{0.91}\text{Ca}_{0.09}\text{Sn}_{0.07}\text{Ti}_{0.93}\text{O}_3 + x\text{Ho}_2\text{O}_3$ are prepared using solid state reaction method, the results on the structural, dielectric, ferroelectric and piezoelectric characterization of the prepared ceramics are reported.

2 Materials and methods

$(\text{Ba}_{0.91}\text{Ca}_{0.09}\text{Sn}_{0.07}\text{Ti}_{0.93})\text{O}_3 + x\text{Ho}_2\text{O}_3$ ($x = 0\text{--}1.0$ mol%) ceramics were prepared using conventional solid state reaction method. High purity raw materials: BaCO_3 (99.0%), CaCO_3 (99.5%), TiO_2 (99.5%), SnO_2 (99.0%) and Ho_2O_3 (99.9%) were weighed stoichiometrically. They were mixed for 20 h using ordinary ball mill with zirconia balls in an isopropanol medium at 80 rpm and then dried for 12 h at 70 °C. The dried samples were double calcined, first at 1050 °C for 4 h and then at 1075 °C for 4 h. The calcined powders were pressed into disks of 10 mm in diameter and 1.5 mm in thickness using 4 wt% polyvinyl alcohol (PVA) as a binder. The green pellets were sintered at 1450 °C for 4 h in air. These Ho-doped BCST ceramics will be respectively abbreviated as BCST0, BCST2, BCST4, BCST6, BCST8 and BCST10 in the increasing order of Ho contents. The sintered pellets were polished, silver-coated and fired at 130 °C for 30 min. For piezoelectric studies, the pellets were poled at 2–3 kV/mm electric field for 1 h at room temperature.

The crystal structures of the ceramics were examined by X-ray diffractometer (Bruker D8 Discover) with CuK_α radiation ($\lambda = 1.5416$ Å) over 2θ ranging from 20° to 80°. The bulk density was measured using the Archimedes' principle. The microstructures of the freshly fractured surfaces of the ceramics were viewed using SEM (Jeol JSM 6610L Japan). The dielectric properties and electromechanical coupling factors were measured using an Impedance analyzer (Wayne Kerr 6500B) with testing voltage of 1 V. The ferroelectric properties were examined using PE loop tracer system (Marine India). The piezoelectric charge coefficient (d_{33}) was measured with a Piezometer (Take Control, PM 25).

3 Results and discussion

3.1 Structural analysis

Figure 1 shows X-ray diffractograms of the BCST ceramic samples. The diffraction patterns reveal that all the ceramic samples form a single phase perovskite structure crystallizing into ferroelectric tetragonal phase with P4mm symmetry. This result indicates that all the dopants have completely diffused into the BCST lattice to form a homogeneous solid solution. The XRD patterns have been analyzed and refined using Powder X software with Treor program [27]. Also the X-ray diffraction peaks obtained matches well with JCPDS file no 03-0726.

The average crystallite size L and lattice strain η have been determined from a graph of $\beta \cos\theta$ versus $\sin\theta$, using the Williamson–Hall method [28, 29],

$$\beta \cos\theta = k\lambda/L + \eta \sin\theta$$

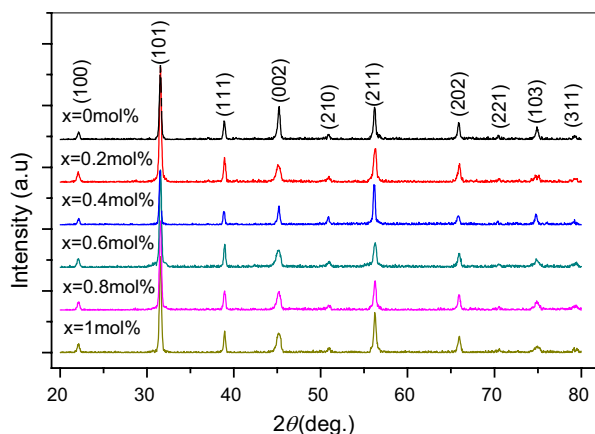
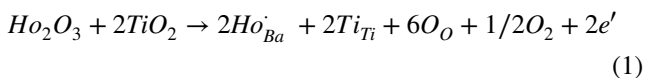


Fig. 1 X-ray diffraction patterns of Ho doped BCST ceramics

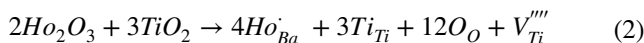
where β is the FWHM of the peak profile, θ the diffraction angle, and λ the wavelength of X-ray.

Table 1 shows the values of the refined lattice parameters with standard deviation in the range 0.0003–0.0007, crystallite size and strain of the ceramics with various Ho^{3+} contents. It is seen that both the crystallite size and strain initially decreases for Ho^{3+} contents up to 0.4 mol%, and then increases at higher Ho^{3+} concentrations. Tetragonality (c/a ratio) does not change significantly over the range of Ho^{3+} content investigated, except for the value of 0.9994, lower than 1, observed for BCST4. The XRD patterns in Fig. 1 also show that there is a gradual shifting of the diffraction peaks towards the lower angles, indicating an increase in lattice unit cell volume of the ceramics with increasing Ho^{3+} content up to 0.4 mol%. Partial substitution of Ho^{3+} with ionic radius ($\text{IR} = 0.9 \text{ \AA}$) for Ba^{2+} ($\text{IR} = 1.6 \text{ \AA}$) with electronic charge compensation mechanism is expected to be primarily responsible for the altered unit cell dimensions. When Ho^{3+} ion incorporate Ba^{2+} site in BT system, the extra charge is compensated electronically with the reduction of Ti^{4+} to Ti^{3+} [30, 31]. This can be well explained using Kröger and Vink defect notion given by [32]:



This observed expansion of unit cell volume is a result of appearance of Ti^{3+} ions ($\text{IR} = 0.67 \text{ \AA}$) having larger Ionic radii than Ti^{4+} ions ($\text{IR} = 0.6 \text{ \AA}$), which is a consequence of this plausible electronic mechanism preferred for Ho substitution in Barium sub lattice up to low 0.4 mol% concentration.

However, as Ho^{3+} content further increases beyond 0.4 mol%, there is an observed shifting of the diffraction peaks towards the higher angles, indicating a decrease in unit cell volume. This shifting is attributed to the replacement of Ba^{2+} ions by Ho^{3+} ions in the higher Ho concentration region via ionic charge compensation mechanism. When Ho^{3+} ion substitute Ba^{2+} site, ionic charge compensation mode is preferred at higher dopant concentration under oxidizing condition; i.e. by generation of Ti vacancies [33]. The associated defect chemistry equation can be written as follows.



The evidence of switching over of the charge compensation mechanism from electrons (e') to cation vacancies ($V_{\text{Ti}}^{\prime\prime\prime}$) around 0.4 mol% Ho content is also vividly supported by the trend of observed values of cell volume listed in Table 1. Such a combination of two doping mechanisms has also been observed in Ho-doped BT system, wherein substitution of Ho^{3+} ions onto Ba^{2+} sites through electronic compensation is the preferred mechanism at low doping level less than 0.5 mol%, but the possibility of another mechanism involving substitution of Ho^{3+} onto Ba^{2+} sites via cation vacancies at higher concentration has been highlighted [34].

The phase transition in a ferroelectric system is always accompanied by a complex evolution of domain structure which tries to minimize the electric and elastic energy of the system. The growth and orientation of domain walls during the transformation gives rise to a change in crystal symmetry. For instance, while transiting from the cubic to tetragonal phase via the transition temperature T_c , strain is induced in the system and depolarization field is created. In order to minimize the strain and thus depolarization field, the system undergoes formation of domains, surface charge or polarization gradients within the crystal. The mechanism

Table 1 Crystallographic and microstructural properties of Ho-doped $\text{Ba}_{0.91}\text{Ca}_{0.09}\text{Sn}_{0.07}\text{Ti}_{0.93}\text{O}_3$ ceramics

Ho content x (mol%)	Crystallite size (\AA)	Strain	Lattice parameters (\AA)			Cell volume (\AA^3)	Grain size (μm)
			a	c	c/a		
0.0	314	0.0037	4.0051	4.0069	1.0004	64.274	20.21
0.2	325	0.0031	4.0007	4.0170	1.0041	64.294	18.24
0.4	188	0.0012	4.0422	4.0397	0.9994	64.923	20.29
0.6	275	0.0024	3.9981	4.0184	1.0051	64.234	20.51
0.8	333	0.0032	4.0016	4.0088	1.0018	64.194	21.57
1.0	440	0.0056	4.0059	4.0155	1.0024	64.185	29.18

of domain formations and their organization however is strongly dependent on the crystallite size of the system. Hsiang et al. [35], considering the thermodynamic relations for unconstrained small crystallites ($< 300 \text{ \AA}$) which do not experience any clamping force from neighboring crystallites as well as for constrained bigger crystallites ($> 300 \text{ \AA}$) which are clamped by its neighboring crystallites during the transition from cubic to tetragonal phase in BT, reported that for small crystallites less strain is produced during transformation and therefore such crystal systems exist mostly in stable cubic phase below T_c . As the crystallites grow in size, more strain is produced due to hard agglomeration and more BT transform to tetragonal phase as a way to relieve the strain by formation of ferroelectric domains. Whether the system will be single domain (t-BT) or multidomain (t-BT) is dependent on clamping conditions. In view of these considerations, BCST4 having minimum crystallite size ($\sim 188 \text{ \AA}$), least strain (0.0012) and small tetragonality (c/a) is more likely to be in a cubic paraelectric phase below the Curie temperature T_c as compared with others. Also It is also reported by many researchers that the system possessing high strain values has high tetragonality observed [36, 37]. BCST4, having low strain value (~ 0.0012) results in low tetragonality (~ 0.9994) due to the release of internal stress as a consequence of enlarged unit cell volume.

3.2 Density and surface morphology

Figure 2 shows the effect of Ho^{3+} content on the theoretical density (TD) and relative density of the BCST ceramics. As Ho^{3+} concentration increases, the bulk density gradually decreases from 5.394 g/cm^3 (91.02% of their TD) for the ceramic composition with no Ho^{3+} to the minimum value of 4.865 g/cm^3 (82.77% of their TD) for 0.4 mol% Ho^{3+}

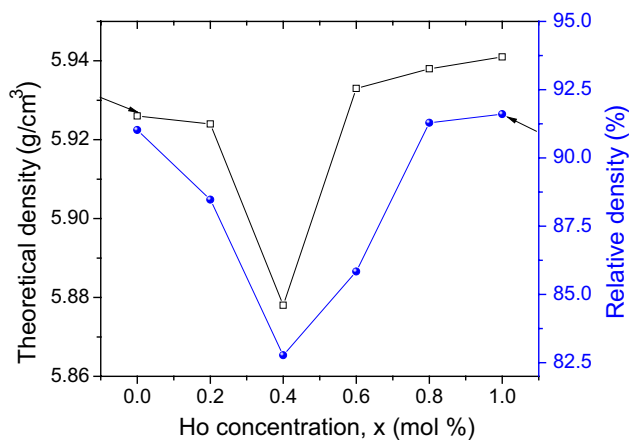


Fig. 2 Plot of theoretical density and relative density of BCST ceramics against Ho^{3+} content

and then increases to 5.442 g/cm^2 (91.60% of their TD) for 1.0 mol% Ho^{3+} .

Figure 3 shows the SEM micrographs of pure and Ho-doped BCST ceramics. Slope intercept method using Image J software is used to measure the grain size for each composition. The grain size tends to decrease slightly from $20.2 \mu\text{m}$ for undoped ceramic composition to the value of $18.2 \mu\text{m}$ for 0.2 mol% Ho^{3+} and then increases gradually to $29.2 \mu\text{m}$ for 1.0 mol% Ho^{3+} (Table 1). The Porous and non-uniform microstructure distribution is prevalent at low dopant concentration ($x \leq 0.4 \text{ mol\%}$) giving rise to low density in these samples. The porous microstructure in these samples may be due to the creation of oxygen vacancies during the synthesis at higher temperature [38]. The microstructures of BCST6, BCST8 and BCST10 exhibit the presence of a liquid phase sintering. The augmentation of liquid phase sintering and enhancement of grain size have contributed to the improved density of the ceramic system with increasing Ho content in the range of 0.4–1.0 mol%. This liquid phase contributes to sintering by accelerating particle redistribution due to enhanced atomic mobility [39]. The study thus reveals that addition of Ho significantly affects the microstructure of BCST ceramics.

3.3 Dielectric studies

Figure 4a shows the temperature dependence of the dielectric constant of the BCST ceramic samples measured at 100 kHz from room temperature up to $120 \text{ }^\circ\text{C}$. The ϵ'' curves of the ceramic samples exhibit one peak corresponding to the ferroelectric to paraelectric phase transition ($T_c \sim 44$ – $66 \text{ }^\circ\text{C}$). As seen in Fig. 4a, T_c exhibits no significant change with increase in Ho content, except for the significantly lower value of $T_c \sim 44 \text{ }^\circ\text{C}$ observed at 0.4 mol%. The dielectric loss tangent ($\tan\delta$) value tends to increase from 0.023 for no Ho content to 0.028 for 0.4 mol% Ho content, with a gradual decrease in value beyond 0.4 mol%. This result is in agreement with density change observed with variation in Ho content. However, room temperature dielectric constant (ϵ_r) value recedes with rise in Ho content except for the sample with 0.4 mol% Ho concentration. Figure 4b depicts the variations of room temperature dielectric constant with frequency.

Sudden rise in dielectric constant value observed for BCST4 is attributed to the shift in its curie temperature near room temperature. It is a general understanding that the system undergoes a change in its anisotropy near Curie temperature. This favors enhancement in polarization rotation and thus improves shear susceptibility and dielectric constant value [9]. Receding dielectric constant value beyond 0.4 mol% Ho content is a consequence of increase in the average grain size which plays a dominant role in controlling dielectric behavior of the material. As grain size

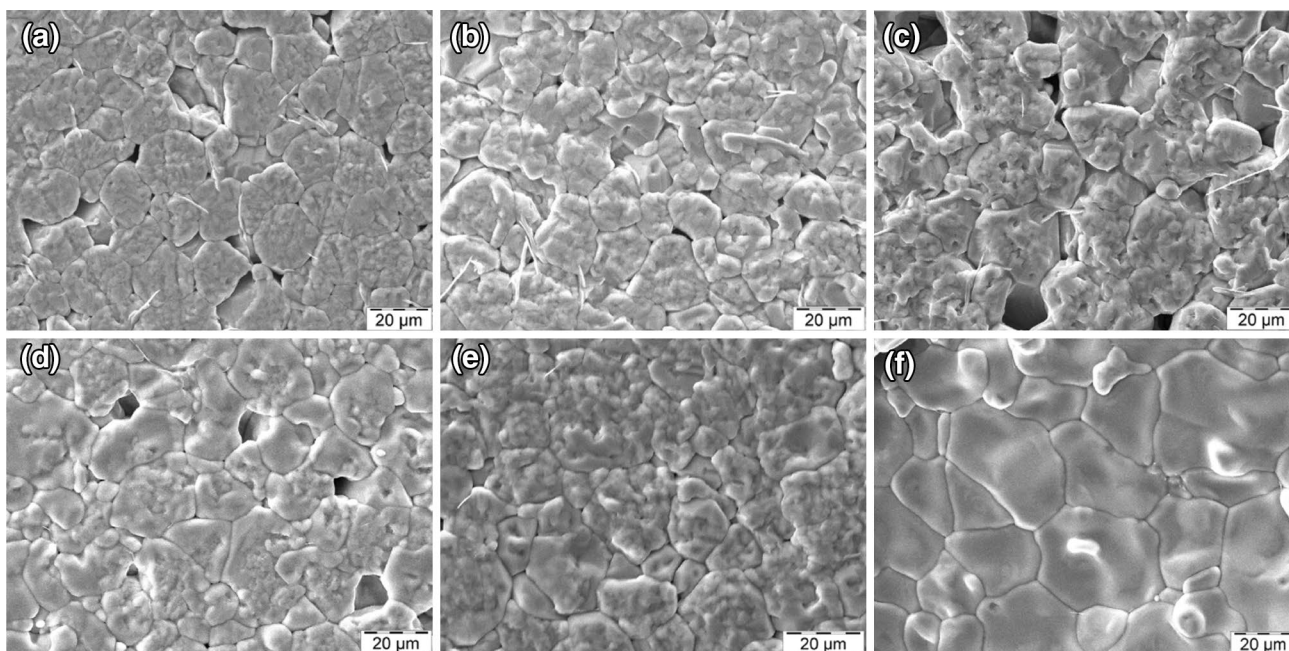
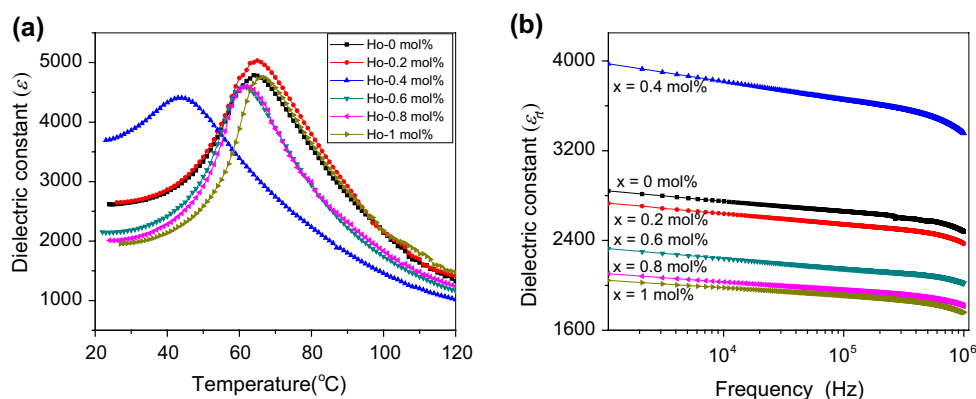


Fig. 3 SEM micrographs of Ho-substituted BCST ceramics **a** $x=0$ mol% **b** $x=0.2$ mol% **c** $x=0.4$ mol% **d** $x=0.6$ mol% **e** $x=0.8$ mol% and **f** $x=1.0$ mol%

Fig. 4 **a** Temperature dependence of dielectric constant (ϵ), measured at 100 kHz, **b** Variation room temperature dielectric constant (ϵ_r) as a function of frequency, for BCST



increases, grain boundary regions; high insulating regions having higher capacitance associated with them decreases in percentage than low resistive regions i.e. grain bulk regions [40].

Figure 4a also shows broadening of the dielectric peaks around T_c indicating diffuse phase transitions. To further study the phenomenon, the dielectric constants at temperatures higher than T_c have been fitted to the modified Curie–Weiss law, proposed by Uchino and Nomura [41]:

$$1/\epsilon - 1/\epsilon_m = (T - T_m)^\gamma / C, (T > T_m) \quad (3)$$

where diffusivity γ and C are the constants, with $1 < \gamma < 2$. The value of γ determines the degree of diffuseness of the phase transition. The value of γ is equal to 1 for a system with a completely ordered transition. On the basis of a local

compositional fluctuation model, the value of γ is equal to 2 for a completely diffused system.

Figure 5 shows the plots of $\ln(1/\epsilon - 1/\epsilon_m)$ versus $\ln(T - T_m)$ for the ceramics. The values of γ as determined from the slopes of the graphs in Fig. 5 exhibit a systematic change with increasing Ho contents in the ceramics. It can be noted that γ increases from 1.54 to 1.62 at 0.4 mol%, and then decreases to 1.47 for 1 mol% indicating that the diffuseness of the ferroelectric transition peaks at Ho content of 0.4 mol%.

3.4 Ferroelectric studies

Figure 6a shows the room temperature polarization–electric field (P – E) hysteresis loops of Ho-doped BCST ceramics,

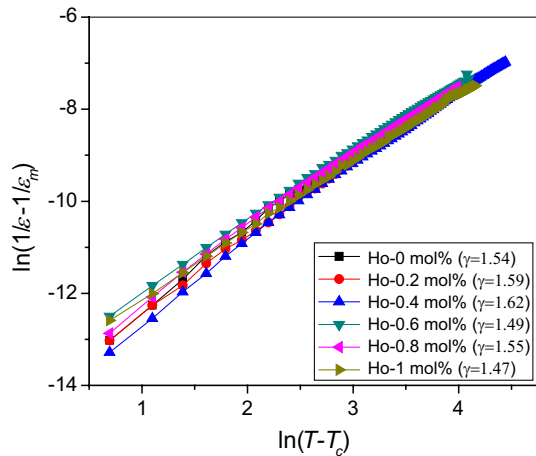


Fig. 5 Variation of $\ln(1/\epsilon-1/\epsilon_m)$ with $\ln(T-T_c)$ for BCST ceramics having different Ho^{3+} contents

measured at 50 Hz frequency. From the P - E hysteresis loops in Fig. 6a, P_r and E_c were determined for the ceramics and are shown in Fig. 6b. For the base composition BCST0, the remnant polarization P_r is $5.8 \mu\text{C}/\text{cm}^2$ and the coercive field E_c is $2.3 \text{ kV}/\text{cm}$. With increasing Ho^{3+} content, P_r decreases to a minimum value of $\sim 2.5 \mu\text{C}/\text{cm}^2$ at 0.4 mol% Ho^{3+} content and then increases to $8.2 \mu\text{C}/\text{cm}^2$ at 1.0 mol% Ho^{3+} content. This variation in the P_r value indicates that Ho^{3+} substitution in the range 0–0.4 mol% weakens ferroelectricity of BCST, whereas the substitution in the range 0.4–1.0 mol% strengthens its ferroelectricity, which can be used for memory device applications like non-volatile data storage below their T_c .

The observed variation of P_r with Ho content is in accordance with that of the crystallite size (Table 1), for the change of crystallite size on account of Ho^{3+} substitution would result in a similar change in domain size and in turn P_r . Existence of such a “size-effect” has also been reported by

Arlt et al. [42] who demonstrated in BaTiO_3 that the equilibrium domain width depends on the grain size and decreases for grain sizes $< 10 \mu\text{m}$, and is effectively constant for grain size $> 10 \mu\text{m}$. In the present work, significant decrease in P_r is observed for BCST4 where the crystallite size shows a minimum.

The squareness of the loop R_{sq} has been calculated using the formula:

$$R_{sq} = P_r/P_s + P_{1.1E_c}/P_r$$

where P_s is the spontaneous polarization and $P_{1.1E_c}$ is the polarization value at 1.1 times of coercive field value. For fully saturated hysteresis loops R_{sq} is equal to 2.

Figure 6c shows the plots of spontaneous polarization P_s and squareness of the loop R_{sq} versus Ho content. It is seen that both the parameters exhibit a declining trend with the increasing Ho content of up to 0.4 mol%, after which their values show a rise. The variation of P_s with Ho content is in agreement with similar variation in lattice strain (Table 1). This observation supports the Landau Ginzburg theory which predicts that square of the spontaneous polarization is directly proportional to lattice strain. The behavior of the graphs of P_s and R_{sq} in Fig. 6c indicates that ferroelectric nature of the BCST ceramics is more enhanced as the composition is farther away from 0.4 mol% Ho content.

It is well known that crystallite (or grain) size has strong influence on the ferroelectric domain structure, domain nucleation and domain mobility, and hence plays an important role in determining the ferroelectric properties of a material. The ferroelectric behavior in small crystallites is highly masked by the strong contribution from crystallite boundary effects that hinder polarization switching. With increasing crystallite size, the energy barrier for ferroelectric domain switching decreases. As a consequence, the reversal of polarization direction of a ferroelectric domain occurs with much ease in a large crystallite compared with that in a small crystallite [43]. In view of this, the observed trend of

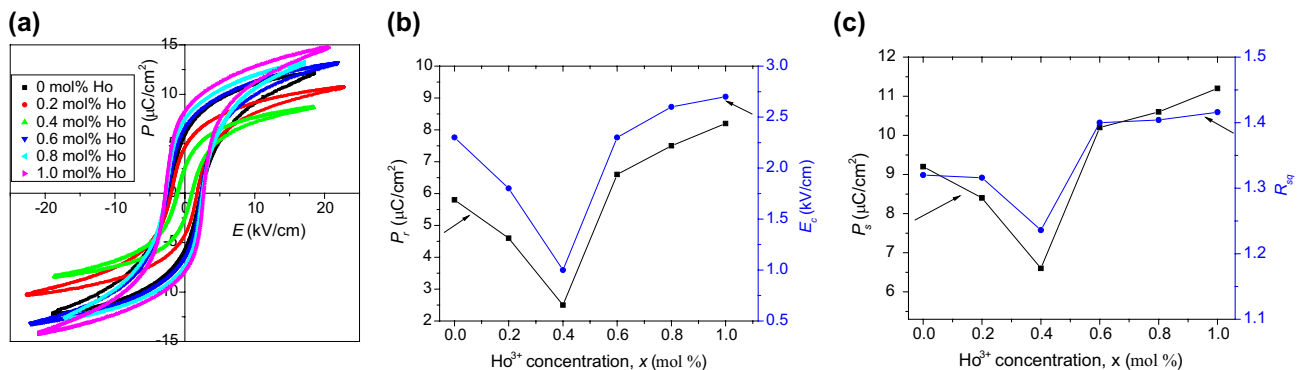


Fig. 6 **a** Room temperature P - E hysteresis curves measured at 50 Hz, **b** plots of P_r and E_c versus x , and **c** plots of P_s and R_{sq} versus x , for BCST ceramics

P_r with a dip in its value to $2.52 \mu\text{C}/\text{cm}^2$ at 0.4 mol% Ho content is commensurate with the corresponding crystallite size change observed with increasing Ho contents (Fig. 3). Such a variation of P_r as a function of crystallite size has been reported by Liu et al. [44] in PZT. More generally, the existence of “size effect” in ferroelectrics has also been observed in different ceramic systems [44–47]. Another influential parameter leading to the rise in P_r values above 0.4 mol% Ho content is the effect of cation vacancy defects in the crystal structure. As examined using xrd analysis, the Barium site (A-site) is being substituted by Ho via generation of cation vacancies ($V_{Ti}^{\prime\prime}$) for higher Ho content ($> 0.4 \text{ mol}\%$). These vacancies tend to behave as nucleating sites for new domains during polarization switching thereby increasing polarization values [48].

The observed low values of spontaneous polarization (P_s) and T_c for BCST4 can be also ascribed to the associated relatively small value of its tetragonality (Table 1). For the ferroelectric materials having perovskite structure, the tetragonality (c/a) is well known to produce significant influence on their ferroelectric properties such as P_s and T_c [49]. The general understanding is that increasing tetragonality in the material yields higher values of P_s and T_c .

It can be noted that, the electronic substitution of Ba^{2+} ion in BCST system with 0.4 mol% Ho^{3+} ion (Fig. 4) results in a significant shifting of the ferroelectric–paraelectric transition (T_c) to lower temperature. As a result of this shifting of T_c , the paraelectric cubic phase of BCST4 comes so close to the room temperature that its ferroelectric property degrades appreciably and P_r falls from $5.8 \mu\text{C}/\text{cm}^2$ for $x=0$ to $2.5 \mu\text{C}/\text{cm}^2$ for $x=0.4 \text{ mol}\%$.

3.5 Piezoelectric studies

Figure 7 shows variations of piezoelectric coefficient d_{33} and electromechanical coupling coefficient k_p with Ho content x . Both these parameters follow a decreasing trend for the initial Ho contents up to 0.4 mol%, but pick up higher values with further increase of Ho concentration. As seen in Fig. 7, the piezoelectric properties are the least for BCST4 ($d_{33}=60 \text{ pC}/\text{N}$, $k_p=8\%$) and the highest for BCST10 ($d_{33}=220 \text{ pC}/\text{N}$, $k_p=25\%$).

The variation of d_{33} observed agrees with the similar change in the density of the ceramics with Ho doping. From thermodynamic theory, the piezoelectric constant d_{33} of a ferroelectric material can be expressed [50] as :

$$d_{33} = 2Q_{11}\epsilon_0\epsilon_{rt}P_s$$

where ϵ_{rt} is the room temperature dielectric constant, Q_{11} the electrostrictive coefficient and P_s the spontaneous polarization. The parameter Q_{11} depends on the domain structure and normally does not change appreciably by doping. The parameter ϵ_{rt} in the present study will also have less

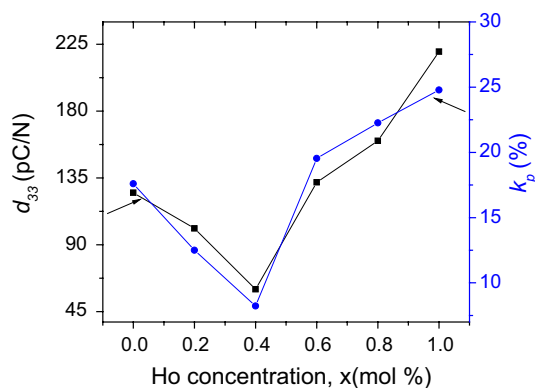


Fig. 7 Variations of d_{33} and k_p as a function of Ho-content in BCST

influence on d_{33} in view of the diffuse phase transition occurring near the room temperature. Therefore the observed decrease (or increase) in d_{33} with increasing x (Fig. 7) system could be mainly attributed to the associated change in P_s (Fig. 6c).

The observed trend of piezoelectric properties can also attributed to the different crystallite sizes (Table 1) of the ceramics. In general, larger crystallite size helps in the lattice distortion from the cubic symmetry, thereby resulting in the improvement of piezoelectricity. In addition to this, as the crystallite size increases, mechanisms like pinning of domain walls would lessen, and the domain motion would be with less hindrance [51]. The increase in domain mobility would increase the polarization switching rate and in turn the piezoelectric properties of the ceramics. There are reports of improvement of piezoelectric properties in other perovskite systems having suitably large crystallites [52, 53].

It can further be noted that the observed trend of d_{33} is also in consistent with the observed variation of strain (Table 1) existing in the ceramics. For instance, the large strain of 0.0056 in BCST10 could cause an anisotropic distortion of the TiO_6 octahedral of the perovskite system which facilitates a preferential Ti off-center movement. Such a distortion would help in strengthening the spontaneous polarization and hence piezoelectric properties of the ceramic system.

4 Conclusion

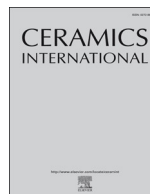
In this paper the influence of Ho content on micro-structural, electrical and piezoelectric properties of $\text{Ba}_{0.91}\text{Ca}_{0.09}\text{Sn}_{0.07}\text{Ti}_{0.93}\text{O}_3$ ceramics has been studied. With increasing Ho contents, Ho-substitution at Ba^{2+} site mechanism switches from electronic to ionic at about 0.4 mol% Ho. This results in systematic changes of unit cell volume, crystallite and lattice strains of the ceramics. Ferroelectric, dielectric and piezoelectric properties of the ceramics reflect

strong influence of the Ho substitution. While increasing dominance of electronic compensation mechanism at low Ho content causes a decline in the values of remnant polarization (P_r), electromechanical coupling constant (k_p) and piezoelectric charge coefficient (d_{33}), switching over to ionic compensation mechanism enhances their values at higher Ho content. The optimum values of 220 pC/N, 25% and 8.2 $\mu\text{C}/\text{cm}^2$ were obtained for d_{33} , k_p and P_r respectively at 1.0 mol% of Ho content. The study reveals that controlled substitution of Ba-site of BCST system with suitable amount of Ho can improve its ferroelectric and piezoelectric properties making them useful as piezoelectric transducers actuators and ultrasonic motors.

Acknowledgements This work is financially supported by the Department of Science and Technology, India, under the Research Project No. EMR/2014/284. We also acknowledge the directors of solid state physics laboratory, Delhi for providing facilities for some measurements.

References

- B. Jaffe, W.R. Cook, H. Jaffe, *Piezoelectric Ceramics*, (Academic Press, London, 1971)
- H. Du, Z. Li, F. Tang, S. Qu, Z. Pei, W. Zhou, *Mater. Sci. Eng. B* **131**, 83 (2006)
- R. Gaur, A. Dhingra, S. Pal, K.C. Singh, *J. Alloys Compd.* **625**, 284 (2015)
- P. Kantha, K. Pengpat, P. Jarupoom, U. Intatha, G. Rujijanagul, T. Tunkasiri, *Curr. Appl. Phys.* **9**, 460 (2009)
- Y. Zhang, J. Li, B. Zhang, C. Peng, *J. Appl. Phys.* **103**, 074109 (2008)
- C. Zhou, X. Liu, *Mater. Chem. Phys.* **108**, 413 (2008)
- K.C. Chitra, Singh, *J. Alloys Compd.* **765**, 869 (2018)
- W. Liu, X. Ren, *Phys. Rev. Lett.* **103**, 257602 (2009)
- D. Xue, Y. Zhou, H. Bao, J. Gao, C. Zhou, X. Ren, *Appl. Phys. Lett.* **99**, 122901 (2011)
- X. Liu, M. Zhu, Z. Chen, B. Fang, J. Ding, X. Zhao, H. Xu, H. Luo, *J. Alloys Compd.* **613**, 219 (2014)
- Z. Zhao, X. Li, H. Ji, Y. Dai, T. Li, *J. Alloys Compd.* **637**, 291 (2015)
- R. Guo, L.E. Cross, S.E. Park, B. Noheda, D.E. Cox, G. Shirane, *Phys. Rev. Lett.* **84**, 5423 (2000)
- Y. Ishibashi, M. Iwata, *Jpn. J. Appl. Phys.* **37**, L985 (1998)
- M. Chen, Z. Xu, R. Chu, H. Qiu, M. Li, Y. Liu, L. Shao, S. Ma, W. Ji, W. Li, S. Gong, G. Li, *Phys. B* **433**, 43 (2014)
- Y. Sakabe, Y. Hamaji, H. Sano, N. Wada, *Jpn. J. Appl. Phys.* **41**, 5668 (2002)
- H. Saito, H. Chazono, H. Kishi, N. Yamaoka, *Jpn. J. Appl. Phys.* **30**, 2307 (2001)
- Y. Tsur, T.D. Dunbar, C.A. Randall, *J. Electroceram.* **7**, 25 (2001)
- G.V. Lewis, C.R.A. Catlow, *J. Radiat. Eff.* **73**, 307 (1983)
- G.V. Lewis, C.R.A. Catlow, *J. Phys. Chem. Sol.* **47**, 89 (1986)
- J. Itoh, H. Haneda, S. Hishita, I. Sakaguchi, N. Ohashi, D.C. Park, I. Yashima, *J. Mater. Res.* **19**, 3512 (2004)
- J. Itoh, D.C. Park, N. Ohashi, I. Sakaguchi, I. Yashima, H. Haneda, J. Tanaka, *J. Ceram. Soc. Jpn.* **110**, 495 (2002)
- D. Makovec, Z. Samardmija, M. Drogenik, *J. Am. Ceram. Soc.* **89**, 3281 (2006)
- Y. Liu, A.R. West, *J. Eur. Ceram. Soc.* **29**, 3249 (2009)
- P.A. Jha, A.K. Jha, *Ceram. Inter.* **40**, 5209 (2014)
- K. Sasaki, J. Maier, *J. Appl. Phys.* **86**, 5422 (1999)
- S.H. Yoon, H. Kim, *J. Appl. Phys.* **92**, 1039 (2002)
- C. Dong, *J. Appl. Crystallogr.* **32**, 838 (1999)
- B.D. Cullity, *Elements of X-ray diffraction* (Addison and Wesley Publishing Company Inc., Boston, 1978), p. 356
- G.K. Williamson, W.H. Hall, *Acta Metall.* **1**, 22 (1953)
- C.V. Lewis, C.R. Catlow, *J. Phys. Chem. Solids* **47**, 89 (1986)
- M.T. Buscaglia, V. Buscaglia, M. Viviani, P. Nanni, *J. Am. Ceram. Soc.* **84**, 376 (2001)
- F.A. Kröger, H.J. Vink, *Solid State Physics* (Academic Press, New York, 1956)
- H.M. Chan, M.P. Harmer, D.M. Smyth, *J. Am. Ceram. Soc.* **69**, 507 (1986)
- J. Jeong, E.J. Lee, Y.H. Han, *Jpn. J. Appl. Phys.* **44**, 4047 (2005)
- H.-I. Hsiang, F.-S. Yang, *J. Am. Ceram. Soc.* **79**(4), 1053 (1996)
- C. Wu, W. Duan, X.W. Zhang, Z. Liu, *J. Appl. Phys.* **108**, 124102 (2010)
- J.F. Li, Z.X. Zhu, F.P. Lai, *J. Phys. Chem. C* **114**, 17796 (2010)
- V.S. Puli, P. Li, S. Adireddy, D.B. Chrisey, *J. Adv. Dielectr.* **5**, 1550027 (2015)
- Y. Zhen, J.F. Li, *J. Am. Ceram. Soc.* **90**, 3496 (2007)
- S. Wang, T.A. Tan, M.O. Lai, L. Lu, *Mater Res Bull* **45**, 279 (2010)
- K. Uchino, S. Nomura, *Integr. Ferroelectr.* **44**, 55 (1982)
- G. Arlt, D. Hennings, G. de With, *J. Appl. Phys.* **58**, 1619 (1985)
- C. Leu, C.Y. Chen, C.H. Chien, *Appl. Phys. Lett.* **82**, 3493 (2003)
- J.S. Liu, S.R. Zhang, H.Z. Zeng, C.T. Yang, Y. Yuan, *Phys. Rev. B* **72**, 172101 (2005)
- K. Ishikawa, K. Yoshikawa, N. Okada, *Phys. Rev. B* **37**, 5852 (1988)
- M.H. Frey, D.A. Payne, *Phys. Rev. B* **54**, 3158 (1996)
- S. Huo, S. Yuan, Z. Tian, C. Wang, Y. Qiu, *J. Am. Ceram. Soc.* **95**, 1383 (2012)
- Y. Noguchi, H. Shimizu, M. Miyayama, *J. Ceram. Soc. Jpn.* **110**, 999 (2002)
- S.C. Abrahams, S.K. Kurtz, P.B. Jamieson, *Phys. Rev.* **172**, 551 (1968)
- B.M. Jin, J. Kim, S.C. Kim, *Appl. Phys. A* **65**, 53 (1997)
- K.C. Singh, C. Jiten, R. Laishram, O.P. Thakur, D.K. Bhattacharya, *J. Alloys Compd.* **496**, 717 (2010)
- H. Takahashi, Y. Numamoto, J. Tani, K. Matsuta, J. Qiu, S. Tsurekawa, *Jpn. J. Appl. Phys.* **45**, L30 (2006)
- C.A. Randall, N. Kim, J.P. Kucera, W. Cao, T.R. Shrout, *J. Am. Ceram. Soc.* **81**, 677 (1998)



Impact of crystal structure and microstructure on electrical properties of Ho doped lead-free BCST piezoceramics



Chitra^a, Ankit Khandelwal^a, Rahil Gupta^a, Radhapiyari Laishram^b, K. Chandramani Singh^{a,*}

^a Department of Physics, Sri Venkateswara College, University of Delhi, New Delhi, 110021, India

^b Solid State Physics Laboratory, Lucknow Road, Timarpur, Delhi, 110054, India

ARTICLE INFO

Keywords:

Sintering
Grain size
Electrical properties
BaTiO₃ and titanates

ABSTRACT

Conventional solid state sintering method was used to synthesize lead-free (Ba_{0.91}Ca_{0.09}Sn_{0.07}Ti_{0.93})O₃-xHo₂O₃ (x = 0, 1.2, 1.4, 1.6, 1.8 and 2.0 mol%) ceramics. The influence on electrical properties of the system as a result of the structural and microstructural changes introduced by the incorporation of rare earth Ho³⁺ ions has been investigated. The X-ray diffraction analysis reveals that Ho³⁺ ions completely diffuse into the (Ba_{0.91}Ca_{0.09}Sn_{0.07}Ti_{0.93})O₃ lattice to form a homogeneous solid solution with a pure perovskite structure having tetragonal symmetry. Evidence of Ho³⁺ substituting Ti⁴⁺ via the oxygen vacancy compensation mechanism exists in the range of 0–1.6 mol % Ho content, while the self-compensation mode is the preferred mechanism beyond 1.6 mol %. The average grain size exhibits a drastic reduction from 16 μm to 0.7 μm as the Ho content increases from 0 to 1.6 mol%, followed by a slight increase at higher Ho concentration. It suggests that addition of Ho³⁺ inhibits grain growth in the ceramics. In the composition range studied, increasing Ho³⁺ content produces a gradual decrease in the relative density from 93% to 81%, room temperature dielectric constant (ϵ_r) from 3997 to 807, electromechanical coupling factor (k_p) from 0.23 to 0.06, and piezoelectric charge constant (d_{33}) from 102 to 38 pC/N. This degradation in the properties is attributed to the crystalline and microstructural changes driven by the increasing presence of Ho content in the ceramics.

1. Introduction

The piezoelectricity business reached a total of 36 billion USD in 2017 with the actuator applications occupying 38.89% of the total piezoelectric market [1,2]. Lead zirconate titanate (PZT) dominates the electronic industry as one of the most efficient and reliable piezoelectric materials since 1960s. In PZT, the so-called morphotropic phase boundary (MPB) is present which results in enhanced polarizability and ease in domain switching providing properties largely independent of temperature [3,4]. However, this lead-free material has been banned due to environmental concerns following *RoHs (Restriction of Hazardous Substances Directive)* [5]. A lot of research has been dedicated to developing new lead-free perovskites to reduce the production and waste disposal of toxic lead [6–8]. The endeavor to develop lead-free perovskites has mostly been focused on creating an MPB in these materials. Research in this direction has yielded new lead-free alternatives based on BaTiO₃(BT), (K,Na)NbO₃ (KNN), (Bi,Na)TiO₃(BNT), (Ba,Ca)(Ti,Zr)O₃ (BCTZ), (Ba,Ca)(Ti,Sn)O₃(BCST), and (Ba,Ca)(Ti,Hf)O₃ (BCTH), having high piezoelectric properties [9–15].

Among these materials, barium titanate (BaTiO₃, BT) is the first

lead-free piezoelectric ceramic to be fabricated via conventional solid-state reaction method [16]. However, the piezoelectric properties of pure BT ceramic are practically low with its d_{33} of about 190 pC/N. However, some breakthroughs have recently been made in BT based system with the addition of dopants like Zr, Sn or Ca which play an important role in altering its phase transition behavior [17–21]. In one such modified BT system, (Ba,Ca)(Ti,Sn)O₃, it has been reported that different phase boundaries can be constructed by modifying the proportion of Ca and Sn, leading to enhanced electrical and piezoelectric properties in the ceramics [22–24]. Aliovalent cations are reported to be effective dopants for improving electrical properties in BaTiO₃ systems due to their acceptor/donor behavior [25]. The atomic radii of trivalent rare earth cations lie between Ba²⁺ and Ti⁴⁺ ions. This gives them the ability to substitute both dodecahedrally coordinated A- and octahedrally coordinated B- site, and therefore are widely used to modify BaTiO₃ [26,27]. These trivalent rare earth cations such as Ho³⁺, Y³⁺ and Dy³⁺ are known to stabilize the temperature dependence of relative dielectric constant by lowering the dissipation factor in dielectric ceramics [28]. Ho³⁺, Y³⁺ and Dy³⁺ show the most amphoteric behavior in BaTiO₃ [26–29]. When these ions are substituted for the A-

* Corresponding author.

E-mail address: kongbam@gmail.com (K.C. Singh).

<https://doi.org/10.1016/j.ceramint.2019.02.095>

Received 27 December 2018; Received in revised form 31 January 2019; Accepted 14 February 2019

Available online 15 February 2019

0272-8842/ © 2019 Elsevier Ltd and Techna Group S.r.l. All rights reserved.

site, they act as donors and reduce the concentration of oxygen vacancies [30], but when these dopants occupy the B-site, they act as acceptors and lower the bulk diffusion of oxygen vacancies through strain and electric field interactions [31]. It is also reported that rare earth elements are dominant additives in BT forming the shell structure [32]. Also a well-developed core-shell is observed when the rare-earth elements are added to BaTiO₃ [32]. Abnormal grain growth can be restrained on doping with rare earth elements thus improving the dielectric properties [33]. Trivalent rare earth cations, owing to their special electronic structure and moderate ionic radii, have been widely used in fruitfully modifying barium titanate based ceramics by incorporating them in both A- and B-sites of ABO₃ lattice [33,34].

The incorporation mechanism of these dopants depends on the initial composition, the ionic radii difference, the A/B ratio and the thermodynamic conditions of the system [26,27]. There are detailed reports on the solid solubility of Ho in BaTiO₃ at high temperatures in air as well as in reducing conditions [35,36]. Under oxidizing condition, in TiO₂ rich samples, a relatively low concentration (1.4 mol%) of Ho preferentially occupies Ba-lattice sites via formation of ionized Ti vacancies to compensate for the excess donor charge. Beyond this concentration, it substitutes Ti-sites in BT system by creating ionized oxygen vacancies for charge compensation [35]. However, this solubility of Ho at Ba site increases to about 4 mol% under reducing conditions [36].

In our previous paper, we reported the effects of free doping of Ho in BT modified BCST system in low concentration range ($x \leq 1$ mol%) [37]. It showed significant improvement in ferroelectric and piezoelectric properties when incorporated in Ba-site (A-site) of the system. The present work reports the result of the influence of Ho on the structural and electrical behavior of BCST system at higher Ho concentrations.

2. Materials and methods

Lead-free (Ba_{0.91}Ca_{0.09}Sn_{0.07}Ti_{0.93})O₃-xHo₂O₃ ($x = 0, 1.2, 1.4, 1.6, 1.8$ and 2.0 mol %) ceramic compositions were synthesized using conventional solid state reaction method. The AR grade raw materials: BaCO₃, CaCO₃, TiO₂, SnO₂ and Ho₂O₃ (Aldrich, purity $\geq 99\%$) were weighed according to their stoichiometry for each composition. After careful weighing, they were mixed for 20 h using ordinary ball mill in plastic bottle containing isopropyl alcohol as milling media with zirconia balls. The mixture was then dried for 12 h at 70 °C in oven and thereafter double calcined, first at 1050 °C for 4 h and then at 1075 °C for 4 h in air. The powder samples were also hand grounded using mortar and pestle in between two calcination stages to ensure homogeneity of the mixture. The calcined powders were uniaxially pressed into disks of 10 mm in diameter and 1.5 mm in thickness in Hydraulic press under 280 MPa using 4 wt.% polyvinyl alcohol (PVA) as a binder. The green pellets were sintered in closed alumina crucible at 1450 °C for 4 h in air after burning off the PVA at 600 °C for 1 h. The Ho-doped BCST ceramics so obtained were abbreviated as BCST0, BCST12, BCST14, BCST16, BCST18 and BCST20 in the increasing order of Ho contents. Prior to electrical measurements, sintered pellets were polished, silver-coated on flat surfaces before firing at 130 °C for 30 min to form electrodes. For piezoelectric studies, the ceramics were electrically poled for 1 h at room temperature in a silicone oil bath by subjecting it to 2–3 kV/mm dc electric field value.

The crystalline phase of the sintered pellets was examined by X-ray diffractometer (Bruker D8 Discover) with monochromatic Cu K α radiation ($\lambda = 1.5418$ Å) with 2θ ranging from 20° to 80°. Treor refinement program was performed with the Powder X software to determine the unit-cell volume and lattice parameters for each composition. The bulk density, ρ was measured using the Archimedes' principle. The relative density has been defined as the ratio of the bulk density ρ (mass per unit volume) of a ceramic to the theoretical density (ρ_t) calculated by the unit-cell volume obtained from XRD analysis and its molecular weight. SEM images were taken from polished and thermally etched

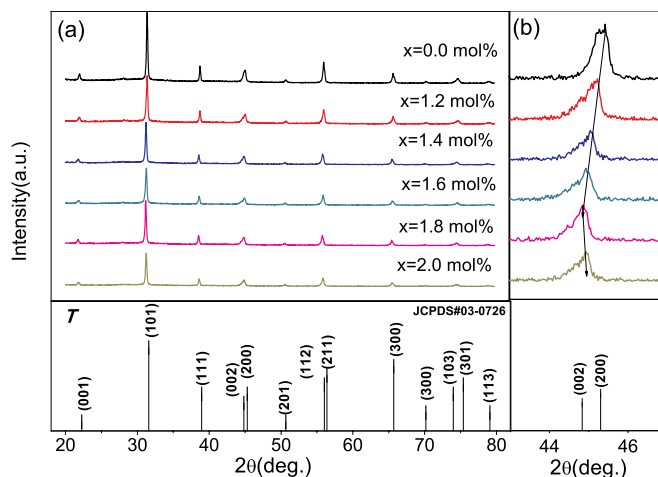


Fig. 1. (a) X-ray diffraction pattern of Ho doped BCST ceramics, and (b) magnified image of the XRD peaks around 45°.

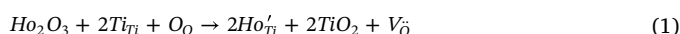
surfaces of the ceramics using scanning electric microscope (Joel JSM 6610L Japan) running at 30 kV. The temperature and frequency dependence of dielectric properties was measured at 1 kHz using an Impedance analyzer (Wayne Kerr 6500B Germany) with testing voltage of 1 V. The ferroelectric properties were examined using a computer controlled PE loop tracer system (Marine India) at room temperature and at a frequency of 50 Hz. The longitudinal piezoelectric charge coefficient (d_{33}) was measured with a quasi-static d_{33} Piezometer (Take Control, PM 25). The electromechanical coupling coefficient (k_p) was calculated for poled ceramic samples using resonance and anti-resonance method based on IEEE standards with the help of an Impedance analyzer.

3. Results and discussion

3.1. X-Ray diffraction analysis

Room temperature X-ray diffractograms of (Ba_{0.91}Ca_{0.09}Sn_{0.07}Ti_{0.93})O₃-xHo₂O₃ ceramic samples with $x = 0, 1.2, 1.4, 1.6, 1.8$ and 2.0 mol% are shown in Fig. 1a. These patterns confirm the presence of pure perovskite structure in all the samples with ferroelectric tetragonal phase having symmetry P4mm at room temperature. Absence of any secondary peaks in the XRD patterns indicates that Ho has completely diffused into the lattice of the host BCST system forming a homogeneous solid solution. Powder X software with Treor refinement program was used for indexing and analysis of these patterns [38], and JCPDS data with File no. 03–0726 was found to match well with all the observed XRD patterns.

Fig. 1b shows the magnified picture around the 45° peak of the ceramics, providing us with a clearer picture of peak shifting upon increasing Ho³⁺ content. It can be observed that upon increasing dopant concentration up to BCST18 there is a clear shifting of the diffraction peaks towards the lower angle whereas for BCST20 the peak shifting occurs slightly towards the higher angle. This shifting in peaks is attributed to the difference in ionic radius of the dopant and the host ion. Aliovalent dopant Ho³⁺ ion with IR- 0.9 Å replaces Ti⁴⁺ ion having smaller IR- 0.6 Å up to BCST18 leading to enlargement in unit cell volume as substantiated by the relevant increase in unit cell parameters shown in Table 1. Incorporation of Ho³⁺ as acceptor ions on Ti⁴⁺ sites is compensated by generation of ionized oxygen vacancies (V_{O}), also known as acceptor mechanism [36]. The related defect reaction up to 1.8 mol% Ho content is represented as follows:

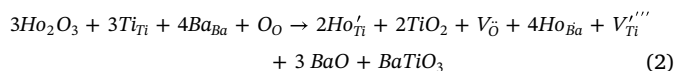


In this case, two Ho³⁺ ions displace two Ti⁴⁺ ions with the

Table 1
Crystallographic properties of Ho-doped $\text{Ba}_{0.91}\text{Ca}_{0.09}\text{Sn}_{0.07}\text{Ti}_{0.93}\text{O}_3$ ceramics.

Ho content	Crystallite	Strain	Lattice parameters (Å)			Cell volume
<i>x</i> (mol %)	size (Å)		<i>a</i>	<i>c</i>	<i>c/a</i>	(Å ³)
0.0	326	0.0158	3.9965	4.0126	1.0040	63.93
1.2	132	0.0073	4.0094	4.0112	1.0026	64.37
1.4	74	0.0053	4.0063	4.0114	1.0016	64.39
1.6	65	0.0038	4.0176	4.0259	0.9996	64.74
1.8	76	0.0074	4.0342	4.0625	1.0071	65.59
2.0	154	0.0103	4.0216	4.0534	1.0068	65.33

generation of one oxygen vacancy. The effect of occupying B-site (Ti site) by the larger Ho ion is evidently reflected by the increased unit cell volume till BCST18. However, a slight decrease in the cell volume is observed for the ceramic with Ho content greater than 1.8 mol%. This switch over can be accounted for by the change in the incorporation mechanism from acceptor mechanism to self-compensation mechanism. During the self-compensation mechanism, Ho^{3+} ions enter the Ba-sites as acceptors with oxygen vacancies and also compensate for the excess positive charge with creation of titanium vacancies ($V_{\text{Ti}}^{\prime\prime\prime}$) [39]. The defect equation concerning Ho incorporation via self-compensation mechanism is as follows:



In this case, two Ho^{3+} ions again displace two Ti^{4+} sites via generating one oxygen vacancy along with substitution of four Ho^{3+} ions at two Ba^{2+} sites via creating one Ti vacancy. The substitution at A-site (Ba, IR 1.6 Å) ion by a smaller Ho^{3+} ion with Ti vacancy can lead to the shrinkage of unit cell volume for higher Ho doped systems (BCST20). This in turn suggests that Ho^{3+} enters BCST structure preferentially as an acceptor at Ti-Sites. This also indicates that the solubility of Ho at the Ba^{2+} sites is lower (< 1.2 mol%) than pure BT system in air [35]. The systemic variation in crystallographic parameters upon the addition of Ho in BCST system is recorded in Table 1.

Due to substitution of Ti ion (B-site) with Ho ion, there is an appreciable increase observed in cell volume from 63.93 Å³ for undoped BCST0 sample to a value 65.59 Å³ for doped BCST18 sample. Lattice parameters *a*, *b* and *c* show increasing trend with increasing Ho content supporting the increased cell volume. In addition, tetragonality (*c/a*) shows an interesting systematic variation suggesting the occurrence of structural changes within the system as a result of varying dopant concentration. Tetragonality drops with rising Ho concentration to a minimum of 0.9996 for BCST16 and then upsurges for higher Ho content.

Williamson-Hall method was used to calculate average crystallite size *L* and lattice strain η using the following equation [40,41]:

$$\beta \cos \theta = k\lambda/L + \eta \sin \theta$$

where β is the FWHM of the peak profile, *k* being the constant with its value taken as 0.9, θ the diffraction angle, and λ (Cu K α : $\lambda = 1.5418$ Å) the wavelength of X-ray. Systematic variations in crystallite size and lattice strain are plotted with Ho content as shown in Fig. 2. A drastic reduction in crystallite size from 326 Å for the undoped sample to a low value of 65 Å is observed for BCST16 before it increases beyond 1.6 mol % Ho content. Similar trend is observed for lattice strain of the ceramics.

It can be observed that variations in crystallite size and lattice strain with Ho content are similar to that of *c/a* ratio observed. Ceramics with large crystallite size and strain have strong influence on crystalline structure which is manifested in terms of the tetragonality (*c/a*) change. Large strain values possessed by the ceramic system could be considered as the origin for its observed high tetragonality. Similar dependence of phase structure on lattice strain is reported by researchers

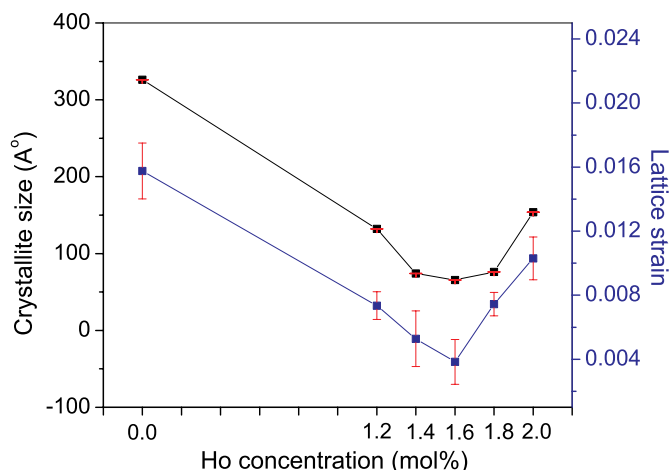


Fig. 2. Plots showing dependence of crystallite size and lattice strain, on Ho^{3+} content in BCST.

in PZT system [42,43], and also observed in lead free KNN ceramic system [44]. With increase in Ho content up to 1.6 mol% i.e. BCST16, microstrain and tetragonality tend to fall as a consequence of release of the internal stress accompanying the enlargement of unit cell volume. The slight rise in these parameters for the higher dopant contents can be for the same reason related to the associated shrinkage in unit cell volume.

3.2. Surface morphology

SEM micrographs of thermally etched surfaces of Ho doped BCST ceramic samples are shown in Fig. 3. It is evident that the microstructure exhibits appreciable changes with the increase of Ho content. The sample with no Ho content viz., BCST0, shown in Fig. 3a has dense and homogeneous microstructure with average grain size of about 16 μm . However as seen in Fig. 3b–e, there is a significant drop in the average grain size for the Ho doped BCST samples. With increasing Ho^{3+} content, the grain size drastically decreases to a minimum value of ~ 0.7 μm at 1.6 mol% Ho^{3+} content indicating the suppression of grain growth in Ho modified BCST ceramics. This suppression in grain size might be due to non-uniform distribution of Ho^{3+} near grain boundary regions restricting their mobility that weakens the mass transportation and results in grain growth inhibition [45]. The charge mismatch between the dopant as solute and grain boundaries causes build-up of a solute cloud. As the grain boundary starts to move, the dopant concentration profile becomes asymmetric due to difference in diffusivity between the host and dopant ions. This asymmetry leads to a solute drag on the grain boundary thus reducing the driving force for migration [46,47]. The developing restraint in grain boundary migration gives rise to the reduction in grain size with increasing the dopant concentration.

Fig. 4(a–f) shows the histogram representation of distribution of grain size with different Ho concentrations. It is clearly seen that undoped BCST system has relatively uniform dense microstructure whereas porous and non-uniform microstructure distribution is predominant for doped system ($x \geq 1.2$ mol%). This substantial effect of Ho on surface morphology and microstructure of BCST results in the fall of density of the ceramics. Bulk densities of the ceramics as measured using Archimedes' principle are listed in Table 2. The bulk density shows a declining trend with increasing Ho content. It decreases from 93% of the theoretical density (TD) for BCST0 to 81% of the TD for heavily doped BCST20 system. The study thus reveals that addition of Ho significantly affects the microstructure of BCST ceramics. No deliquescence was observed in the ceramics when exposed to water for 24 h.

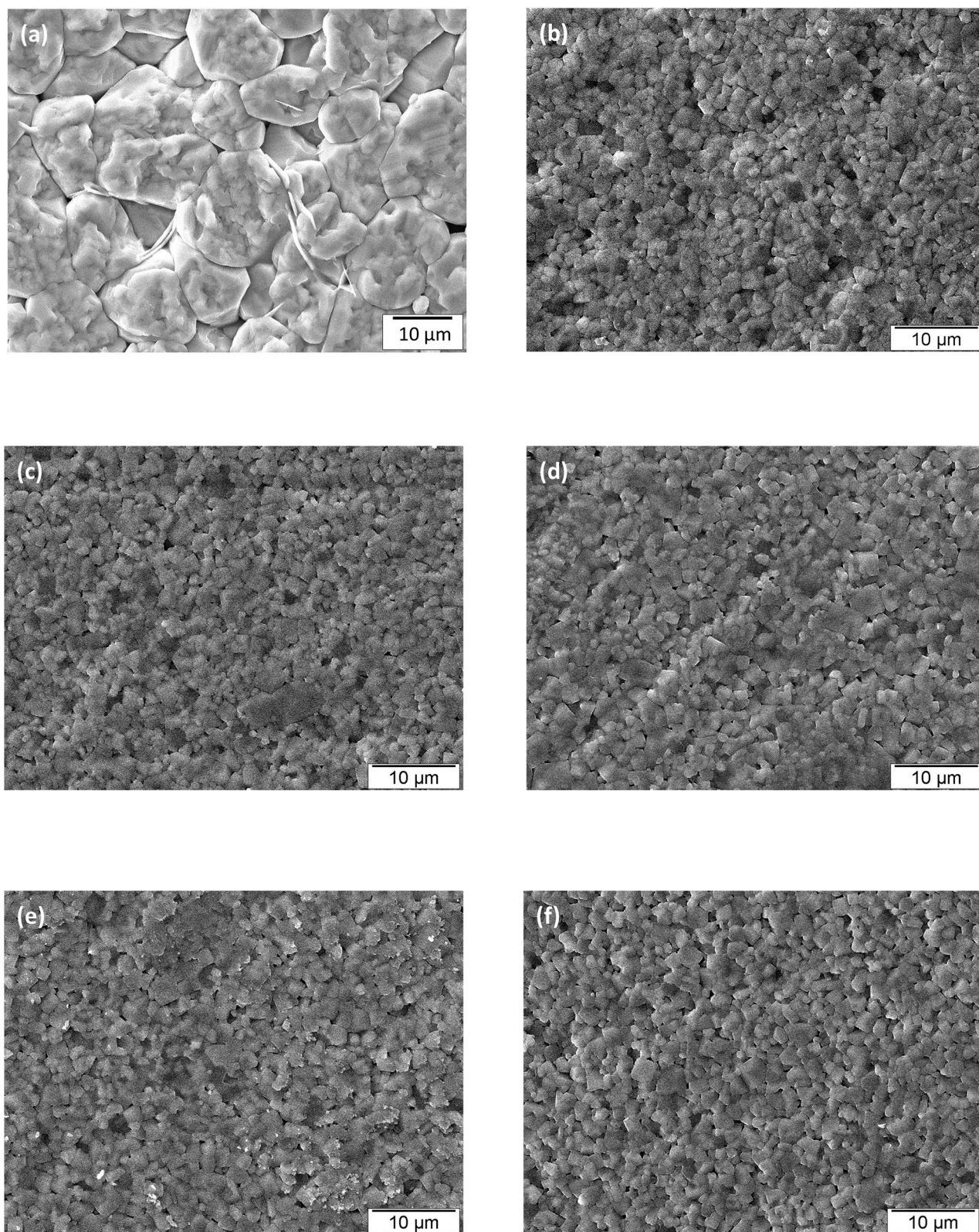


Fig. 3. SEM micrographs of Ho substituted ceramics with (a) $x = 0$ mol%, (b) $x = 1.2$ mol%, (c) $x = 1.4$ mol%, (d) $x = 1.6$ mol%, (e) $x = 1.8$ mol%, and (f) $x = 2.0$ mol%.

3.3. Dielectric studies

Frequency dependence of room temperature dielectric constant (ϵ_{rt}) and dissipation factor ($\tan\delta$) with various Ho^{3+} concentration are illustrated in Fig. 5(a, b). Also the dielectric properties for all prepared

ceramic systems with different Ho concentrations are summarized in Table 2. It is seen that there is a notable reduction detected in ϵ_{rt} values from BCST0 ($\epsilon_{rt} \sim 3997$) to BCST20 ($\epsilon_{rt} \sim 800$) ceramic system. It exhibits a clear declining trend with an increase in Ho content, which is consistent with the degrading density (Table 2). The observed large

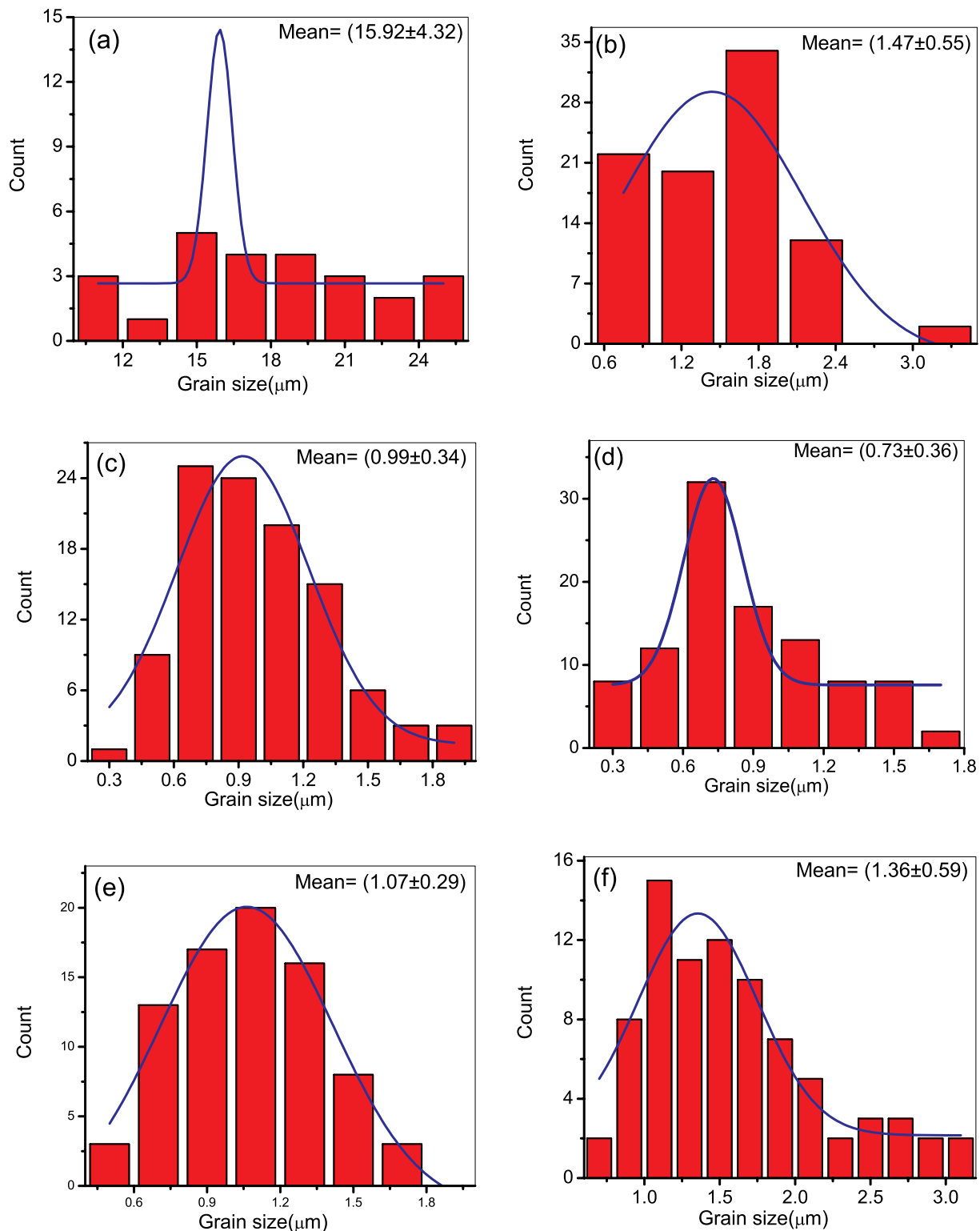


Fig. 4. Histogram representation of distribution of grain size of BCST system with (a) $x = 0$ mol%, (b) $x = 1.2$ mol%, (c) $x = 1.4$ mol%, (d) $x = 1.6$ mol%, (e) $x = 1.8$ mol%, and (f) $x = 2.0$ mol% Ho content.

dielectric constant value for BCST0 can be attributed to its homogenous dense microstructure. Such dependence of dielectric constant on density is also observed in many other systems [48,49]. The observed decrease in dielectric constant value may also be a consequence of shrinking grain size with rising Ho concentration. Crystallite size tends to decrease with decreasing grain size which in turn makes crystallite size comparable with the domain wall width leading to domain wall

pinning effect. This would inhibit domain wall motion resulting in degradation of dielectric constant value with grain size.

While all the ceramics show a decreasing trend in ϵ_r with increasing frequency, the fall of ϵ_r values at higher frequencies becomes steeper till BCST14 beyond which the decline is less abrupt. The decreasing trend of dielectric constant at higher frequencies is commensurate with the rise in $\tan \delta$ values up to BCST14 at higher frequencies. The increase

Table 2
Dielectric properties of various Ho-doped $\text{Ba}_{0.91}\text{Ca}_{0.09}\text{Sn}_{0.07}\text{Ti}_{0.93}\text{O}_3$ ceramics.

Ho content (mol%)	0	1.2	1.4	1.6	1.8	2.0
Bulk Density (g/cm^3)	5.62	5.42	5.29	5.19	4.92	4.78
Relative Density (%)	93.15	91.07	88.72	87.54	83.99	81.17
Porosity (%)	6.85	8.93	11.28	12.46	16.01	18.83
ϵ_{rt} , 30 °C	3997	2936	2380	2459	1678	807
ϵ_m at T_c	5544	3147	2489	2513	1736	814
Curie temperature, T_c (°C)	58	53	49	43	39	35
Dielectric loss, $\tan \delta$	0.044	0.021	0.025	0.022	0.023	0.018

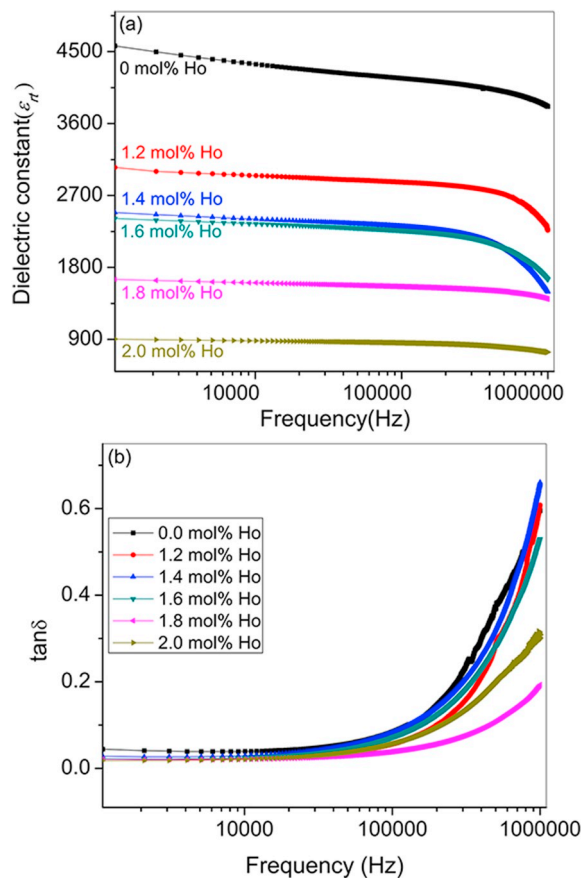


Fig. 5. Frequency dependence of (a) dielectric constant (ϵ_r), and (b) dissipation factor ($\tan \delta$) at room temperature, for Ho doped BCST system.

in $\tan \delta$ at higher frequencies is suggestive of the increasing presence of conductive losses in the system which results in the observed declining trend of dielectric constant. It can also be remarked that at lower frequencies Ho doped BCST systems show low $\tan \delta$ values in the range 0.018–0.025, much less than that of undoped system BCSTO (Table 2).

Fig. 6a shows temperature dependence of dielectric constant (ϵ) curves for Ho doped $\text{Ba}_{0.91}\text{Ca}_{0.09}\text{Sn}_{0.07}\text{Ti}_{0.93}\text{O}_3$ ceramics measured over the temperature range 25°–150 °C at 1 kHz frequency. The major characteristic peaks observed in each curve indicates the transition temperature from ferroelectric to paraelectric phase - the Curie temperature T_c . This temperature along with room temperature dielectric constant (ϵ_{rt}) tends to decrease with increasing Ho concentration in BCST system, as seen in Fig. 6a. The observed decrease in T_c values might be a result of B-site (Ti-ions) substitution with Ho ions. This substitution leads to an increase in unit cell volume with simultaneous decrease in available Ti-O bonds which in turn weakens Ti-O interaction within TiO_6 octahedral of the perovskite structure, giving rise to decrease in Curie temperature.

Interestingly, higher incorporation of Ho^{3+} ions into the system

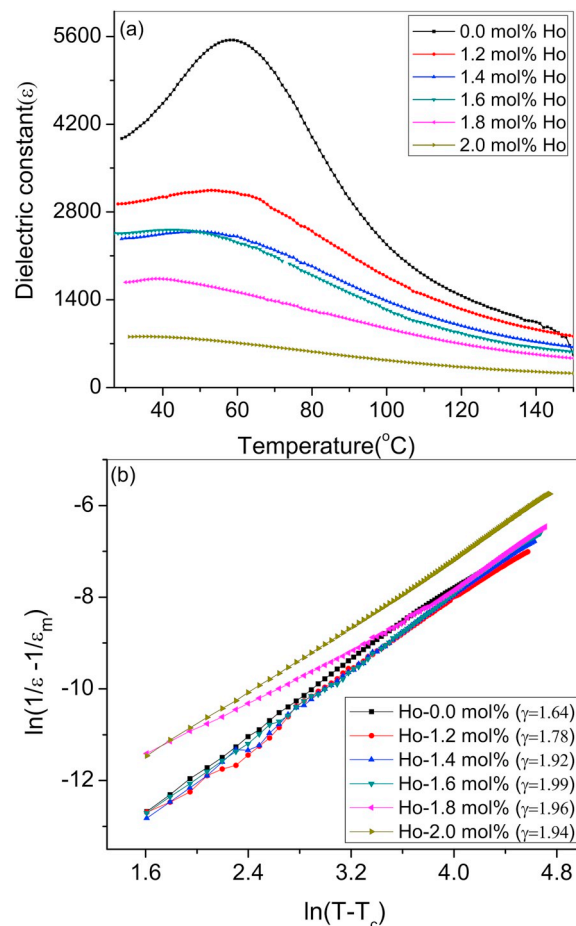


Fig. 6. (a) Temperature dependence of dielectric constant (ϵ), and (b) plot showing variation of $\ln(1/\epsilon - 1/\epsilon_m)$ with $\ln(T-T_c)$ for BCST ceramics having different Ho^{3+} contents, measured at 1 kHz frequency.

induces a broadening effect on this transition peak. This broadening is further analyzed by calculating the diffuseness parameter using modified Curie Weiss law. The dielectric constants at temperatures higher than T_c have been fitted to this model, proposed by Uchino and Nomura [50]:

$$1/\epsilon - 1/\epsilon_m = (T - T_m)^\gamma / C, \quad (T > T_m) \quad (T > T_m) \quad (3)$$

where ϵ_m is the maximum value of dielectric constant at temperature T_m . Diffusivity γ and C are the constants, with $1 < \gamma < 2$ where γ determines the degree of diffuseness of the phase transition. The value of γ is equal to 1 corresponding to a completely ordered phase transition whereas γ is equal to 2 for a completely diffused system expected on the basis of a local compositional fluctuation model.

Fig. 6b shows the plots of $\ln(1/\epsilon - 1/\epsilon_m)$ versus $\ln(T - T_m)$ for the ceramics. The values of γ as determined from the slopes of the graphs in Fig. 6b exhibit a systematic change with increasing Ho content in the ceramics. It can be noted that γ increases drastically from 1.64 for BCST0 to 1.99 for BCST16, and then slightly decreases to 1.94 for BCST20 indicating a systematic change induced in the diffuseness of the ferroelectric transition peaks at different Ho content. It is observed that the diffuseness of the dielectric peak increases while a decrease in T_c towards the room temperature is observed with Ho doping in BCST system. Both of these phenomena are responsible for transferring a large fraction of paraelectric phase near the room temperature. The increasing presence of paraelectric component at the room temperature is also evidenced by the observed variations of tetragonality and grain size with increasing Ho content (Table 1). It is a general understanding that the diffuseness of the dielectric peak has an origin in local

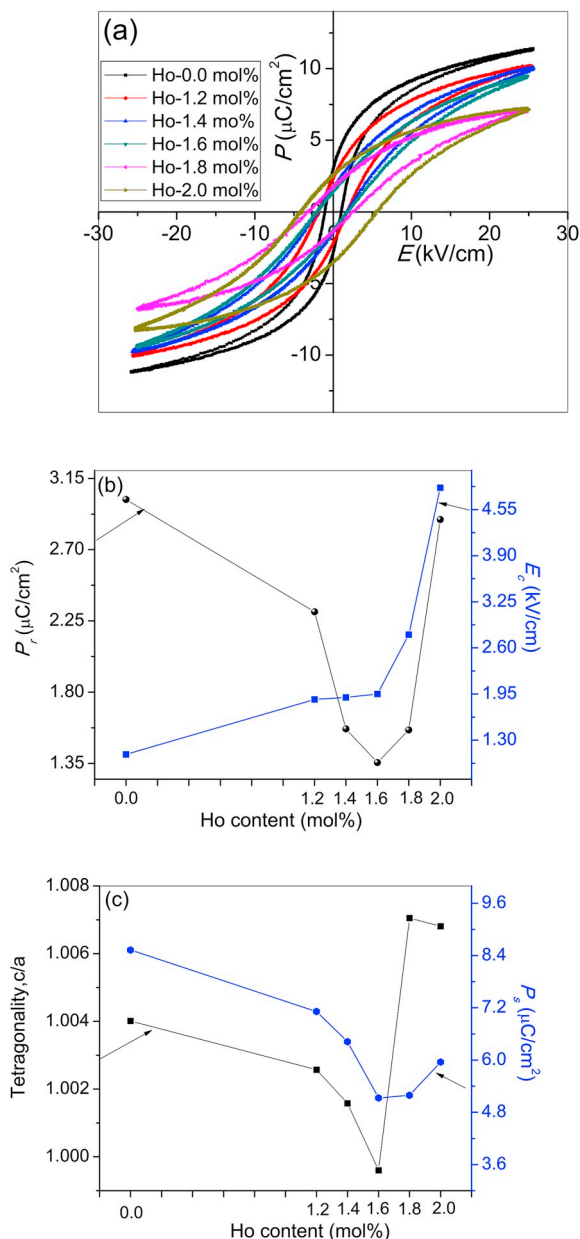


Fig. 7. (a) Room temperature P-E hysteresis curves measured at 50 Hz, (b) plots of P_r and E_c versus x , and (c) plots of P_s and tetragonality, versus x , for Ho doped BCST ceramics.

compositional fluctuation that gives rise to different micro-regions with slightly varying individual ferroelectric-paraelectric phase transitions [51,52]. These micro-regions might have increased with decreasing grain size and crystallite size with Ho doping and thus increased the diffused behavior of dielectric peak of the material [52].

3.4. Ferroelectric studies

Room temperature PE hysteresis loops for the Ho doped BCST ceramic samples, measured at 50 Hz are shown in Fig. 7a. The variations in remnant polarization (P_r) and coercive field (E_c) values determined from these loops are depicted in Fig. 7b. It can be inferred that with the increase of Ho^{3+} concentration, the value of P_r follows a decreasing trend towards the lowest value at $x = 1.6$ mol%, after which it upsurges. This suggests that ferroelectricity of the ceramics weakens when Ho^{3+} substitutes the Ti-site and strengthens when it occupies Ba-site.

Decrease in ferroelectricity in ceramic system is closely related to changes observed in grain size. There have been reports which suggest the weakening of the ferroelectric properties as a result of decreasing grain size in the ceramics [53–55]. In general, these properties directly depend on ferroelectric domain structure, nucleation and its mobility. As the grain size decreases the energy barrier for ferroelectric domain switching increases along with increased grain boundary effect in smaller grains. These effects subsequently hinder the polarization switching and suppress the ferroelectric behavior under an applied electric field in small sized grains [56]. It has also been observed that polarization reversal of ferroelectric domains is easier in large sized grains as compared to small ones [48]. Also this degradation in ferroelectric property for Ho doped ceramic samples in view of its low P_r value is also a result of their low T_c which ensures the presence of partial paraelectric phase at room temperature. It can be also noted that there is an overall growth in E_c values from 1.09 kV/cm to 4.86 kV/cm as the Ho content increases from BCST0 and BCST20. This indicates that the ceramic system changes its ferroelectric nature towards hard ferroelectric behavior at higher Ho^{3+} concentration. The elevated coercive field value is also closely related with the decreased grain size. As grain size decreases, back field originates due to increased percentage of grain boundary regions which opposes the switching during field loading [57].

Ferroelectricity originates from the structural changes occurring within the system. In order to emphasize these changes, plots showing variations in spontaneous polarization (P_s) and tetragonality (c/a) with various Ho^{3+} content are presented in Fig. 7c. It is seen that the observed trend of spontaneous polarization (P_s) is in agreement with that of tetragonality. It has been reported for the perovskite type ferroelectric materials that its tetragonality (c/a) can significantly affect their ferroelectric properties such as P_s and T_c [58]. P_s values are generally expected to rise in the material having high tetragonality due to ease in orientation of dipoles along their respective polar axes. This might be a plausible reason for the rise in P_r values at higher dopant contents ($x = 1.8$ and 2.0 mol%). Another contributory factor towards the upsurge of P_r is the appearance of cationic vacancy defects as a result of self-compensation mechanism dominance at higher concentration. These defects facilitate domain motion during switching as they themselves act as nucleating site for new domains [59]. However, ceramics with these concentrations also show hysteresis loops with larger area and as a result hysteresis losses are large too.

3.5. Piezoelectric studies

Effective changes in piezoelectric coefficient d_{33} and electro-mechanical coupling coefficient k_p with Ho concentration are depicted in Fig. 8. Both these parameters follow a decreasing trend for increasing Ho concentration in BCST system. As seen in Fig. 8, the piezoelectric properties attain the highest values for undoped BCST0 ($d_{33} = 102$ pC/N, $k_p = 22\%$) and the least values for heavily doped BCST20 ($d_{33} = 38$ pC/N, $k_p = 6\%$).

Thermodynamic theory suggests that the piezoelectric constant d_{33} of a ferroelectric material is dependent on polarization and dielectric permittivity which can be expressed [60] as:

$$d_{33} = 2Q_{11}\epsilon_0\epsilon_r P_s$$

where Q_{11} is the electrostrictive coefficient, ϵ_r the room temperature dielectric constant and P_s the spontaneous polarization. Normally Q_{11} does not change appreciably due to doping as it is mainly dependent on the domain structure which does not undergo appreciable changes with doping. Therefore the observed decrease in d_{33} with increasing x (Fig. 8) in BCST system could be mainly attributed to the associated change in ϵ_r and P_s (Figs. 5a and 7c). In addition to above factors the presence of phase transition T_c occurring near the room temperature due to rise in Ho^{3+} content further weakens ferroelectricity and thus

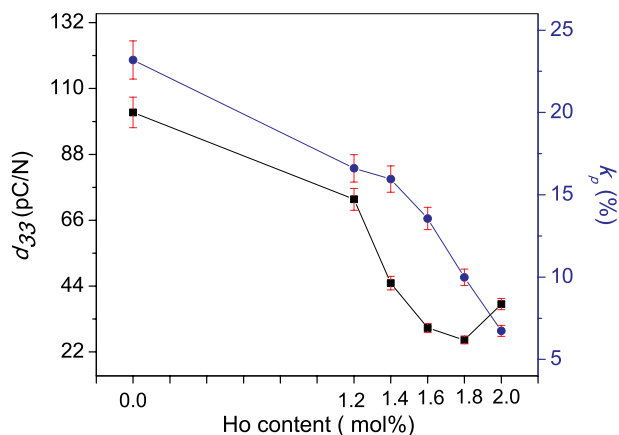


Fig. 8. Variations of d_{33} and k_p as functions of Ho-content in BCST.

piezoelectricity.

The variation in d_{33} observed correlates well with the changes detected in the density of the ceramics with Ho doping. This reduction in piezoelectric properties may be attributed to cumulative changes observed in grain size and the density of the ceramics. There are reports of improvement of piezoelectric properties in other perovskite systems having suitably large crystallite/grain size [61,62]. With smaller grains/crystallite size there is a probability of suppression of lattice distortion arising from cubic lattice which deteriorates piezoelectric behavior of a material. Another factor which could contribute in degrading piezoelectric behavior is the difficulty in domain wall motion as a consequence of increased coercive field (E_c) values with Ho concentration and also due to domain wall pinning effect arising due to corresponding reduction in crystallite size with grain size.

The observed reduction of piezoelectric nature for $x \geq 1.2$ mol% Ho content thus supports the presence of appropriate grain size for a material to possess good piezoelectric properties; similar observation has been reported for BaTiO₃ ceramic system [61]. There are similar reports on donor doped PZT system [62] which show degrading piezoelectric properties due to restricted domain wall motion accounted to their smaller grain size. Further it can be noted that the observed decrease of d_{33} is also in accordance with the variation of strain (Table 1) existing in the ceramics up to $x \leq 1.6$ mol%. For instance, the small strain of 0.0038 in BCST16 is not enough to create anisotropic instability in the system leaving it hardly with any TiO₆ octahedral distortion in the perovskite structure. This ensures rigid Ti off-center movement which further weakens the spontaneous polarization and hence piezoelectric properties of the ceramic system. The overall degradation in the piezoelectric properties may be due to the existence of a critical grain size, poorer density and the presence of Curie temperature T_c too close to room temperature.

4. Conclusion

In the present work, Barium Titanate based lead-free (Ba_{0.91}Ca_{0.09}Sn_{0.07}Ti_{0.93})O₃-xHo₂O₃ ($x = 0, 1.2, 1.4, 1.6, 1.8$ and 2.0 mol %) piezoceramics were synthesized by traditional ceramic processing sintering technique. Presence of pure perovskite structure with tetragonal symmetry was confirmed by XRD analysis for all the ceramic compositions prepared. It can be concluded that under oxidizing condition, the solubility of Ho ion at Ba-site in BCST ceramic system is lower than the reported solubility in pure BT system as it tends to substitute Ti-site for $x \geq 1.2$ mol%. The mechanism for Ho-substitution at Ti-sites switches from acceptor mechanism to self-compensation mode at about 1.8 mol% Ho content. This brings a systematic change in unit cell volume, crystallite and lattice strains of the ceramics. The gradual decrease in room-temperature dielectric constant (ϵ_{rt}) and Curie temperature shift towards RT with rise in Ho content in BCST

system exhibits strong dependence of dielectric properties on the Ho content. Increasing Ho content significantly reduces grain size by inhibiting grain growth in the ceramics thereby inducing hard ferroelectric nature in them. The bulk density, piezoelectric charge coefficient d_{33} and electromechanical coupling factor k_p decreases as Ho³⁺ concentration increases from 0 to 2 mol%. The gradual degradation in piezoelectric properties with rise in Ho³⁺ content in the ceramics is attributed to the poorer density, refined grains, decreasing dielectric constant and declining ferroelectric properties.

Declarations of interest

None.

Acknowledgment

This work is financially supported by the Department of Science and Technology, India, under the Research Project No. EMR/2014/284. We acknowledge the directors of Solid State Physics Laboratory, Delhi for providing facilities for some measurements.

References

- [1] L. Gao, H. Guo, S. Zhang, C. Randall, Base metal co-fired multilayer piezoelectrics, *Actuators* 5 (2016) 8 <https://doi.org/10.3390/act5010008>.
- [2] C.H. Hong, H.P. Kim, B.Y. Choi, H.S. Han, J.S. Son, C.W. Ahn, W. Jo, Lead-free piezoceramics-where to move on? *J. Mater.* 2 (1) (2016) 1–24 <https://doi.org/10.1016/j.jmat.2015.12.002>.
- [3] I. Coondoo, N. Panwar, A. Kholkin, Lead-Free piezoelectrics: current status and perspectives, *J. Adv. Dielect.* 3 (2013) 1330002 <https://doi.org/10.1142/S2010135X13300028>.
- [4] G. Shirane, K. Suzuki, Phase transitions in solid solutions of PbZrO₃ and PbTiO₃ (II) X-ray study, *J. Phys. Soc. Jpn.* 7 (1) (1952) 12–18 <https://doi.org/10.1143/JPSJ.7.12>.
- [5] EU Directive 2002/95/EC of the European Parliament and of the Council of 27 January 2003 on the restriction of the use of certain hazardous substances in electrical and electronic equipment (RoHS), *Off. J. Eur. Union* 46 (L37) (2003) 19 http://europa.eu.int/eur-lex/pri/en/oj/dat/2003/l_037/l_03720030213en00190023.pdf.
- [6] J.F. Li, K. Wang, F.Y. Zhu, L.Q. Cheng, F.Z. Yao, (K, Na) NbO₃-based lead-free piezoceramics: fundamental aspects, processing technologies, and remaining challenges, *J. Am. Ceram. Soc.* 96 (12) (2013) 3677–3696 <https://doi.org/10.1111/jace.12715>.
- [7] J. Wu, D. Xiao, J. Zhu, Potassium-sodium niobate lead-free piezoelectric materials: past, present, and future of phase boundaries, *Chem. Rev.* 115 (7) (2015) 2559–2595 <https://doi.org/10.1021/cr5006809>.
- [8] T. Zheng, J. Wu, D. Xiao, J. Zhu, Recent development in lead-free perovskite piezoelectric bulk materials, *Prog. Mater. Sci.* 98 (2018) 552–624 <https://doi.org/10.1016/j.pmatsci.2018.06.002>.
- [9] A. Reyes-Montero, F. Rubio-Marcos, L. Pardo, A. Del Campo, R. López-Juárez, M.E. Villafuerte-Castrejón, Electric field effect on the microstructure and properties of Ba_{0.9}Ca_{0.1}Ti_{0.9}Zr_{0.1}O₃ (BCTZ) lead-free ceramics, *J. Mater. Chem.* 6 (13) (2018) 5419–5429 <https://doi.org/10.1039/C7TA09798K>.
- [10] K. Xu, J. Li, X. Lv, J. Wu, X. Zhang, D. Xiao, J. Zhu, Superior piezoelectric properties in potassium-sodium niobate lead-free ceramics, *Adv. Mater.* 28 (38) (2016) 8519–8523 <https://doi.org/10.1002/adma.201601859>.
- [11] C. Zhao, H. Wu, F. Li, Y. Cai, Y. Zhang, D. Song, J. Zhu, Practical high piezoelectricity in barium titanate ceramics utilizing multiphase convergence with broad structural flexibility, *J. Am. Ceram. Soc.* 140 (45) (2018) 15252–15260 <https://doi.org/10.1021/jacs.8b07844>.
- [12] W. Liu, X. Ren, Large piezoelectric effect in Pb-free ceramics, *Phys. Rev. Lett.* 103 (2009) 257602 <https://doi.org/10.1103/PhysRevLett.103.257602>.
- [13] J. Rödel, W. Jo, K.T.P. Seifert, E.M. Anton, T. Granzow, D. Damjanovic, Perspective on the development of lead-free piezoceramics, *J. Am. Ceram. Soc.* 92 (2009) 1153–1177 <https://doi.org/10.1111/j.1551-2916.2009.03061.x>.
- [14] Y. Saito, H. Takao, T. Tani, T. Nonoyama, K. Takatori, T. Homma, T. Nagaya, M. Nakamura, Lead-free piezoceramics, *Nature* 432 (2004) 84–87 <https://doi.org/10.1038/nature03028>.
- [15] T. Takenaka, H. Nagata, Current status and prospects of lead-free piezoelectric ceramics, *J. Eur. Ceram. Soc.* 25 (2005) 2693–2700 <https://doi.org/10.1016/j.jeurceramsoc.2005.03.125>.
- [16] R. Bechmann, Elastic, piezoelectric, and dielectric constants of polarized barium titanate ceramics and some applications of the piezoelectric equations, *J. Acoust. Soc. Am.* 28 (3) (1956) 347–350 <https://doi.org/10.1121/1.1908324>.
- [17] Y. Huang, C. Zhao, X. Lv, H. Wang, J. Wu, Multiphase coexistence and enhanced electrical properties in (1-x-y)BaTiO₃-xCaTiO₃-yBaZrO₃ lead-free ceramics, *Ceram. Int.* 43 (16) (2017) 13516–13523 <https://doi.org/10.1016/j.ceramint.2017.07.057>.
- [18] X. Cheng, M. Shen, Enhanced spontaneous polarization in Sr and Ca co-doped BaTiO₃ ceramics, *Solid State Commun.* 141 (11) (2007) 587–590 <https://doi.org/>

- 10.1016/j.ssc.2007.01.009.
- [19] A. Kirianov, T. Hagiwara, H. Kishi, H. Ohsato, Effect of Ho/Mg ratio on formation of core-shell structure in BaTiO₃ and on dielectric properties of BaTiO₃ ceramics, *Jpn. J. Appl. Phys.* 41 (11S) (2002) 6934 <https://doi.org/10.1143/JJAP.41.6934>.
- [20] Y. Yao, C. Zhou, D. Lv, D. Wang, H. Wu, Y. Yang, X. Ren, Large piezoelectricity and dielectric permittivity in BaTiO₃-xBaSnO₃ system: the role of phase coexisting, *EPL-Europhys. Lett.* 98 (2) (2012) 27008 <https://doi.org/10.1209/0295-5075/98/27008>.
- [21] W.H. Payne, V.J. Tennery, Dielectric and structural investigations of the system BaTiO₃-BaHfO₃, *J. Am. Ceram. Soc.* 48 (1965) 413–417 <https://doi.org/10.1111/j.1151-2916.1965.tb14779.x>.
- [22] M. Chen, Z. Xu, R. Chu, Y. Liu, L. Shao, W. Li, S. Gong, G. Li, Polymorphic phase transition and enhanced piezoelectric properties in (Ba_{0.9}Ca_{0.1})(Ti_{1-x}Sn_x)O₃ lead-free ceramics, *Mater. Lett.* 97 (2013) 86–89 <https://doi.org/10.1016/j.matlet.2012.12.067>.
- [23] L.F. Zhu, B.P. Zhang, X.R. Zhao, L. Zhao, F.Z. Yao, X. Han, P.F. Zhou, J.F. Li, Phase transition and high piezoelectricity in (Ba,Ca)(Ti_{1-x}Sn_x)O₃ lead-free ceramics, *Appl. Phys. Lett.* 103 (7) (2013) 072905 <https://doi.org/10.1063/1.4818732>.
- [24] M. Chen, Z. Xu, R. Chu, H. Qiu, M. Li, Y. Liu, W. Li, Enhanced piezoelectricity in broad composition range and the temperature dependence research of (Ba_{1-x}Ca_x)(Ti_{0.95}Sn_{0.05})O₃ piezoceramics, *Phys B* 433 (2014) 43–47 <https://doi.org/10.1016/j.physb.2013.10.014>.
- [25] M.T. Buscaglia, V. Buscaglia, M. Viviani, P. Nanni, M. Hanuskova, Influence of foreign ions on the crystal structure of BaTiO₃, *Jpn. J. Appl. Phys.* 40 (2001) 255–258 [https://doi.org/10.1016/S0955-2219\(00\)00076-5](https://doi.org/10.1016/S0955-2219(00)00076-5).
- [26] Y. Tsur, D.T. Dunbar, C.A. Randall, Crystal and defect chemistry of rare earth cations in BaTiO₃, *J. Electroceram.* 7 (2001) 25–34 <https://doi.org/10.1023/A:101221882>.
- [27] Y. Tsur, A. Hitomi, I. Scrymgeour, C.A. Randall, Site occupancy of rare-earth cations in BaTiO₃, *Jpn. J. Appl. Phys.* 40 (1) (2001) 255–258 <https://doi.org/10.1143/JJAP.40.255>.
- [28] H. Saito, H. Chazono, H. Kishi, N. Yamaoka, X7R multilayer ceramic capacitors with nickel electrodes, *Jpn. J. Appl. Phys.* 30 (2001) 2307 <https://doi.org/10.1143/JJAP.30.2307>.
- [29] M.T. Buscaglia, V. Buscaglia, M. Viviani, P. Nanni, Atomistic simulations of dopant incorporation in barium titanate, *J. Am. Ceram. Soc.* 84 (2) (2001) 376–384 <https://doi.org/10.1111/j.1151-2916.2001.tb00665.x>.
- [30] S. Sato, Y. Nakano, A. Sato, T. Nomura, Mechanism of improvement of resistance degradation in Y-doped BaTiO₃ based MLCCs with Ni electrodes under highly accelerated life testing, *J. Eur. Ceram. Soc.* 19 (1999) 1061–1065 [https://doi.org/10.1016/S0955-2219\(98\)00374-4](https://doi.org/10.1016/S0955-2219(98)00374-4).
- [31] Y. Tsur, A. Hitomi, I. Scrymgeour, C.A. Randall, Dielectric and piezoelectric ceramics 8th US-Japan seminar, *Dielectr. Piezoelectr. Ceram.* 44 (1997).
- [32] C.H. Kim, K.J. Park, Y.J. Yoon, M.H. Hong, J.O. Hong, K.H. Hur, Role of yttrium and magnesium in the formation of core-shell structure of BaTiO₃ grains in MLCC, *J. Eur. Ceram. Soc.* 28 (6) (2008) 1213–1219 <https://doi.org/10.1016/j.jeurceramsoc.2007.09.042>.
- [33] Y. Wang, L. Li, J. Qi, et al., Ferroelectric characteristics of ytterbium-doped barium zirconium titanate ceramics, *Ceram. Int.* 28 (2002) 657–661 [https://doi.org/10.1016/S0272-8842\(02\)00023-8](https://doi.org/10.1016/S0272-8842(02)00023-8).
- [34] S. Shirasaki, M. Tsukioka, H. Yamamura, et al., Origin of semiconducting behavior in rare-earth doped barium titanate, *Solid State Commun.* 19 (1976) 721–724 [https://doi.org/10.1016/0038-1098\(76\)90905-4](https://doi.org/10.1016/0038-1098(76)90905-4).
- [35] D. Makovec, Z. Samardžija, M. Drogenik, Solid solubility of holmium, yttrium, and dysprosium in BaTiO₃, *J. Am. Ceram. Soc.* 87 (7) (2004) 1324–1329 <https://doi.org/10.1111/j.1151-2916.2004.tb07729.x>.
- [36] D. Makovec, Z. Samardžija, M. Drogenik, The solid solubility of holmium in BaTiO₃ under reducing conditions, *J. Am. Ceram. Soc.* 89 (10) (2006) 3281–3284 <https://doi.org/10.1111/j.1151-2916.2006.01204.x>.
- [37] R. Chitra, A. Laishram, Vashishtha, et al., Effect of holmium doping on structural, electrical and piezoelectric properties of lead-free (Ba,Ca)(Ti,Sn)O₃ ceramics, *J. Mater. Sci. Mater. Electron.* (2019) 1–8 <https://doi.org/10.1007/s10854-019-00682-w>.
- [38] C. Dong, Powder X: windows-95-based program for powder X-ray diffraction data processing, *J. Appl. Crystallogr.* 32 (4) (1999) 838–838 <https://doi.org/10.1107/S0021889899003039>.
- [39] Y.Z.A. Leyva, Y.L. Ruiz, J. Anglada-Rivera, F.G. Zayas, Analysis of the structural properties in Erbium doped barium titanate by molecular dynamics simulations, *Rev. Cubana Quím.* 24 (3) (2015) 261–265.
- [40] B.D. Cullity, Phase diagram determination, *Elements of X-ray Diffraction*, Addison and Wesley Publishing Company Inc., MA, 1978, pp. 356–359.
- [41] G.K. Williamson, W.H. Hall, X-ray line broadening from filed aluminium and wolfram, *Acta Metall.* 1 (1953) 22–31 [https://doi.org/10.1016/0001-6160\(53\)90006-6](https://doi.org/10.1016/0001-6160(53)90006-6).
- [42] C. Wu, W. Duan, X.W. Zhang, Z. Liu, Effects of hydrostatic pressure on Pb(Zr_{1-x}Ti_x)O₃ near the morphotropic phase boundary, *J. Appl. Phys.* 108 (2010) 124102 <https://doi.org/10.1063/1.3520659>.
- [43] J.F. Li, Z.X. Zhu, F.P. Lai, Thickness-dependent phase transition and piezoelectric response in textured Nb doped Pb(Zr_{0.52}Ti_{0.48})O₃ thin films, *J. Phys. Chem. C* 114 (2010) 17796–17801 <https://doi.org/10.1021/jp106384e>.
- [44] J.J. Zhou, J.F. Li, X.W. Zhang, Orthorhombic to tetragonal phase transition due to stress release in (Li, Ta)-doped (K, Na)NbO₃ lead-free piezoceramics, *J. Eur. Ceram. Soc.* 32 (2012) 267–270 <https://doi.org/10.1016/j.jeurceramsoc.2011.09.001>.
- [45] D. Lin, K.W. Kwok, H.L.W. Chan, Effects of BaO on the structure and electrical properties of the 0.95 K_{0.5}Na_{0.5}(Nb_{0.94}Sb_{0.06})O₃-0.05LiTaO₃ lead-free ceramics, *J. Phys. D Appl. Phys.* 40 (21) (2007) 6778 <https://doi.org/10.1088/0022-3727/40/21/043>.
- [46] P.L. Chen, I.W. Chen, Grain growth in CeO₂: dopant effects, defect mechanism, and solute drag, *J. Am. Ceram. Soc.* 79 (7) (1996) 1793–1800 <https://doi.org/10.1111/j.1151-2916.1996.tb07997.x>.
- [47] M.N. Rahaman, *Ceramic Processing and Sintering*, second ed., Marcel Dekker, Inc., New York, 2003.
- [48] R. Gaur, M. Sangal, A. Dwivedi, K.C. Singh, Lead-free vanadium-substituted (K_{0.485}Na_{0.5}Li_{0.015})(Nb_{0.9}Ta_{0.1})O₃ piezoceramics synthesized from nanopowders, *J. Mater. Sci. Mater. Electron.* 25 (2014) 3195 <https://doi.org/10.1007/s10854-014-2003-2>.
- [49] K.C. Chitra, Singh, Compositional optimization of lead-free (Ba_{1-x}Ca_x)(Ti_{1-y}Sn_y)O₃ ceramics: a structural and electrical perspective, *J. Alloy. Comp.* 765 (2018) 869–877 <https://doi.org/10.1016/j.jallcom.2018.06.273>.
- [50] K. Uchino, S. Nomura, Critical exponents of the dielectric constants in diffused phase-transition crystals, *Ferroelectrics* 44 (1) (1982) 55–61 <https://doi.org/10.1080/00150198208260644>.
- [51] M.A. Mohiddin, K.L. Yadav, Effect of 90° domain on ferroelectric properties of alkali modified SBN, *J. Phys. D Appl. Phys.* 41 (2008) 225406 <https://doi.org/10.1088/0022-3727/41/22/225406>.
- [52] Y. Kumar, M.A. Mohiddin, A. Srivastava, K.L. Yadav, Effect of Ni doping on structural and dielectric properties of BaTiO₃, *Indian J. Eng. Mater. Sci.* 16 (2009) 390–394 <http://hdl.handle.net/123456789/7295>.
- [53] R.Z. Zuo, J. Fu, D.Y. Lu, Y. Liu, Antimony tuned rhombohedral-orthorhombic phase transition and enhanced piezoelectric properties in sodium potassium niobate, *J. Am. Ceram. Soc.* 93 (2010) 2783–2787 <https://doi.org/10.1111/j.1551-2916.2010.03804.x>.
- [54] S. Huo, S. Yuan, Z. Tian, C. Wang, Y. Qiu, Grain size effects on the ferroelectric and piezoelectric properties of Na_{0.5}K_{0.5}NbO₃ ceramics prepared by Pechini method, *J. Am. Ceram. Soc.* 95 (2012) 1383–1387 <https://doi.org/10.1111/j.1551-2916.2011.04992.x>.
- [55] J.S. Liu, S.R. Zhang, H.Z. Zeng, C.T. Yang, Y. Yuan, Coercive field dependence of the grain size of ferroelectric films, *Phys. Rev. B* 72 (2005) 17210 <https://doi.org/10.1103/PhysRevB.72.172101>.
- [56] C. Leu, C.Y. Chen, C.H. Chien, Domain structure study of SrBi₂Ta₂O₉ ferroelectric thin films by scanning capacitance microscopy, *Appl. Phys. Lett.* 82 (2003) 3493–3495 <https://doi.org/10.1063/1.1576308>.
- [57] Y. Tan, J. Zhang, Y. Wu, C. Wang, V. Koval, B. Shi, H. Ye, R. McKinnon, G. Viola, H. Yan, Unfolding grain size effects in barium titanate ferroelectric ceramics, *Sci. Rep.* 5 (2015) 9953 <https://doi.org/10.1038/srep09953>.
- [58] S.C. Abrahams, S.K. Kurtz, P.B. Jamieson, Atomic displacement relationship to Curie temperature and spontaneous polarization in displacive ferroelectrics, *Phys. Rev.* 172 (1968) 551–553 <https://doi.org/10.1103/PhysRev.172.551>.
- [59] Y. Noguchi, H. Shimizu, M. Miyayama, Lattice distortion and ferroelectric properties in Pb-substituted SrBi₂Ta₂O₉, *J. Ceram. Soc. Jpn.* 110 (2002) 999 <https://doi.org/10.2109/jcersj.110.999>.
- [60] B.M. Jin, J. Kim, S.C. Kim, Effect of Grain size on electrical properties of PbZr_{0.52}Ti_{0.48}O₃ ceramics, *Appl. Phys. A* 65 (1997) 53–56 <https://doi.org/10.1007/s003390050>.
- [61] H. Takahashi, Y. Numamoto, J. Tani, K. Matsuta, J. Qiu, S. Tsurekawa, Lead-free barium titanate ceramics with large piezoelectric constant fabricated by microwave sintering, *Jpn. J. Appl. Phys.* 45 (2006) L30–L32 <https://doi.org/10.1143/JJAP.45.L30>.
- [62] C.A. Randall, N. Kim, J.P. Kucera, W. Cao, T.R. Shrout, Intrinsic and extrinsic size effects in fine-grained morphotropic-phase-boundary lead zirconatetitanate ceramics, *J. Am. Ceram. Soc.* 81 (1998) 677–688 <https://doi.org/10.1111/j.1151-2916.1998.tb02389.x>.

To
The Head
Department of Physics and Astrophysics,
University of Delhi, Delhi-110007

15 February 2018

Subject: Dissertation Proposal

Sir,

This is to bring to your kind notice that I am supervising one of the students, Shaoni Kar (INSPIRE Scholar), of BSc (Honours) Physics Third Year in the academic session 2017-18. I am enclosing the proposed dissertation, namely '**To understand and compare various Pseudo-Newtonian potentials in black holes with super-Eddington Accretion rates**'. I am also attaching the names of four probable external examiners for the same.

1. Prof. H. P. Singh, Department of Physics and Astrophysics, University of Delhi
2. Dr. A. P. Singh, Department of Physics, Rajdhani College, University of Delhi
3. Dr. A. K. Jha, Department of Physics, Kironi Mal College, University of Delhi
4. Dr. Pankaj Narang, Department of Physics, ARSD College, University of Delhi

Thanking you,
With kind regards

Dr. A. K. Chaudhary
Associate Professor, Sri Venkateswara College
University of Delhi, Delhi-110021
+91-9654646534
akchaudhary@svc.ac.in

Forwarded by: Dr. B. V. G. Rao, Teacher-in-charge

Topic: To understand and compare various Pseudo-Newtonian potentials in black holes with super-Eddington Accretion rates.

Name of the Student: Shaoni Kar

Supervisor: Dr. A K Chaudhary

Department of Physics, Sri Venkateswara College, University of Delhi

Objective: To compare mathematically and through simulations, the different Pseudo-Newtonian potentials to mimic the general relativity effects around a non-spinning black hole; to attempt to extend it mathematically to the formation of relativistic jets by spinning blackholes.

Introduction: Black holes are the most exotic prediction of Einstein's general relativity and range in mass from a few solar masses to supermassive degrees. They have the strongest possible gravitational fields out of all celestial bodies. The investigation of general relativity in the environment of black holes is one of the fundamentals of current astrophysics research and the main motive behind designing of advanced telescopes.

Accretion is the process where external mass inflows into gravitating objects resulting in angular momentum transport and gradual formation of a stellar disk from the flow around the compact object. This can be visualised to some extent through simulation tools. However, employing the relativity equations implements huge complexity that can be avoided through the use of the different forms of Pseudo-Newtonian potential that limits the error in calculation to less than 10%, even for super-massive blackholes spinning at Super-Eddington accretion rates. This project is an attempt to understand and compare these effects, and extend it to actual general relativity.

Parameters chosen:

- Mass of black hole: $5 \cdot 10^8$ Solar mass
- Accretion Rate: $250 L(\text{edd})/c^2$ to $1500 L(\text{edd})/c^2$
- Self turbulence is generated by the initial magneto-rotational instability.

Project plan:

- Mathematical derivation of pseudo-Newtonian potentials and comparison to General Relativistic conditions; comparative study on type of potential best suited for a blackhole with given parameters.
- Magneto-hydrodynamic simulations of Super-Eddington accretion disks by implementing the various Pseudo-Newtonian potentials and comparative study. Possible conclusion: These accretion rates giving rise to certain values of radiation pressure to gas pressure ratio are only possible in AGN Disks.
- Attempt to mathematically formulate a similar code for actual relativistic conditions for a black hole of the given parameters.

Expected Outcome:

The simulations of the MHD using tools like Matlab are expected to produce graphics that reassert the assumption of the chosen accretion rates being found solely in AGN disks. Apart from this, we also expect to induct actual general relativistic calculations in the simulation to produce a probably more realistic picture.

References:

Jiang, Y.-F., Davis, S. W., & Stone, J. M. 2016b, ApJ, 827, 10 Jiang, Y.-F., Guillochon, J., & Loeb, A. 2016c, ApJ, 830, 125

Jin, C., Done, C., & Ward, M. 2016, MNRAS, 455, 691
—. 2017, MNRAS, 468, 3663

Jiang, Y.-F., Stone, J. M., & Davis, S. W. 2012, ApJS, 199, 14 —. 2013a, ApJ, 778, 65
Stella, L., & Rosner, R. 1984, ApJ, 277, 312

GOVERNMENT OF INDIA
MINISTRY OF SCIENCE & TECHNOLOGY
DEPARTMENT OF SCIENCE & TECHNOLOGY
Technology Bhavan, New Mehrauli Road, New Delhi - 110016



Date: 17/01/2017

Subject: Provisional Offer of INSPIRE Scholarship for students of 2015 Batch

Dear Miss Shaoni Kar,

On the basis of your application submitted under **Scholarship for Higher Education (SHE)** component of the scheme, **Innovation in Science Pursuit for Inspired Research (INSPIRE)**, I am delighted to inform that you have been provisionally selected for the award of INSPIRE Scholarship for the period starting **2015**, which is the year of your enrollment in B.Sc/Int. MSc. or Int. M.S. Course. Your INSPIRE Scholarship Registration Number is **201500054677**.

The final selection for scholarship will be subject to the satisfaction of norms as listed in the **Post Offer Implementation Guidelines**, which is enclosed along with this offer letter.

The total amount of the Scholarship is Rs 80,000/- per annum, out of which Rs 60,000/- as scholarship @ Rs 5000 per month and Rs 20,000/- per year shall be reimbursed for expenses towards summer research internships in research/academic institutions. The maximum tenure of this Scholarship is five years, or until the completion of M.Sc. / Int. M.Sc. /Int. MS course, whichever is earlier, provided you continue to maintain academic excellence and performance. Please note that a student cannot avail more than one scholarship at any time. Further, on acceptance of the INSPIRE scholarship by a student, switching over to other government scholarship schemes including KVPY, is not allowed at any stage without the due permission of the DST.

The Scholarship will be provided directly to you through the **State Bank of India (SBI)** to your bank account. To facilitate the transfer of Scholarship to your bank account, you are requested to **open a normal Savings Bank Account in your name only, at any branch of State Bank of India (SBI) in the country, having no limit of cash transfer (Jandhan, Kiosk, Zero Balance Opening Account or similar type account may please avoided)**. Please note that joint account or account in Banks other than SBI will not be accepted. Upon opening of the Savings Bank account at SBI, you may please fill up the pro-forma available on the online web-portal with the requisite information.

Please note that the submission of the documents such as SBI Bank account details, yearly Performance Reports and Mark Sheets is accepted only through the Online Portal. Please do not send any documents by post. The link to download the Performance Report format is available here www.inspire-dst.gov.in/SHE_Performance_Report.pdf. The validity of this Provisional Offer shall be 120 days from the date of Offer and no documents will be accepted after the prescribed time limit.

For any assistance during online submission of documents, you can write to inspire.prog-dst@nic.in or call 0120-4676260 (Mon-Sat, 10AM to 5PM).

With best regards,

Ms. Tamanna Arora
Scientist 'C'
INSPIRE Programme Division

Miss Shaoni Kar
C/o Goutom Kar
Flat 271, Batukji CGHS, Plot 5B, Sector-3, Dwarka, New Delhi- 110078
West Delhi - 110078 DELHI

This is a computer generated letter, no signature is required

Topic: Role of Synthesis Techniques in the Development of Nanocrystalline CaF₂:Tm Phosphor and its Characterization for Dosimetry of Gamma Rays and Ion Beam.

Student: Ms. JASLEEN KAUR

Supervisor: Dr. ANANT PANDEY

Affiliation: DEPARTMENT OF PHYSICS, SRI VENKATESWARA COLLEGE, UNIVERSITY OF DELHI, DHAULA KUAN, NEW DELHI-110021.

OBJECTIVE: Synthesis techniques play a vital role in thermoluminescence (TL) characteristics of nanophosphors. With deep understanding of TL mechanism, I aim at improving TL characteristics of CaF₂:Tm nanophosphors by using different routes of synthesis and thus developing an indirect dose measuring device for gamma rays and ion beam.

INTRODUCTION: TL is a wide spread phenomenon exhibited by most of minerals, inorganic crystals, glasses and ceramics, organic compounds etc. in which previously absorbed energy from electromagnetic radiation or other ionizing radiation is re-emitted as light upon heating the material [1]. TL is a very good technique which has extended to a whole spectrum of disciplines such as archaeology, forensic sciences, geology, radiation dosimetry, radiation physics, space sciences and many more. Most of the interest in TL comes from the possibility of using it in radiation dosimetry. Radiation is an important tool in nuclear and medical research programs. Since radiation is hazardous, it is necessary to monitor the dose absorbed by the workers who are involved in such programs. Thermoluminescence dosimeter being inexpensive and very sensitive to radiation is one of the many devices used to measure the radiation dose. The main basis in the thermoluminescence dosimetry (TLD) is that TL output is directly proportional to the radiation dose received by the phosphor and hence provides the means of estimating the dose from unknown irradiations. Thus, TL dosimeters are being used in personnel, environmental and medical dosimetry.

Moreover, the importance of nanomaterials has tremendously increased in the field of luminescence as they exhibit enhanced optical, electronic and structural properties, and have potential as efficient phosphors.

Lastly, the most important fact is to find the interrelations among the preparation methods, the structural defects and the TL properties of the material as the structure of the defects can be controlled to a high extent by the preparation method [2].

EXPERIMENTAL PLAN: Nanocrystalline CaF₂:Tm would be prepared by different methods (viz. chemical co-precipitation, combustion etc.). This phosphor would be irradiated with gamma (Co⁶⁰) and ion beam. Physical properties would be checked by X-ray diffraction and other techniques such as TEM/SEM to understand the particle size and the morphology of the samples. Thus, I intend to develop a phosphor that would not only be suitable for dosimetry of electromagnetic radiations like gamma rays but would also work for dosimetry of particulate radiation (ion beam) which are now being commonly used in radiotherapy for cancer treatment.

EXPECTED OUTCOMES: Firstly, I hope to understand the role played by the method of preparation in determining the TL properties of a material. Thereafter, I intend to develop an indirect dose measuring device for gamma rays as well as ion beams. Moreover, the computational skills learnt would be origin, TL reader, powderX, stopping range in matter (SRIM) along with pellet making and ladder making.

REFERENCES:

[1] A.J.J. Bos, Theory of thermoluminescence. *Radiation Measurement* 41(2007) S45-S56.

[2] A. Pandey et.al., *Nuclear Instruments and Methods in Physics Research B* 269 (2011) 216-222.

To
The Head
Department of Physics & Astrophysics
University of Delhi, Delhi-110007

25.01.2019

Sub: List of Names for External Examinership for Dissertation in B.Sc.(H) Physics III Year Examination (2018-2019)

Sir,

I am supervising one student of B.Sc.(H) Physics III Year for her dissertation in the academic session 2018-19. As required I am enclosing her proposed dissertation abstract for your kind approval. Also listed below are the names of four probable external examiners for the viva-voce:

1. Dr. Harsupreet Kaur, Department of Electronics, South Campus, University of Delhi (Phone: 9811905600)
2. Dr. Vijay Sharma, Physics Department, Shyam Lal College, Delhi University (Phone: 9871557925)
3. Dr. Lalit Kumar, Physics Department, Hindu College, Delhi University (Phone: 9911378156)
4. Dr. Raksha Sharma, Physics Department, Kirorimal College, Delhi University (Phone: 9818259896)

The proposed dissertation project is as given below:

Title: ***"Synthesis and characterization of thermoluminescent nanophosphor tricalcium phosphate doped with dysprosium"***

Student: **Ms. Najdeep Kaur** (College Roll Number: 1816038, B.Sc.(H) Physics III Year)

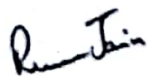
With kind regards,

Yours sincerely,



Dr. Anant Pandey

Assistant Professor of Physics
Sri Venkateswara College
University of Delhi
Dhaura Kuan, New Delhi-110021
Phone: 9811720585
Email: apandey@svc.ac.in



Forwarded by: **Dr. Renu Jain (Teacher-in-Charge)**

DISSERTATION TOPIC: SYNTHESIS AND CHARACTERIZATION OF THERMOLUMINESCENT NANOPHOSPHOR TRICALCIUM PHOSPHATE DOPED WITH DYSPROSIUM

Student name: Ms. Najdeep Kaur (College Roll Number 1816038, B.Sc. (Hons.) Physics III Year Session 2018-19)

Supervisor: Dr. Anant Pandey

Affiliation: DEPARTMENT OF PHYSICS, SRI VENKATESWARA COLLEGE, UNIVERSITY OF DELHI, DHAULA KUAN, NEW DELHI-110021

PURPOSE:

- To synthesize and characterize thermoluminescent nanophosphor tricalcium phosphate doped with dysprosium ($\text{Ca}_3(\text{PO}_4)_2:\text{Dy}$).
- To optimize the phosphor by varying the dopant (dysprosium) concentration in order to establish best possible TL sensitivity in the phosphor.
- To compare the optimized sample with the commercially available standard thermoluminescent dosimeters (TLD).

INTRODUCTION: Luminescence is basically a phenomenon in which some energy source kicks an electron of an atom out of its ground state into an excited state by supplying extra energy to the electron, and then as the excited state is not stable the electron jumps back to its ground state by giving out this energy in the form of light. Now depending on the method of excitation, luminescence can be classified into a number of categories. Thermoluminescence (TL) is one of them in which light is emitted by a semiconductor or an insulator, when it is heated at low temperature after being irradiated by some ionizing radiations such as x-rays, gamma rays etc. TL has a number of applications in a number of fields like radiation dosimetry, age determination of ancient objects, geology etc. [1]. Due to continuous use of different radiations in places like hospitals, nuclear reactors, nuclear research centres, etc it's very important to keep track of radiative exposure levels of individuals to avoid radiation based harmful effects. Since tricalcium phosphate is a nearly tissue-equivalent material (close to being bone-type), it has been reported as a promising TL material prepared by a number of methods like wet precipitation and solid state synthesis [2] and in one of the reports, the same host material is doped with terbium and thulium studied for their TL properties [3]. In the present dissertation project the same host material i.e. tricalcium phosphate but with a different dopant (dysprosium) will be studied. The nanophosphor $\text{Ca}_3(\text{PO}_4)_2:\text{Dy}$ will be prepared by the method of chemical co-precipitation and further irradiated by both UV and gamma rays for TL dosimetry purpose.

EXPERIMENTAL WORK: The experimental work includes the synthesis of the required phosphor $\text{Ca}_3(\text{PO}_4)_2:\text{Dy}$ with varied concentrations of the dopant by the co-precipitation method and, then the characterization of the prepared samples by using various characterization techniques such as X-ray diffraction (XRD), scanning electron microscopy (SEM), photoluminescence (PL), and transmission electron microscopy (TEM). These samples will then be irradiated by gamma and UV rays. After which, the samples will be tested for their TL properties.

EXPECTED DELIVERABLES AND SKILLS LEARNT: It is expected that the prepared optimized phosphor shows high TL sensitivity towards UV, and gamma rays and a linear dose response over a wide range of doses. It is also expected that the phosphor shows low fading over a long period of time. The skills that will be learnt during the project include: working on TL readers and gamma chambers, computational skills to carry out data analysis on application softwares like Origin and powder-X, characterization of samples through XRD, SEM, PL, and TEM.

REFERENCES:

1. S.W.S Mckeever, M. Mosocowitch, P Townsend, *Thermoluminescence dosimetry materials: properties and uses*. Nuclear technology publishing, Ashford (1995).
2. Madhukumar. K., Varma, H.K., Komath, M., Elias, T.S., Padmanabhan, V. and Nair, C.M.K., 2007. Photoluminescence and thermoluminescence properties of tricalcium phosphate phosphors doped with dysprosium and europium. *Bulletin of Materials Science*, 30(5), pp.527-534.
3. Fukuda, Y., Ohtaki, H. and Owaki, S., 1994. Thermoluminescence of thulium sensitized by terbium in β -phase $\text{Ca}_3(\text{PO}_4)_2$. *physica status solidi (a)*, 144(2), pp.K107-K111.



Role of Y^{3+} ion substitution in the enhanced electrical properties of $Ba_{(0.9-x)}Y_xCa_{0.1}Zr_{0.07}Ti_{0.93}O_3$ lead-free piezoceramics

Shreya Mittal¹ · Ishita Chaturvedi¹ · K. Chandramani Singh¹

Received: 11 August 2019 / Accepted: 9 October 2019
© Springer Science+Business Media, LLC, part of Springer Nature 2019

Abstract

$Ba_{(0.9-x)}Y_xCa_{0.1}Zr_{0.07}Ti_{0.93}O_3$ lead free piezoelectric ceramics were synthesized for $x=0-0.035$ in the steps of 0.005. The lead free piezoceramics are gaining importance as there is an urgent demand for replacing the highly toxic PZT family piezoceramics. $Ba_{0.9}Ca_{0.1}Zr_{0.07}Ti_{0.93}O_3$ (BCZT) is one such system. It shows some high electrical properties but suffers with a low Curie temperature, which restricts its usage in low temperature range only. In the present study, the Curie temperature has been improved by 9 °C. A polymorphic phase transition (PPT) has also been observed around $x=0.015$, consisting of orthorhombic and tetragonal phases, which provides the polarization vector more number of favorable directions. As a result the remnant polarization (P_r), piezoelectric charge coefficient (d_{33}) and electromechanical coupling coefficient (k_p) attain their maximum values of 5.21 $\mu C/cm^2$, 200 pC/N and 24.78% respectively for $x=0.015$. This increase in transition temperature and other electrical properties makes BCZT a potential candidate for a lead free piezoelectric system.

1 Introduction

Piezoelectric ceramics have been in use for many years, due to their wide area of applications. These applications include actuators, sensors and transducers. One of the most widely used piezoceramic is lead zirconium titanate ($PbZr_xTi_{1-x}O_3$), abbreviated as PZT, which is a lead based composition. But, lead, being the hazardous substance, must be and has already been banned from almost all of the industries. It is well known that its use can cause serious health issues, including cancer [1]. For many years, the search for a lead-free piezoelectric composition has been going on. But, a suitable candidate has not yet been found; this forced the European countries to implement RoHS 2017 that restricts the use of all hazardous substances except PZT (Lead zirconium titanate) in the electronic industry, to be replaced by a suitable candidate by 2022 [2]. Such exemption calls for the urgent need of finding a lead-free piezoelectric replacement for highly toxic lead-based PZT. In 2009, Liu et al. were able to introduce the world to a lead free composition $x[Ba(Zr_{0.2}Ti_{0.8})O_3] - (1-x)[(Ba_{0.7}Ca_{0.3})TiO_3]$, abbreviated as BZT-BCT, with comparable piezoelectric properties to

the existing prevalent piezoceramic, PZT [3]. Since the discovery of the BZT-BCT composition, a lot of efforts have been made to further improve its electrical properties. Most of these studies include optimizations in the sintering conditions and techniques [4–7], tailoring the initial particle size [8–12] and doping with suitable elements at A-site, B-site or simultaneously both sites [13–17]. But, the major drawback associated with this composition is its low Curie temperature, which restricts its usage in low temperature range only.

In one of our previous studies, we synthesized $Ba_{0.9}Ca_{0.1}Zr_{0.07}Ti_{0.93}O_3 - xY$ ($x=0, 0.02, 0.04, 0.06, 0.08, 0.1$) ceramics in which yttrium was freely doped to enter any of the possible sites [18]. We observed that yttrium enters A-site with Ba^{2+} vacancies for $x=0.02$ only and after that it enters B-site with Ti^{4+} vacancies for $x=0.04$ to $x=0.1$. Also, we observed that A-site substitution of yttrium resulted in elevated Curie temperature with improved electrical properties. The increase in Curie temperature was the highlight of the previous study as the low Curie temperature is the major drawback of BCZT compositions. The enhanced results were attributed to the multi-phase coexistence region in A-site substitution of Y^{3+} .

The present study is to see the effect of A-site substitution, with change in the concentration of Y^{3+} , on the transition temperature and electrical properties of BCZT composition. For this, we synthesized and investigated $Ba_{(0.9-x)}Y_xCa_{0.1}Zr_{0.07}Ti_{0.93}O_3$ ($x=0, 0.005, 0.01, 0.015, 0.02,$

✉ K. Chandramani Singh
kongbam@gmail.com

¹ Department of Physics, Sri Venkateswara College,
University of Delhi, New Delhi 110021, India

0.025, 0.03, 0.035) ceramics for their electrical properties. All the microstructural information and studies of electrical properties of the synthesized ceramics are reported in this paper.

2 Materials and methods

Raw materials of BaCO₃ (99.9%), CaCO₃ (99.9%), ZrO₂ (99.8%), TiO₂ (99.8%) and Y₂O₃ (99.5%) were weighed in their stoichiometric ratios according to Ba_(0.9-x)Y_xCa_{0.1}Zr_{0.07}Ti_{0.93}O₃ ($x=0, 0.005, 0.01, 0.015, 0.02, 0.025, 0.03, 0.035$) composition. The mixture was milled in a ball mill with isopropanol as the milling medium, along with the zirconia balls, for 24 h. The mixed powder was then calcined at 1100 °C for 4 h. Then PVA (Polyvinyl alcohol, 4 wt%) was mixed with the calcined powder to serve as a binder and with the help of a hydraulic press, green pellets of 10 mm diameter and 1 mm thickness were made. The pressure applied was 320 MPa. The pellets were kept at 600 °C for 1 h to burn off PVA. After this the pellets were continued to be heated to 1450 °C, where they were kept for 4 h for sintering to yield the desired ceramics (abbreviated as BCZYT). The heating rate was kept at 5 °C min⁻¹. For electrical measurements, The silver paste was coated on both the plane surfaces of the sintered ceramics which served as electrodes. The densities of all the sintered ceramics were measured using Archimedes Principle: $\rho_{\text{obs}} = w_a / (w_a - w_{\text{water}})$, where, ρ_{obs} = observed density of the ceramic sample, w_a = weight of the sample in air, and w_{water} = weight of the sample in water. The theoretical density of the ceramics is given by the relation: $\rho_{\text{th}} = ZM/N_A V$, where, Z = number of formula units per unit cell, M = molar mass of the composition, N_A = Avogadro's number and V = unit cell volume calculated using XRD. X-ray Diffractometer (BRUKER D8 DISCOVER) was used to analyze the crystalline phases of the ceramics. The temperature and frequency dependences of the dielectric constant were examined using Precision Impedance Analyzer (WAYNE KERR 6500B). The SEM images of the polished and thermally etched surfaces were taken using ZEISS scanning electron microscope. These SEM images were used to study the surface morphology of the ceramics. P–E hysteresis loops of all the ceramics were recorded using P–E loop tracer system (MARINE INDIA). Poling of the ceramics was performed using a Poling unit (Stanford Research Systems PS350) at an electric field of 2.5 kV/mm for 30 min. The piezoelectric charge coefficient (d_{33}) was measured using Piezo d33 m (YE2730A d33 METER). The electromechanical coupling coefficient (k_p) was

calculated using a Precision Impedance Analyzer (WAYNE KERR 6500B) following resonance and anti-resonance data based on IEEE standards:

$$k_p^2 = 2.51(f_a - f_r)/f_r,$$

where, f_r is the resonant frequency, and f_a is the anti-resonant frequency.

3 Results and discussion

3.1 Density

In the present study, we were able to achieve the density as high as 97.9% of the theoretical density in the ceramic sample for $x=0.015$. Above this concentration, the density shows a gradually decreasing trend to a minimum value of 92.43% of the theoretical density. All the observed and calculated values of the densities are tabulated in Table 1.

3.2 XRD studies

Figure 1 shows the XRD patterns of the BCZYT ceramics taken at room temperature in the range of $2\theta = 20\text{--}80^\circ$. All the diffraction peaks are assigned with the characteristic (hkl) indices, calculated using PowderX software [19–21].

All the prepared ceramics are found to exhibit perovskite structure without any secondary phases. As seen in Table 2, the cell volume shows a systematic change with

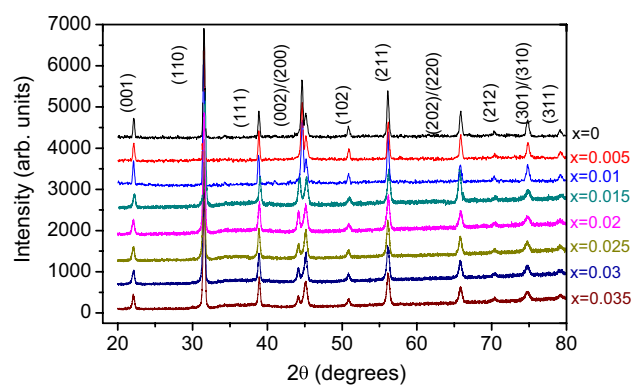


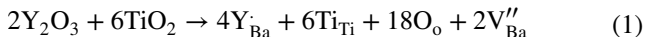
Fig. 1 XRD patterns of Ba_(0.9-x)Y_xCa_{0.1}Zr_{0.07}Ti_{0.93}O₃ ceramics taken at room temperature

Table 1 Observed density, theoretical density and relative density of Ba_(0.9-x)Y_xCa_{0.1}Zr_{0.07}Ti_{0.93}O₃ piezoceramics

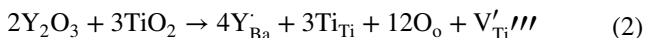
	0	0.005	0.010	0.015	0.020	0.025	0.030	0.035
Observed density (g/cm ³)	5.47	5.54	5.63	5.70	5.60	5.53	5.44	5.35
Theoretical density (g/cm ³)	5.81	5.82	5.83	5.82	5.81	5.80	5.79	5.78
Relative density (g/cm ³)	94	95	96	98	96	95	94	92

the increasing concentration of yttrium in the ceramics with a minimum value of 64.39 Å³ occurring at $x = 0.015$. This observed behavior can be understood on the basis of charge compensation reactions, written using Kröger-Vink notations.

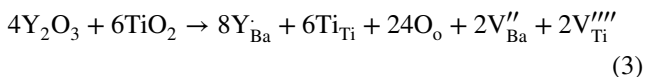
When the Y-ion is doped at Ba-site, the extra charge can be compensated by the barium vacancy:



or, by titanium vacancy:



or, by both, barium and titanium vacancies:



The ionic radii of Y³⁺, Ti⁴⁺ and Ba²⁺ are 1.075 Å, 0.605 Å and 1.61 Å respectively [22]. So, the decreasing trend in the cell volume from $x = 0$ to $x = 0.015$ indicates that the incorporation of yttrium into the lattice takes place by following the reaction Eq. 1. However, the increase in cell volume from $x = 0.015$ to $x = 0.035$ indicates that cation with the lower ionic radius is leaving the lattice, which in the present case is Ti⁴⁺. But, as the observed cell volume remains smaller than that of the un-doped one, it can be interpreted that from $x = 0.02$ to $x = 0.035$ the reactions are governed by the reaction Eq. 3, in which both the cationic vacancies are generated with the barium vacancies proportionately becoming lesser in number than that in the earlier case. Similar results have been reported on BaTiO₃ [23].

The XRD patterns also reveal that from $x = 0$ to $x = 0.01$, the ceramics are in orthorhombic phase with the clear splitting of the peak around $2\theta \sim 45^\circ$, with $I_{002}/I_{200} > 1$, where, I_{002} and I_{200} are the peak intensities for (002) and (200) miller planes' reflections. On the other hand, the ceramics from $x = 0.02$ to

$x = 0.035$ are purely in tetragonal phases with $I_{002}/I_{200} < 1$. The ferroelectrics structures were confirmed with the help of Powder X software. The ceramic with $x = 0.015$ is in a mixed phase indicative of the polymorphic phase transition (PPT) comprising of orthorhombic and tetragonal phases, with $I_{002}/I_{200} \sim 1$. This multi phase coexistence can lead to some high electrical properties as the polarization vector gets many favorable directions. Also, as seen in Table 2, the tetragonality (c/a) from $x = 0.015$ to $x = 0.035$ decreases as the x increases, converging to nearly cubic structure.

The tolerance factors calculated for all the compositions are tabulated in Table 2. The calculations were performed using the modified formula for tolerance factor [24]:

$$t = \left((0.9 - x)R_{Ba}^{2+} + xR_y^{3+} + 0.1R_{Ca}^{2+} + R_o \right) / \left(\sqrt{2} (0.07R_{Zr}^{4+} + 0.93R_{Ti}^{4+} + R_o) \right)$$

where, $x = 0-0.035$, t = tolerance factor, R_{Ba}^{2+} = ionic radius of Ba²⁺, R_y^{3+} = ionic radius of Y³⁺, R_{Ca}^{2+} = ionic radius of Ca²⁺, R_o = ionic radius of O²⁻, R_{Zr}^{4+} = ionic radius of Zr⁴⁺, R_{Ti}^{4+} = ionic radius of Ti⁴⁺. For a stable perovskite structure the tolerance factor lies in the range $0.95 < t < 1.06$, where t denotes the tolerance factor. All the calculated values lie within this range confirming the stability of the perovskite structure [24]. Also, we get a decreasing trend in the value of the tolerance factor with increase in the dopant concentration. It implies the transition from a lower symmetrical structure to the higher symmetrical one, which is also evident from the XRD patterns of the ceramics.

The crystallite size (L) was also calculated for all the ceramics using Scherrer formula [25]:

$$L = k\lambda / \beta \cos \theta,$$

where, $k = 0.9$ (shape factor), λ = wavelength used (Cu-K_α), θ = angle of the highest intensity reflection and β is the

Table 2 Structural and electrical properties of Ba_(0.9-x)Y_xCa_{0.1}Zr_{0.07}Ti_{0.93}O₃ piezoceramics

	0	0.005	0.010	0.015	0.020	0.025	0.030	0.035
Average grain size (μm)	2.45	1.63	1.54	1.51	1.99	2.53	3.26	3.45
Crystallite size (Å)	261	285	286	300	265	260	245	219
Tetragonality (c/a)	–	–	–	–	1.0004	1.0002	1.0001	1.00001
Cell volume (Å ³)	64.59	64.48	64.40	64.39	64.42	64.46	64.47	64.48
Tolerance factor	1.048	1.047	1.046	1.045	1.044	1.043	1.042	1.041
Curie temperature (°C)	83	87	88	92	88	86	84	82
P_r (μC/cm ²)	4.08	3.78	4.42	5.21	5.12	4.98	4.96	4.88
P_s (μC/cm ²)	8.89	8.94	9.07	9.14	8.47	8.35	7.73	7.68
E_c (kV/cm)	2.01	2.04	2.25	2.91	3.38	3.5	3.93	4.47
R_{sq}	0.89	0.95	0.70	0.76	0.78	0.79	0.81	0.82
d_{33} (pC/N)	132	145	164	200	138	98	95	86
k_p (%)	17.42	17.43	17.52	24.78	17.52	17.42	17.42	17.25

P_r remnant polarization, P_s spontaneous polarization, E_c coercive field, R_{sq} squareness of P–E loop, d_{33} piezoelectric charge coefficient, k_p electromechanical coupling coefficient

corrected FWHM (Full width at half maximum), calculated using:

$$\beta^2 = \beta_o^2 - \beta_i^2,$$

where, β_o is the observed FWHM and β_i is the broadening due to the instrument. As seen in Table 2, as the yttrium content increases the crystallite size increases to a maximum value of 300 Å for the composition with $x=0.015$. For $x > 0.015$, the crystallite size decreases continuously. With the decrease in the crystallite size the dipole moment per unit volume tends to decrease, which can affect the overall polarization of the ceramics.

3.3 SEM studies

Figure 2a–h show the SEM micrographs of the polished and thermally etched surfaces of all the yttrium doped $\text{Ba}_{(0.9-x)}\text{Y}_x\text{Ca}_{0.1}\text{Ti}_{0.93}\text{Zr}_{0.07}\text{O}_3$ ceramics.

All the ceramics are densely packed and appear to possess multimodal grain size distribution. With increase in yttrium content the smaller grains tend to gradually disappear and bigger grains increase in number. This increase in larger grains at the expense of the smaller grains can be attributed to the difference in the chemical potential of the surfaces. Figure 3a–h shows the grain size distribution in the ceramics, calculated using the line intercept method in ImageJ software [26].

It is clear from the histograms that initially there are small as well as large grains in the ceramics, but with the increasing presence of yttrium in the ceramics the grain size distribution spreads with the growth of bigger grains at the cost of smaller grains. The average grain size (Fig. 3e) shows a fall from $x=0$ to $x=0.015$, after which it increases to the larger values.

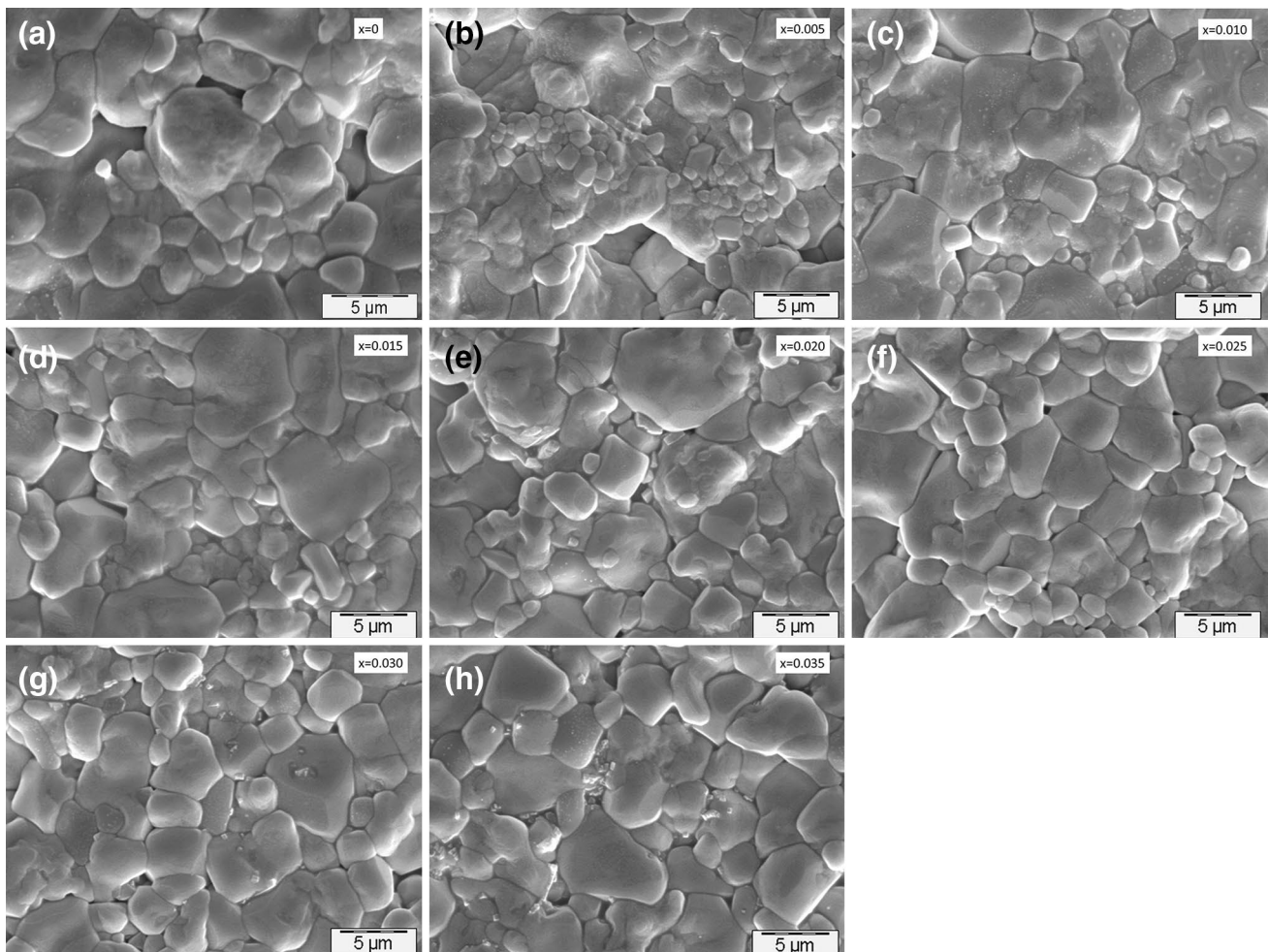


Fig. 2 SEM images of polished and thermally etched surfaces of $\text{Ba}_{(0.9-x)}\text{Y}_x\text{Ca}_{0.1}\text{Ti}_{0.93}\text{Zr}_{0.07}\text{O}_3$ ceramics with **a** $x=0$, **b** $x=0.005$, **c** $x=0.010$, **d** $x=0.015$, **e** $x=0.020$, **f** $x=0.025$, **g** $x=0.030$ and **h** $x=0.035$

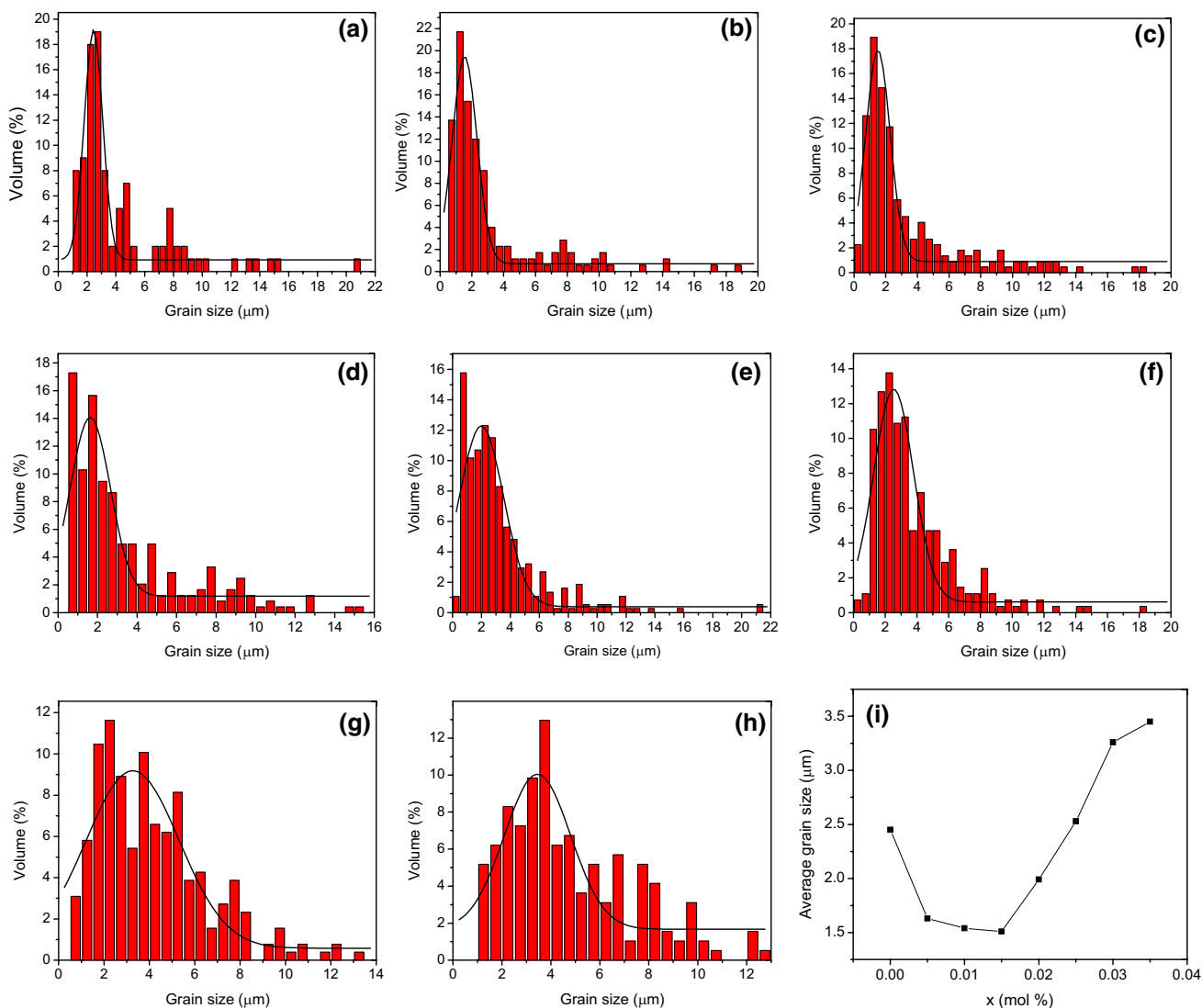


Fig. 3 Grain size distribution of the grains in the $\text{Ba}_{(0.9-x)}\text{Y}_x\text{Ca}_{0.1}\text{Zr}_{0.07}\text{Ti}_{0.93}\text{O}_3$ ceramics with **a** $x=0$, **b** $x=0.005$, **c** $x=0.010$, **d** $x=0.015$, **e** $x=0.020$, **f** $x=0.025$, **g** $x=0.030$ and **h** $x=0.035$; **i** Variation in average grain size with change in x

3.4 Dielectric studies

Figure 4a, b shows the temperature dependence of the dielectric constant measured at 1 kHz.

All the ceramics show a global maximum at the Curie temperature (T_c), which is the indication of the phase transition from ferroelectric phase to paraelectric phase. For the first four compositions, i.e. from $x=0$ to $x=0.015$, another hump, below T_c , has also been observed (Fig. 4b). This hump signifies the transition from a ferroelectric phase to another ferroelectric phase. As the temperature increases, the ceramic undergoes the symmetry transformation, generally from lower symmetry to the higher one. In the present case, this is a transition from orthorhombic structure to a structure of higher symmetry, i.e. tetragonal

and the corresponding temperature is labeled as T_{o-t} . Figure 4d shows the variation in T_{o-t} with the change in x .

The T_{o-t} for the un-doped one was found to be 52 °C. It decreases with the increase in x and reaches to around room temperature for $x=0.015$. With further increase in x , the T_{o-t} goes below the room temperature and hence could not be observed, whereas, T_c increases as the amount of yttrium increases to $x=0.015$, which is of great importance in view of BCZT composition. It decreases with further increase in x . The variation in T_c can be explained with the help of the concept of bond-dissociation energy. The values for bond dissociation energy of Ba–O, Y–O and Ti–O are 563 kJ/mol, 715 kJ/mol and 662 kJ/mol [27]. As discussed in XRD section, from $x=0$ to $x=0.015$, yttrium enters A-site with only A-site ion vacancies. The Y–O bond is stronger than

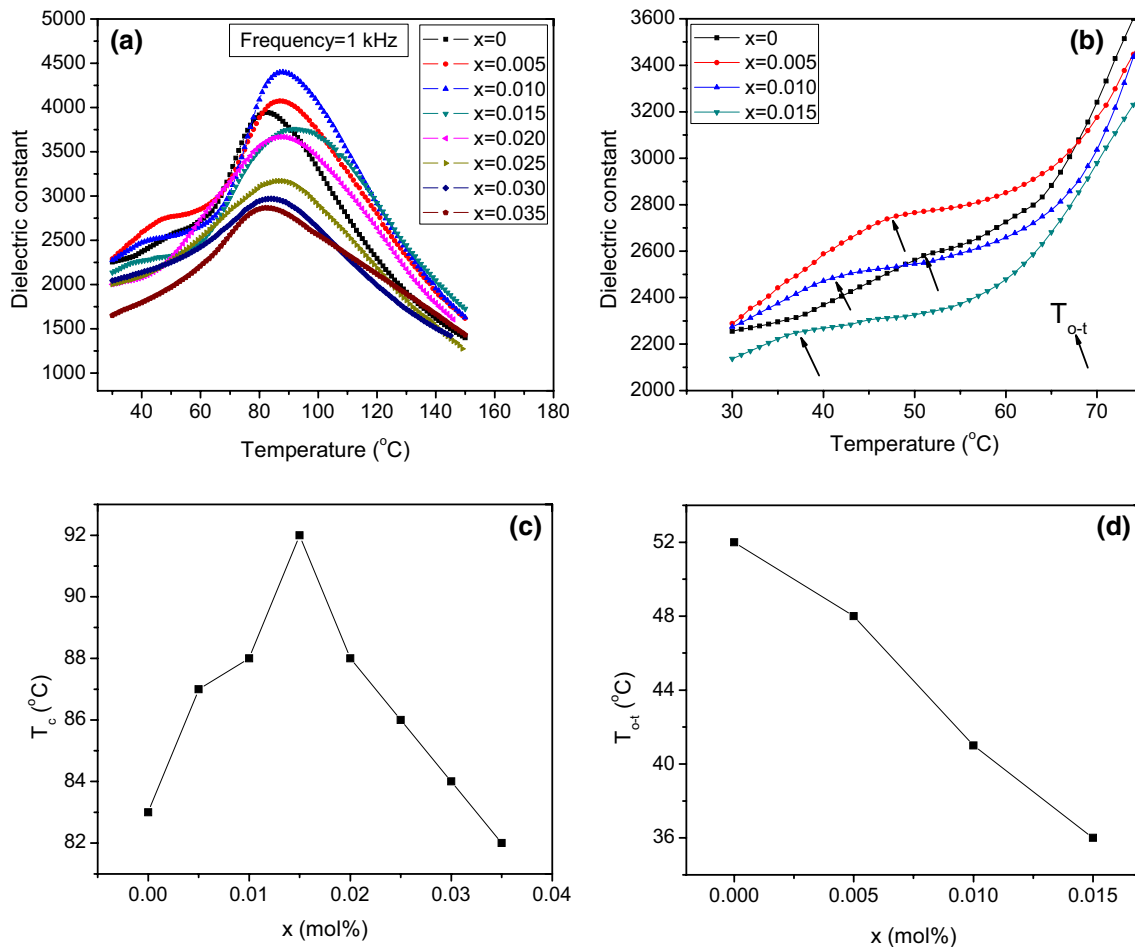


Fig. 4 **a** Temperature dependence of dielectric constant for different concentrations of yttrium at 1 kHz; **b** Magnified image of dielectric constant versus temperature curve to show T_{0-t} in $x=0$ to $x=0.015$; **c** Change in transition temperature T_c and **d** T_{0-t} with x

Ba–O bond and hence the Ba–O bonds get disturbed, in turn strengthening the Ti–O bonds. This strengthening of Ti–O bond increases the transition temperature. However, from $x=0.02$ to $x=0.035$, it has been seen that yttrium enters A-site with the creation of A-site ion and B-site ion vacancies simultaneously. These Ti^{4+} (B-site ion) vacancies weaken the Ti–O bonds and hence decrease the transition temperature.

The temperature dependence of dielectric constant was also observed at three different frequencies i.e. at 1 kHz, 10 kHz and 100 kHz (Fig. 5a–h).

It was noticed that with the increase in the frequency, the dielectric constant at room temperature decreases and the transition temperature shifts to the higher temperature. Also, the transitions are found to be diffused. These are the two characteristics of a relaxor ferroelectric and hence it is concluded that all the ferroelectric ceramics, in the discussion, are relaxor ferroelectrics [28]. The relaxor behavior is due to the formation of polar nano regions or polar nano domains that are active below as well as beyond the Curie

temperature. These are the small ordered regions disturbing the long range order of the system.

The diffusivities were also calculated for such transitions (Fig. 6).

The diffusivity is found to rise initially reaching the maximum value of 2 at $x=0.015$, after which it decreases. Relating with the XRD results, it is clear that diffusivity increases with the increasing presence of A-site vacancies only, but it decreases when the generation of B-site vacancies is prevalent. It is thus suggestive that the diffusivity is directly proportional to the number of A-site vacancies in yttrium doped $\text{Ba}_{0.9}\text{Ca}_{0.1}\text{Zr}_{0.07}\text{Ti}_{0.93}\text{O}_3$ ceramic system.

3.5 Ferroelectric studies

Figure 7a shows the P–E hysteresis curves of all the ceramics, recorded at room temperature and at 50 Hz. All the loops are well saturated hence showing the behavior of a ferroelectric. Figure 7b shows the variation in remnant polarization and coercive field with increasing yttrium content.

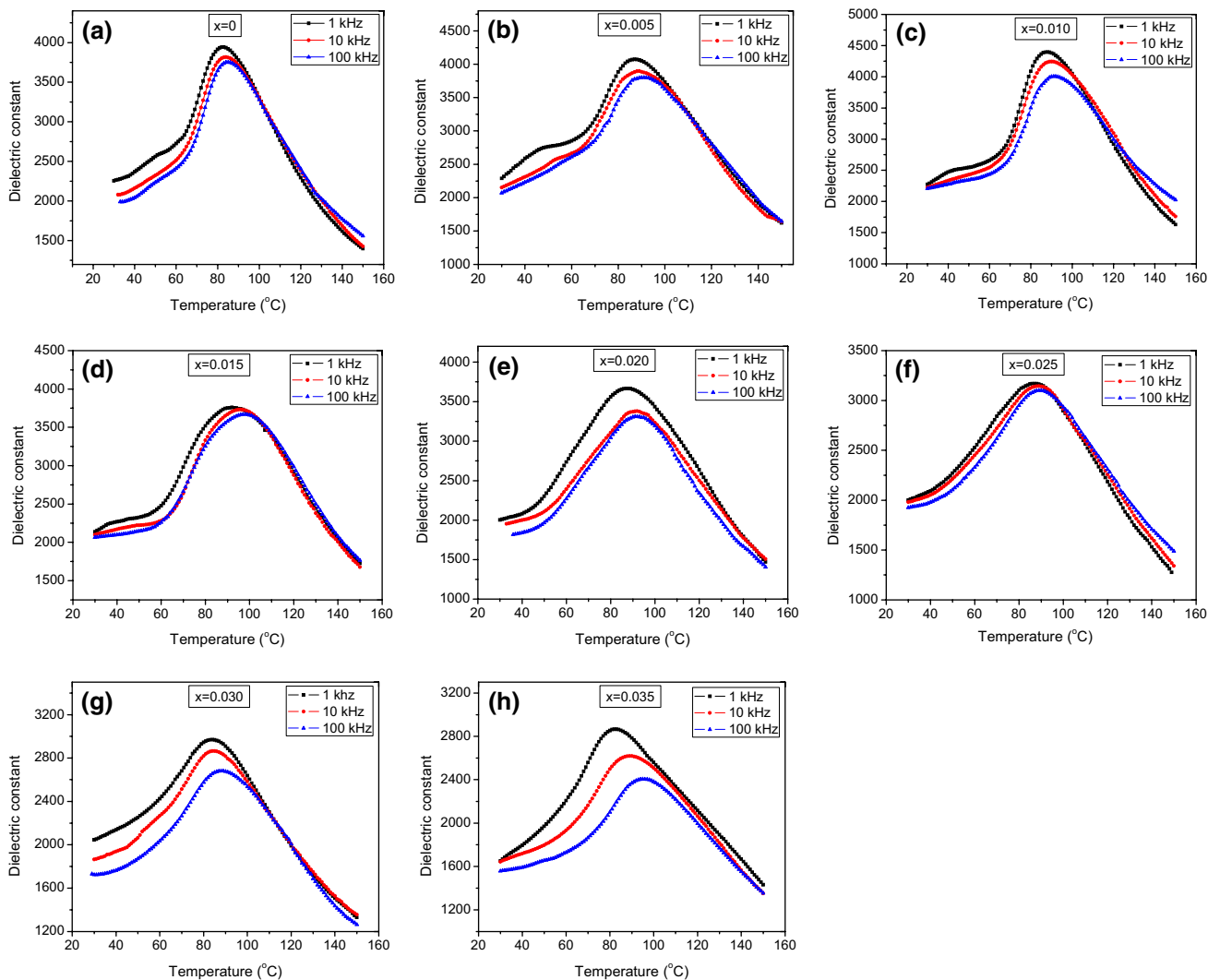


Fig. 5 Temperature dependence of dielectric constant of $Ba_{(0.9-x)}Y_xCa_{0.1}Zr_{0.07}Ti_{0.93}O_3$ ceramics at 1 kHz, 10 kHz and 100 kHz for **a** $x=0$; **b** $x=0.005$; **c** $x=0.010$; **d** $x=0.015$; **e** $x=0.020$; **f** $x=0.025$; **g** $x=0.030$ and **h** $x=0.035$

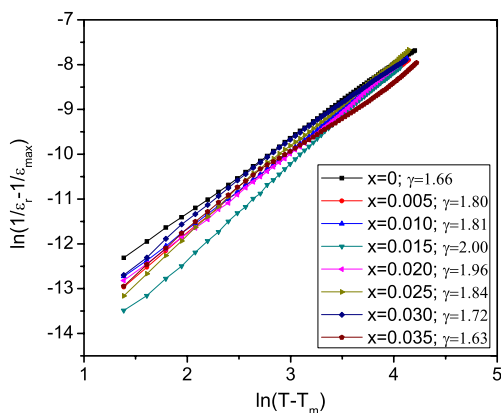


Fig. 6 Diffusivity of all the $Ba_{(0.9-x)}Y_xCa_{0.1}Zr_{0.07}Ti_{0.93}O_3$ ceramics as a slope of $\ln(1/\epsilon_r - 1/\epsilon_r^{max})$ versus $\ln(T - T_m)$ graph

The remnant polarization increases with x and reaches to a maximum value of $5.21 \mu C/cm^2$ for $x=0.015$. The coercive field keeps on increasing with the increase in the yttrium concentration. The increase in remnant polarization with increase in x can be explained on the basis of increased crystallite size. As the crystallite size increases, the distance between the atoms increases and hence individual dipoles increase. This influences the overall polarization of the ceramics. Also, in this range of $x=0$ to 0.015 , it can be noticed that the corresponding average grain size of the ceramics decreases (Table 2). With the decreasing grain size, the grain boundaries increase in number. Along with this the rise in remnant polarization suggests that the contribution towards net polarization comes from the boundaries as well, that corresponds to the space charge or interfacial polarization. The increase in coercive field can be explained on the

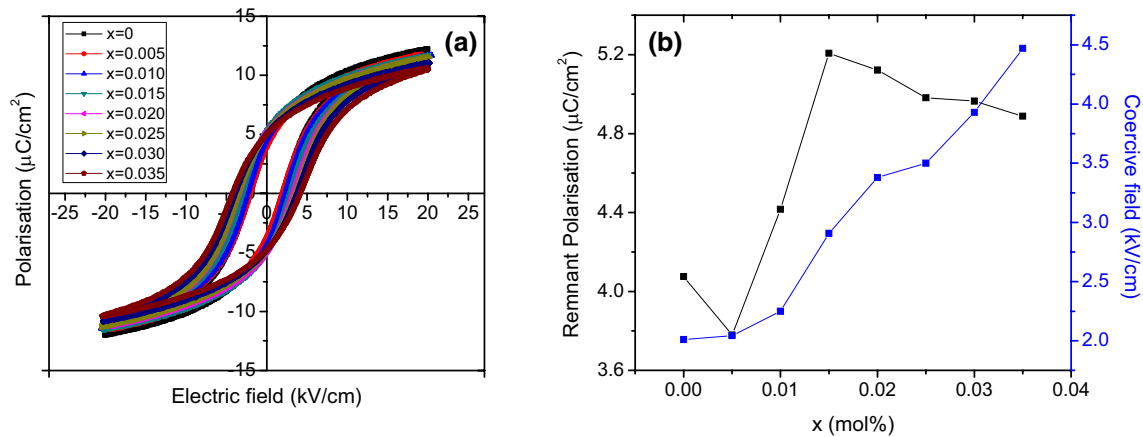


Fig. 7 **a** P–E loops of $\text{Ba}_{(0.9-x)}\text{Y}_x\text{Ca}_{0.1}\text{Zr}_{0.07}\text{Ti}_{0.93}\text{O}_3$ ceramics; **b** variation in remnant polarization and coercive field with increasing yttrium content

basis of charge defects. As sintering was performed at high temperature, oxygen vacancies are expected to occur plus as the yttrium content increases, various stoichiometric defects may also appear. These defects contribute to domain wall pinning effect which in turn makes polarization reversal difficult and hence increase the coercive field of the concerned ferroelectric ceramic.

The observed P–E loops are slimmer than those of a normal ferroelectric, which is due to the relaxor behavior of the ferroelectric ceramics, as discussed earlier. The degree of saturation of the loops can be measured in terms of a parameter called squareness of the loop, R_{sq} , given by:

$$R_{\text{sq}} = P_r/P_s + P_{1.1(\text{Ec})}/P_r,$$

where, P_r = remnant polarization, P_s = spontaneous polarization and $P_{1.1(\text{Ec})}$ = polarization at the electric field of 1.1 times of the coercive field. The values of R_{sq} vary between 0.70 and 0.95 for all the ceramics (Table 2), showing incomplete saturation of the loops, which can again be due to the relaxor behavior of the ceramics.

3.6 Piezoelectric studies

Figure 8 shows the dependence of piezoelectric parameters, piezoelectric charge coefficient (d_{33}) and electro-mechanical coupling coefficient (k_p), on Y^{3+} content in $\text{Ba}_{(0.9-x)}\text{Y}_x\text{Ca}_{0.1}\text{Zr}_{0.07}\text{Ti}_{0.93}\text{O}_3$ ceramics.

Both these parameters attain their maximum values of 200 pC/N and 0.25 respectively at $x=0.015$. Such high values of d_{33} and k_p in this sample can be attributed to the associated high density, high P_s , and high ϵ_r . From the thermodynamic theory, the dependence of d_{33} on P_s and ϵ_r is as follows [29]:

$$d_{33} = 2Q_{11}\epsilon_0\epsilon_r P_s,$$

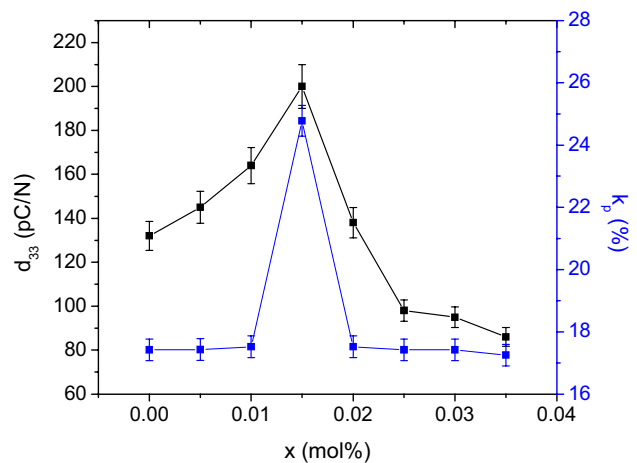


Fig. 8 Piezoelectric charge coefficient and electromechanical coupling coefficient of $\text{Ba}_{(0.9-x)}\text{Y}_x\text{Ca}_{0.1}\text{Zr}_{0.07}\text{Ti}_{0.93}\text{O}_3$ ceramics

where, ϵ_r is the dielectric constant, P_s the spontaneous polarization, and Q_{11} the electrostrictive coefficient which couples longitudinal strain and polarization.

Also, as confirmed from XRD analysis and temperature dependence of dielectric constant, there exists a mixed phase of tetragonal and orthorhombic structure around $x=0.015$, at room temperature. Such a mixed phase provides the maximum favorable orientations for the polarization vector and hence contribute to the high piezoelectric properties at $x=0.015$. In addition, the large crystallite size is also contributing to the improved piezoelectric properties of the sample. As the crystallite size increases, the individual dipole moments increase which contributes to more polarization. It can also be seen from the SEM images that the grain size decreases to its minimum value at $x=0.015$. It is known that as the grain size decreases, the domain wall

density increases, which is the region where major dynamics happen and is responsible for the high piezoelectric effect. The ceramic with $x=0.015$ being the composition of lowest grain size contains largest domain wall density and hence the appreciable piezoelectric effect. The effect of A-site vacancies can further be highlighted as the major contribution towards the enhanced electrical properties. Only with A-site vacancies, the properties were increased and reached to their respective maxima. It is apparent from the present study that there exists a “cut-off” value for x after which B-site ions also start vacating their lattice site.

4 Conclusion

In this work, $\text{Ba}_{(0.9-x)}\text{Y}_x\text{Ca}_{0.1}\text{Zr}_{0.07}\text{Ti}_{0.93}\text{O}_3$ ($x=0, 0.005, 0.01, 0.015, 0.02, 0.025, 0.03, 0.035$) ceramic compositions have been made and investigated for their microstructural and electrical properties. All the ceramics show dense microstructure. There can also be seen a gradual transformation from orthorhombic phase to tetragonal phase as we increase $x=0.015$ to 0.02 , which confirms the presence of polymorphic phase transition (PPT) around $x=0.015$. Plus, it has been seen that yttrium ion can substitute for A-site in the BCZT composition provided its concentration is optimally chosen. The increase in various electrical properties has been observed. The dielectric, ferroelectric and piezoelectric properties improved for 0.015 mol% of yttrium content. This increase in the electrical properties can majorly be attributed to the occurrence of PPT around $x=0.015$. Also, the increase in T_c by 9°C is a finding of a great importance here. This study emphasizes on the dependence of electrical properties and transition temperature on the amount of yttrium ion concentration and the site it occupies in the perovskite structure. The study conclusively reveals that this A-site doped BCZT composition can further be optimized to get the desired results.

Acknowledgements The authors acknowledge the directors, solid state physics laboratory and AIIMS, Delhi for providing facilities for some measurements.

Funding The authors acknowledge the Department of Science and Technology of India (Research Project No.: EMR/2014/284) and Council of Scientific and Industrial Research (CSIR), Government of India (SRF), for financial support.

References

1. E.U. Directive, 2011/65/EU. Off. J. Eur. Union **50**, 88 (2011)
2. Directive (EU), 2017/2102. Off. J. Eur. Union L **305**, 8 (2017)
3. W. Liu, X. Ren, Phys. Rev. Lett. **103**, 257602 (2009)
4. P.Y. Jiang, X.G. Tang, S.G. Ju, Q.X. Liu, T.F. Zhang, H.F. Xiong, J. Mater. Sci. **27**(3), 3048 (2016)
5. Y. Cui, X. Liu, M. Jiang, X. Zhao, X. Shan, W. Li, C. Yuan, C. Zhou, Ceram. Int. **38**(6), 4761 (2012)
6. X. Chen, X. Ruan, K. Zhao, X. He, J. Zeng, Y. Li, L. Zheng, C.H. Park, G. Li, J. Alloys Compd. **632**, 103 (2015)
7. W. Liu, S. Li, I.E.E.E. Trans, Dielectr. Electr. Insul. **22**(2), 734 (2015)
8. A.K. Nath, C. Jiten, K.C. Singh, Phys. B **405**(1), 430 (2010)
9. S. Hunpratub, T. Yamwong, S. Srilomsak, S. Maensiri, P. Chindaprasirt, Ceram. Int. **40**(1), 1209 (2014)
10. A. Jain, A.K. Panwar, A.K. Jha, Ceram. Int. **42**(16), 18771 (2016)
11. Y. Bai, A. Matousek, P. Tofel, V. Bijalwan, B. Nan, H. Hughes, T.W. Button, J. Eur. Ceram. Soc. **35**(13), 3445 (2015)
12. A.V. Polotai, A.V. Ragulya, C.A. Randall, Ferroelectrics **288**(1), 93 (2003)
13. H. Lu, L. Liu, J. Lin, W. Yang, L. Weng, X. Zhang, Ceram. Int. **44**(6), 6514 (2018)
14. Y. Tian, S. Li, S. Sun, Y. Gong, T. Li, Y. Yu, Q. Jing, J. Electron. Mater. **47**(1), 684 (2018)
15. D. Zhang, Y. Zhang, S. Yang, J. Mater. Sci. **26**(2), 909 (2015)
16. A. Hamza, F. Benabdallah, I. Kallel, L. Seveyrat, L. Lebrun, H. Khemakhem, J. Alloys Compd. **735**, 2523 (2018)
17. X. Wang, P. Liang, L. Wei, X. Chao, Z. Yang, J. Mater. Sci. **27**(4), 3217 (2016)
18. S. Mittal, R. Laishram, K.C. Singh, Ceram. Int. **45**, 1237 (2019)
19. C. Dong, J. Appl. Crystallogr. **32**, 838 (1999)
20. P.-E. Werner, Z. Krist. **120**, 375 (1964)
21. P.-E. Werner, L. Eriksson, M. Westdahl, J. Appl. Cryst. **18**, 367 (1985)
22. R.D. Shannon, Acta Crystallogr. A **32**, 751 (1976)
23. J. Zhi, A. Chen, Y. Zhi, P.M. Vilarinho, J.L. Baptista, J. Amer. Ceram. Soc. **82**(5), 1345 (1999)
24. L.A. Xue, Y. Chen, R.J. Brook, Mater. Sci. Eng. B **1**(2), 193 (1988)
25. P. Scherrer, Göttinger Nachrichten Gesell. **2**, 98 (1918)
26. C.A. Schneider, W.S. Rasband, K.W. Eliceiri, Nat. Methods **9**(7), 671 (2012)
27. D.R. Lide, *CRC Handbook of Physics and Chemistry*, 88th edn edn. (Taylor and Francis, London, 2007)
28. L.E. Cross, Ferroelectrics **76**, 241 (1987)
29. K. Uchino, S. Nomura, Ferroelectrics **44**(1), 55 (1982)

Publisher's Note Springer Nature remains neutral with regard to jurisdictional claims in published maps and institutional affiliations.



Size-dependent structural and electrical properties of lead-free BCST ceramics prepared from high-energy ball milled nanopowders

Chitra^a, Shriya Agarwal^a, Radhapiyari Laishram^b, K. Chandramani Singh^{a,*}

^a Department of Physics, Sri Venkateswara College, University of Delhi, New Delhi, 110021, India

^b Solid State Physics Laboratory, Lucknow Road, Timarpur, New Delhi, 110054, India

ARTICLE INFO

Keywords:

High-energy milling
Sintering
Microstructure
Piezoelectric properties
Perovskite

ABSTRACT

Recently developed $(\text{Ba}_{0.88}\text{Ca}_{0.12})(\text{Ti}_{0.94}\text{Sn}_{0.06})\text{O}_3$ (BCST) ceramic composition gained popularity as a cleaner substitute for the lead-based $\text{Pb}(\text{Zr,Ti})\text{O}_3$ (PZT) after its electrical properties were found to be comparable to those of some soft-end PZTs. These properties can be further enhanced by optimizing the microstructure and phase-symmetry of the ceramic system. In the present work, BCST nanopowders have been synthesized via solid-state reaction method followed by high-energy ball milling. Initial particle size has been controlled by varying the milling speed from 100–400 rpm at fixed milling time. It has been observed that a mere change in initial particle size strongly affects the microstructural, structural and electrical properties. A monotonous decline in average particle size ($\sim 97\%$) with an enormous rise in the average grain size ($\sim 260\%$) with milling speed is observed. The increase of milling speed causes the evolution of perovskite crystal symmetry of the ceramics from orthorhombic to tetragonal, with the bulk density acquiring a peak value for BCST ceramic prepared from 175-rpm milled powder. As a consequence of relatively high density and favorable phase-structure, the piezoelectric properties of this ceramic sample exhibit a significant enhancement of about $\sim 70\%$.

1. Introduction

Piezoelectrics are widely used in actuators, resonators, ultrasonic generators, sensors and similar electronic devices. Currently, PZT is extensively employed in the electronic industry for various piezoelectric applications due to its advanced piezoelectric properties originating from the presence of Morphotropic Phase Boundary (MPB) in the material [1,2]. The MPB makes the domain reorientation in the material easier due to a larger possibility of polarization directions associated with the coexistence of two mixed phases. A vertical MPB in the PZT material gives it an added advantage of having temperature-independent electrical properties. However, there is an urgent need for a cleaner lead-free piezoelectric material due to the concerns caused by the lead (Pb) content in PZT to the environment [3,4]. As a result, some of the lead-free materials like BaTiO_3 (BT), $\text{K}_{1-x}\text{Na}_x\text{NbO}_3$ (KNN), $\text{Bi}_{1/2}\text{Na}_{1/2}\text{TiO}_3$ (BNT), have been studied extensively in the recent times [5]. The pseudo-binary BT system has been considered as a potential candidate. However, the BT systems were found to be much inferior to PZT in terms of their piezoelectric properties [6]. To improve these properties, suitable dopants are used to modify the host composition. The piezoelectric properties of BT systems can be enhanced by shifting the polymorphic phase transition (PPT) closer to room temperature or

by introducing the substance at the phase boundary of the ferroelectric and non-ferroelectric phase. This results in the facilitation of the polarization rotation of dipoles which are under external stress or field. During recent years, many variations of BT have been proposed, which include BNT-BT, $(\text{Ba}_{0.95}\text{Sr}_{0.05})(\text{Zr}_{0.05}\text{Ti}_{0.95})\text{O}_3$ (BSZT), $(\text{Ba}_{1-x}\text{Ca}_x)(\text{Ti}_{1-y}\text{Sn}_y)\text{O}_3$ [5,7–13].

In $\text{Ba}_{1-x}\text{Ca}_x(\text{Ti}_{1-y}\text{Sn}_y)\text{O}_3$ materials, the replacement of A-site (Ba^{2+}) of the BT system by Ca^{2+} shifts the orthorhombic to tetragonal (T_{O-T}) and rhombohedral to orthorhombic (T_{R-O}) phase transition temperatures towards the lower temperature region but it barely affects the Curie temperature (T_c), whereas the replacement of B-site (Ti^{4+}) by Sn^{4+} shifts T_{R-O} and T_{O-T} towards higher temperature region and can significantly lower the T_c [12,13]. Moreover, high piezoelectricity in these systems is attributed to the concurrence of two or more phases which emanates to an unstable polarization state, making it easier for the external electric field to cause polarization rotation. In our previous work, conventional ceramic processing route was employed to produce $(\text{Ba}_{1-x}\text{Ca}_x)(\text{Ti}_{1-y}\text{Sn}_y)\text{O}_3$ ceramics, with x ranging from 0.06 to 0.18 and y from 0.04 to 0.08. It was seen that the ceramic composition ($x = 0.12$ and $y = 0.06$) exhibits the highest directional strain with optimum piezoelectric and ferroelectric properties. This particular ceramic composition proved to be an ideal candidate to be used for various

* Corresponding author.

E-mail address: kcsingh@svc.ac.in (K.C. Singh).

<https://doi.org/10.1016/j.mtcomm.2020.101400>

Received 5 March 2020; Received in revised form 21 June 2020; Accepted 26 June 2020

Available online 08 July 2020

2352-4928/ © 2020 Elsevier Ltd. All rights reserved.

piezoelectric applications owing to a primary pyroelectric coefficient (p_1) of $0.488 \text{ C/m}^2\text{K}$ and hydrostatic electrostrictive coefficient (Q_h) of $0.0414 \text{ m}^4/\text{C}^2$. Apart from this, a high value for dielectric constant, low dielectric loss along with maximum spontaneous polarization was observed. The improved electric properties including dielectric, ferroelectric, pyroelectric and piezoelectric properties are traced to the complimentary contribution from BCT and BST terminals [14].

Nanoscience plays an integral part in today's world due to the fact that the properties exhibited by these particles greatly differ from those shown by their bulk counterparts. Reports have shown enhanced properties including mechanical, electrical or optical properties in nanomaterials [15,16]. This can be explained by understanding the nanoscale effects which become relevant at this scale, such as the "quantum size effect" wherein the electrical properties are altered with the reduction in the particle size in the given size range. BCST has been chosen for the present study in view of improving its properties further. This study owes allegiance to various reports on improvement in the electrical as well as physical properties of the BT ceramic samples prepared with nanoparticles [17,18]. It has been found that the particle size of BT strongly affects its dielectric constant [19]. Moreover, below a certain critical particle size, the lattice structure converts from disordered tetragonal symmetry to ordered cubic symmetry resulting in the disappearance of ferroelectricity [20,21]. The average critical particle size for BT below which it loses its ferroelectric nature is reported to be below 50 nm [22]. The present work is an attempt to comprehensively analyze the ramification of the change in particle size on the electrical properties of BCST system. Even though there have been reports of a similar study for simpler-structure ceramics like alkaline niobate, BT systems, etc., such a study on complex system like BCST composite system has not been reported so far.

Though nanoparticles can be obtained via various techniques like hydrothermal synthesis, sol-gel technique or the chemical co-precipitation method [23–25], we have opted for the high energy ball milling (HEBM), being the most extensively used technique for synthesizing nanopowders due to its simplicity and cost effectiveness in terms of large scale production [26,27]. The HEBM is proven to be more effective than the conventional milling method due to its ability to bring about a possible chemical change in the sample in contrast to the inability of the latter. The aforementioned change can be further exploited for the creation of the required perovskite structure by solid state reaction, merely by ball milling, hence eliminating the calcination process altogether [28,29]. Furthermore, the Coriolis and frictional forces produced in HEBM result in a more enhanced degree of particle size reduction than its counterparts.

2. Materials and method

Raw powders of AR grade CaCO_3 (99.5 %), SnO_2 (99.0 %), BaCO_3 (99.0 %) and TiO_2 (99.5 %) were stoichiometrically weighed to yield $(\text{Ba}_{0.88}\text{Ca}_{0.12})(\text{Ti}_{0.94}\text{Sn}_{0.06})\text{O}_3$ ceramics. These contents were properly mixed in plastic bottles containing zirconia's balls and isopropanol for 20 h in an ordinary ball mill. The mixture obtained was dried at 70°C in an oven over 24 h which was then crushed using agate mortar and pestle. The powder mixture was then calcinated at 1150°C in air for 4 h in order to obtain the required perovskite structure. A Retsch PM 100 planetary ball mill was used to high energy ball mill this calcined powder to achieve the highest degree of fineness. The ball mill contains an eccentrically arranged grinding jar on the sun wheel which moves opposite to the direction of the grinding jar while maintaining the ratio of both speeds at 1: -2. Balls and vials made of agate are used for the process. The grinding balls are subjected to Coriolis force resulting from the superimposed rotational movements. High dynamic energies are released from the interaction involving frictional and impact forces between the balls and the grinding jar and are responsible for the effective particle size reduction in the ball mill. 5 g of the prepared powder was taken for each study with the weight ratio of the calcined

sample to the milling balls fixed at 1:5. This was then ball milled at various milling speeds: 0 rpm, 100 rpm, 175 rpm, 250 rpm, 325 rpm and 400 rpm for a fixed milling time of 5 h. The ball-milled powder was then pressed into disks of 10 mm diameter and 1 mm thickness with a hydraulic press producing a 320 Mpa uniaxial pressure. These pellets were further sintered at 1450°C in air for 4 h with a constant heating rate of $5^\circ\text{C}/\text{min}$ starting from 40°C . The samples so obtained were accordingly named as BCST0, BCST100, BCST175, BCST250, BCST325 and BCST400.

TEM (FEI Morgagni 268 TEM) data was employed to study the size of the particles of the milled powder samples. The crystalline structure of the ceramics was analysed using the X-Ray diffractometer (Bruker D8 Discover) data obtained with $\text{Cu-K}\alpha$ radiation ($\lambda = 1.5406 \text{ \AA}$) for 2θ ranging from 20° to 80° with the step interval of 0.04° . FESEM micrographs of thermally etched ceramic surfaces were gathered using FESEM (Zeiss Gemini SEM 500) after measuring the bulk densities for various ceramic samples through Archimedes' principle: $\rho_{\text{obs}} = w_a / (w_a - w_{\text{water}})$, where ρ_{obs} = observed density of the ceramic sample, w_a = weight of the sample in air and w_{water} = weight of the sample in water. Meanwhile, the theoretical density for the samples was estimated using the formula: $\rho_{\text{th}} = ZM/N_A V$, where Z = number of formula units per unit cell, M = molar mass of the composition, N_A = Avogadro's number and V = Unit cell volume calculated from XRD analysis. All the electrical measurements were made after silver coating the pellet on both sides, with the silver acting as electrodes for the sample. The coated samples were fired at 130°C for 30 min. The variation of dielectric properties with temperature and frequency was measured at the testing voltage fixed at 1 V, through an impedance analyzer (Wayne Kerr 6500B, Germany). Further, the PE loop tracer system (Marine India) was used to detect the ferroelectric properties at a frequency of 50 Hz. A dc electric field as high as $3 \text{ kV}/\text{mm}$ was used to pole the ceramic samples, keeping the temperature fixed at 60°C to measure the piezoelectric charge coefficient (d_{33}) using a Piezometer (Take Control PM 25). Resonance and anti-resonance method was employed to estimate the planar electromechanical coupling coefficient (k_p) using the data obtained from the impedance analyser [30].

3. Results and discussion

3.1. TEM analysis

TEM images for the powders produced under various milling conditions are depicted in Fig. 1. Fig. 2 shows the dependence of particle size on the milling speed as determined from Fig. 1. The average particle size can be seen to gradually reduce from 275 nm for the unmilled powder to 115 nm for 175-rpm and finally to 7 nm for the 400-rpm sample.

The energy provided during milling via the high-energy planetary ball mill is used to produce nanoscale particles. This energy ruptures the interatomic crystal bonds and forms additional surfaces resulting from the cleavage of crystalline grains [31]. An analytical model, given by Gusev et al. describes the relationship between post-milling particle size (D) of the ceramic sample and the milling energy (E_{mill}) with the equation [32]:

$$D = \frac{M[A + B \ln(D_{\text{in}}/2b)\epsilon_{\text{max}}\{1 - \exp(ct)\}]}{E_{\text{mill}} + M[A + B \ln(D_{\text{in}}/2b)\epsilon_{\text{max}}\{1 - \exp(ct)\}]/D_{\text{in}}} \quad (1)$$

where D_{in} is the initial particle size for the ceramic samples, M is the initial mass, A and B are constants which are characteristic of the particular material, $\epsilon = \epsilon_{\text{max}}[1 - \exp(ct)]$ ($c < 0$) is an empirical function describing the variation of the micro-strains ϵ with the milling time t and b is the Burgers vector magnitude linked with the disordered network of grains edge dislocations.

The milling energy, E_{mill} which is used up in milling of the powder is found to be proportional to ω^3 (the cube of the angular rotation speed) and the milling time t . Hence, it can also be expressed as:

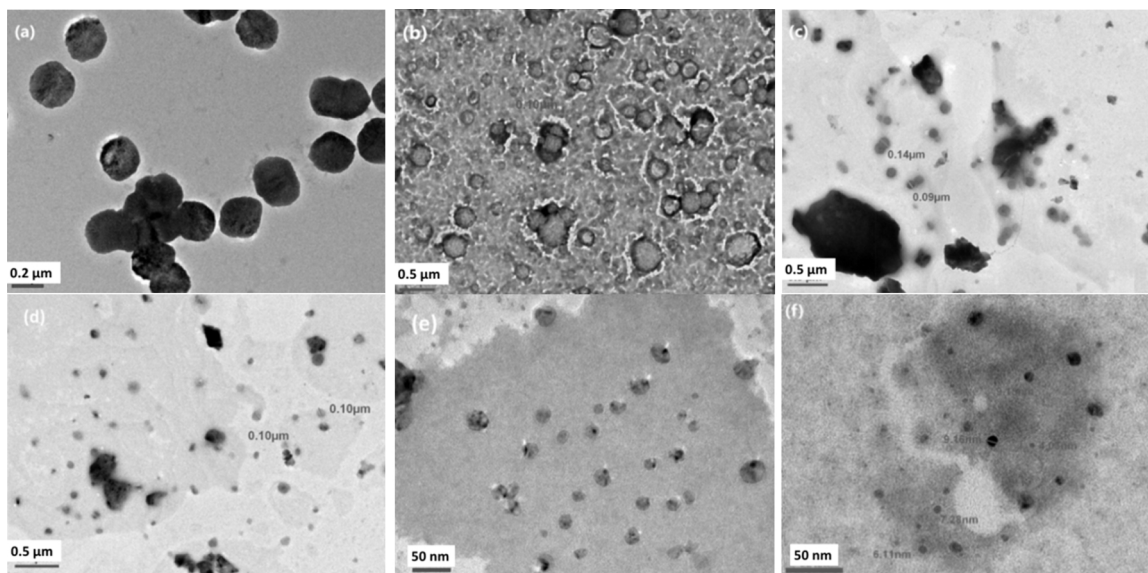


Fig. 1. TEM images for BCST nanoparticles milled for 5 h. at (a) 0 rpm, (b) 100 rpm, (c) 175 rpm, (d) 250 rpm, (e) 325 rpm and (f) 400 rpm.

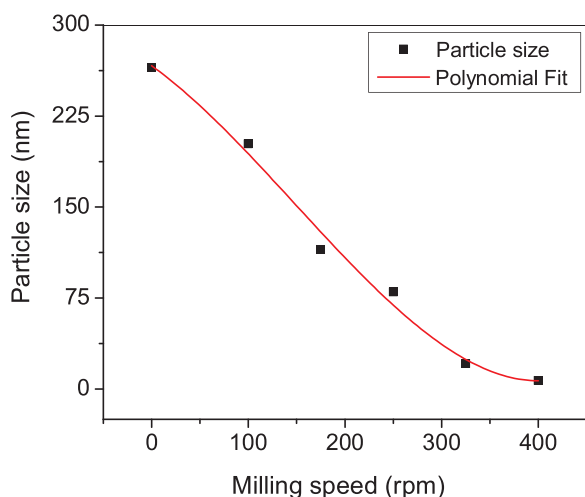


Fig. 2. Plot showing change in particle size with a change in milling speed.

$$E_{mill} = \kappa \omega^3 t, \quad (2)$$

where κ is a constant factor for the milling system. Combining both the equations given above, we obtain:

$$D = \frac{M[A + B \ln(D_{in}/2b)\epsilon_{max}\{1 - \exp(ct)\}]}{\kappa \omega^3 t + M[A + B \ln(D_{in}/2b)\epsilon_{max}\{1 - \exp(ct)\}]/D_{in}} \quad (3)$$

In the above equation, we see that the average particle size post milling is inversely proportional to ω^3 as can also be observed from the fitted polynomial curve which gives the adjusted R squared value of 0.98 suggesting a good fit (Fig. 2). Therefore, the observed gradual reduction of the particle size with a rise in the rotation speed is in accordance with this model.

3.2. Structural analysis

Fig. 3a depicts the X-ray diffraction pattern for BCST ceramics, milled at different milling speeds. XRD data was studied and indexed with the TREOR90 program using Powder X software [33]. The XRD peak patterns obtained for BCST0, BCST325 and BCST400 are found to be in agreement with the JCPDS file no. 05-0626 for the tetragonal (T) symmetry, whereas JCPDS file no. 79-1482 for orthogonal (O)

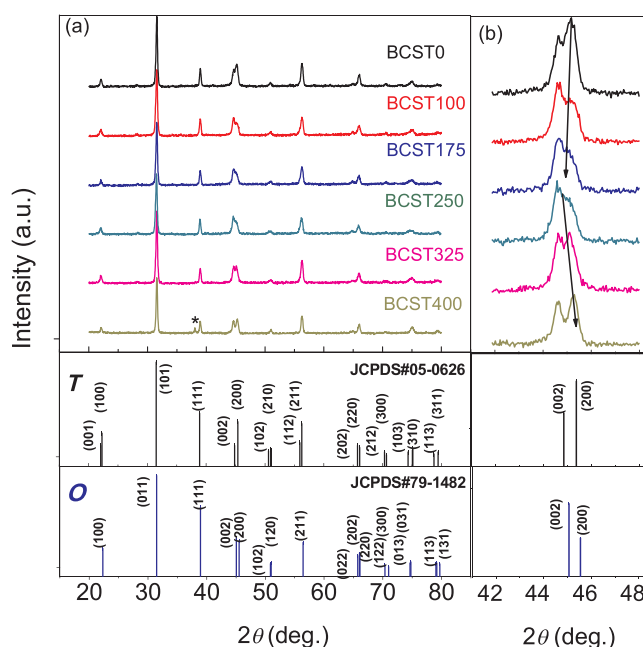


Fig. 3. (a) X-ray diffraction patterns for BCST ceramics prepared from powders milled at different milling speeds and (b) magnified image of the XRD peaks around 45°.

symmetry matches well for BCST100, BCST175 and BCST250 ceramic samples.

It is seen in Fig. 3a that the perovskite structure is exhibited by all the BCST ceramic samples, without the presence of any secondary phase, with an exception of a secondary peak seen in the diffraction pattern of BCST400 sample at $2\theta = 38.16^\circ$. The existence of a secondary phase for BCST400 sample demonstrates that the working sintering temperature (1450 °C) is practically too high for this system. A similar effect of high sintering temperature on the phase structure and the composition of the compound has also been observed in $\text{Li}_{7-x}\text{La}_3\text{Zr}_2\text{O}_{12-0.5x}$ and $\text{Na}_{0.5}\text{K}_{0.5}\text{NbO}_3$ ceramics [34,35]. As a general understanding, reduction in initial particle size promotes sinterability and thus decreases the sintering temperature for complete phase formation with dense microstructure [36]. Therefore, we expect a lower sintering temperature for the BCST400 sample with very fine initial

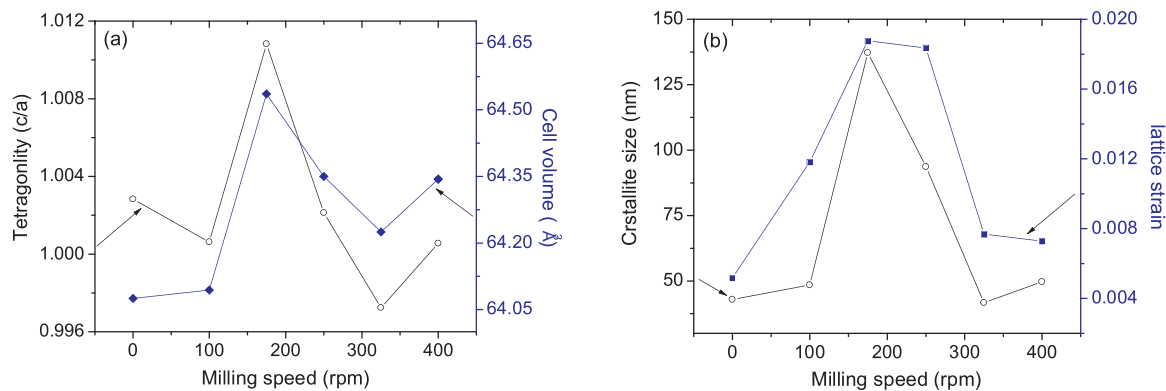


Fig. 4. (a) Variations of tetragonality (c/a) and unit cell volume, and (b) Plots showing the variation of lattice strain and crystallite size, of BCST ceramics on milling speed.

particle size (~ 7 nm, Fig. 1f). Additionally, porous surface morphology has also been observed for BCST400 sample (Fig. 5f) indicative of inappropriately high sintering temperature for this particular milling speed, similar to the inference drawn from the XRD analysis. Fig. 3b shows the magnified image of the XRD peaks present around 45° . It clearly shows that BCST0 sample crystallizes into the tetragonal phase with $P4mm$ symmetry characterized by the higher intensity (200) peak, (I_{200}) and lower intensity (002) peak, (I_{002}). As we increase milling speed up to BCST250, the intensity pattern of the 45° peak changes with more intense I_{002} peak than I_{200} peak [12,37], suggesting a phase shift to orthogonal $Amm2$ symmetry. On increasing the milling speed further to 325-rpm, the intensity, I_{200} can be seen re-emerging with higher intensity count than I_{002} to finally depict a clearly defined tetragonal symmetry for BCST400 sample.

The variation in unit cell volume (V) and tetragonality (c/a) for BCST system against milling speed are plotted in Fig. 4a. The plot depicting the variation of crystallite size and lattice strain of BCST ceramics with milling speed is shown in Fig. 4b. The average lattice strain and crystallite size present in the ceramic samples are calculated by fitting the graph for $\beta\cos\theta$ versus $\sin\theta$, using the Williamson-Hall method [38,39] which is given by:

$$\beta\cos\theta = \frac{k\lambda}{L} + \eta\sin\theta \quad (4)$$

where β is the peak profile's FWHM, λ is the wavelength for X-ray used and θ is the diffraction angle. Fig. 4b illustrates the dependence of lattice strain (η) and crystallite size (L) on the milling speed.

Table 1 shows the crystallographic properties of the samples, including crystallite size, cell parameters, lattice strain and unit cell volume of the BCST ceramics. As seen from Table 1, the cell parameters a and b increase throughout, with a standard deviation in the range 0.0003–0.0007 whereas c is seen to peak for the milling speed of 175-rpm and falls on either side. These variations result in the tetragonality and the cell volume peaking at 175-rpm as observed in Fig. 4(a). The alterations in lattice parameters are also in agreement with the shifting of diffraction peaks (Fig. 3b) upon milling. The diffraction peaks can be seen to gradually shift towards smaller angles, signifying a rise in the lattice cell volume till BCST175, after which the peak is seen to move towards larger angles implying a decline in cell volume at higher speeds.

From Fig. 4b, the crystallite size apexes at ~ 137 nm for the 175-rpm sample before finally decreasing to ~ 50 nm for the 400-rpm sample. It can also be noted that the lattice strain shows a maximum value of 0.0188 for BCST175 and finally falls to a value of 0.0073 for BCST400. It has been reported by various researchers that the systems with high strain values have a higher tetragonality [40,41]. The present observation that both these parameters show the highest values at BCST175 (Table 1), agrees with such reports.

The significant structural changes leading to changing crystal symmetries of BCST ceramic system are induced by the milling conditions. It is a well-accepted fact that evolution of the domain structure (formation of 90° and 180° domain structure) always accompanies the phase transition of the ferroelectric system in order to reduce the strain induced by its electric and elastic energy [22,42,43]. Whether the system undergoes the creation of domains or surface charge/polarization gradients inside the crystal to minimize these strains depends on the crystallite/particle size [22]. Furthermore, a thermodynamic theory reported for the BT systems also states that there is an alteration in the crystal structure from symmetric cubic to asymmetric tetragonal phase for a crystallite size greater than 80 nm [22]. This transformation accompanied by the domain twinning is an attempt to reduce the increased internal stress within the crystallite arrangement due to clamping condition imposed by its neighboring crystallites. However, smaller particles/crystallites with low internal stress may not undergo lattice deformation since they are free from clamping. In view of these considerations, as milling speed rises from 0 to 250-rpm, the BCST system with lattice strain greater than 0.01 (Table 1) is more likely to transform into a more asymmetric orthorhombic phase to lessen this strain by the development of ferroelectric multi-domains. Whereas, on further increasing the milling speed such as in BCST325 and BCST400 systems having small crystallites with less strain, exhibit no crystal transformation and are mostly stable in tetragonal phase below curie temperature T_c .

3.3. Surface morphology and density measurement

Fig. 5 (a–f) shows the FESEM micrographs of polished and thermally etched surfaces of BCST0, BCST100, BCST175, BCST250, BCST325 and BCST400 ceramic system respectively. Average grain size for each sample is estimated using the slope-intercept method via the Image J software. Besides, the histograms plotted in the insets in Fig. 5(a–f) show the distribution of grain size against its number count. As seen in the figure, BCST0 consists of evenly spread small-sized grains while the bigger grains tend to evolve in size along with the shrinkage of smaller ones with a further rise in the milling speed. A significant effect of changing milling speed on the microstructure packing and the porosity can also be observed in Fig. 5. Further, the microstructure tends to be more homogenous and dense with a reduction in the porosity up to BCST175. However, on further increasing the milling speed, the difference between the sizes of bigger and smaller grains gradually becomes even more significant with escalating porosity in the sample.

Changing surface morphology and microstructure of BCST ceramics as a result of varying milling speed also affects the density of the ceramics. In order to analyze this effect, Archimedes' principle is used to calculate the bulk density for each sample showing no deliquescence on exposure to water for 24 h. Further, the relative density for all the

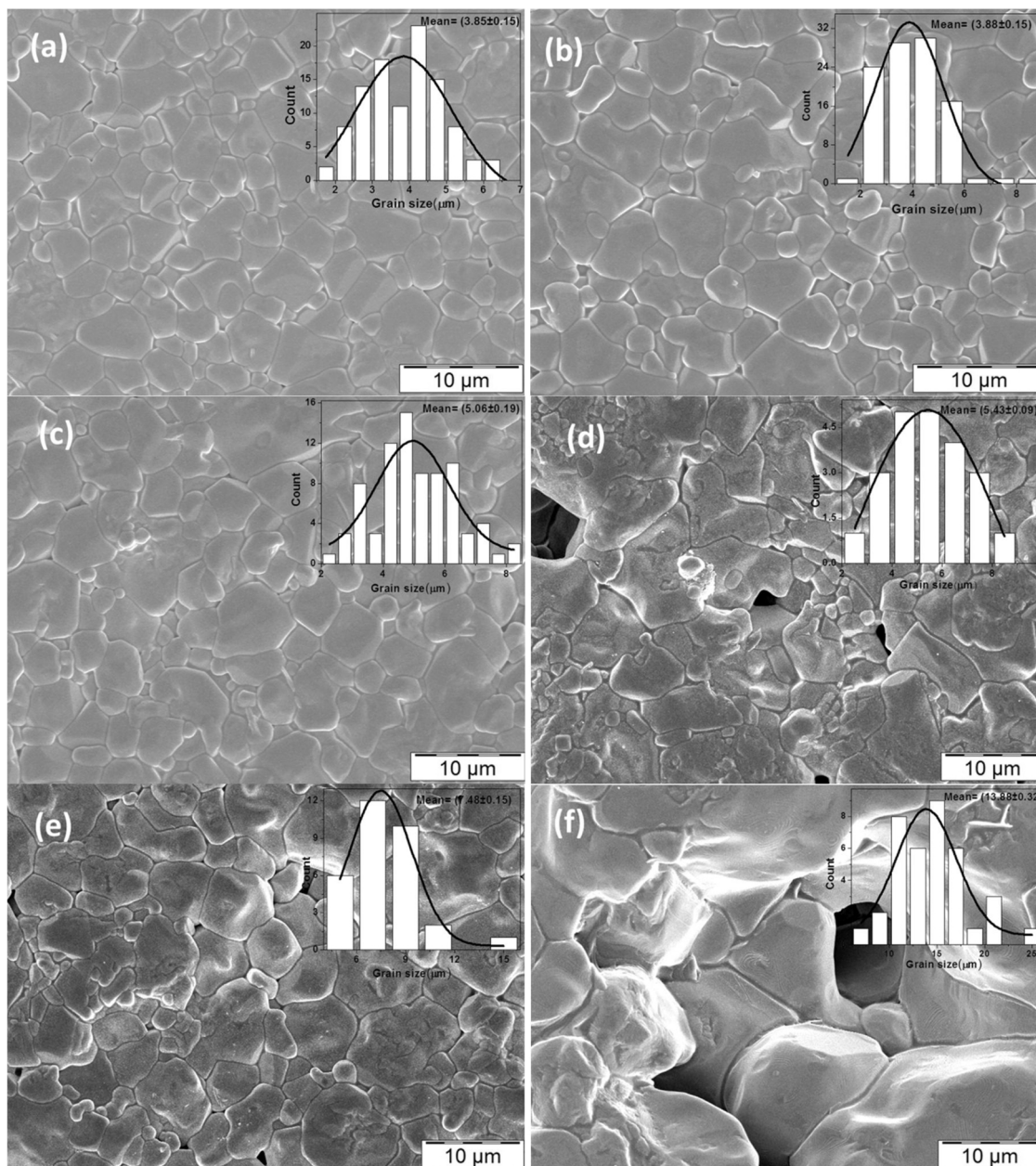


Fig. 5. FESEM micrographs of polished and thermally etched surfaces of (a) BCST0, (b) BCST100, (c) BCST175, (d) BCST250, (e) BCST325 and (f) BCST400 ceramic system.

ceramics is also determined using the theoretical density, which is calculated with the help of its molecular weight along with the cell volume, as derived from the XRD analysis. The variations in bulk density, relative density and the porosity with milling speed are summarized in Table 2. Moreover, Fig. 6 depicts the relation of grain size

and relative density of the sample with milling speed. It should be noted that while the grain size shows an increasing trend starting from 3.85 μm for BCST0 to 13.88 μm for BCST400, the relative density is seen to increase and peak at 175 rpm (93.16 % of TD) before decreasing rapidly for BCST400 at 78.7 % of its TD.

Table 1
Size dependent crystallographic properties of BCST ceramics.

Milling Speed (rpm)	Crystallite size (nm)	Strain	Lattice parameters (\AA)			Tetragonality (c/a)	Cell volume (\AA^3)
			a	b	c		
0	42.9	0.0052	3.9978	3.9978	4.0091	1.0028	64.07
100	48.47	0.0118	4.0003	4.0009	4.0028	1.0006	64.09
175	137.27	0.0188	4.0044	4.0117	4.0477	1.0108	64.54
250	93.68	0.0183	4.0036	4.006	4.0121	1.0021	64.35
325	41.76	0.0077	4.0121	4.0121	4.0009	0.9972	64.23
400	49.69	0.0073	4.0057	4.0057	4.0079	1.0005	64.34

Table 2
Measured properties of $(\text{Ba}_{0.88}\text{Ca}_{0.12})(\text{Ti}_{0.94}\text{Sn}_{0.06})$ ceramics milled for various milling speed.

Milling Speed (rpm)	0	100	175	250	325	400
Bulk Density (g/cm^3)	5.35	5.34	5.41	5.33	5.24	4.59
Theoretical density (g/cm^3)	5.76	5.79	5.8	5.82	5.79	5.78
Relative Density (%)	91.45	91.35	93.16	91.46	89.7	78.7
Porosity (%)	8.55	8.65	6.85	8.54	10.3	21.3
ϵ_{rt} , 30 °C	2431	2350	2483	2248	1998	1500
Dielectric loss, 30 °C	0.0157	0.0172	0.0185	0.0187	0.0179	0.0225
Curie temperature, T_c (°C)	79	80	72	70	74	77
ϵ_m at T_c	3894	3715	4221	4698	4228	3003
Curie constant, C ($\times 10^{50}\text{C}$)	0.876	0.798	0.796	0.743	0.704	0.559

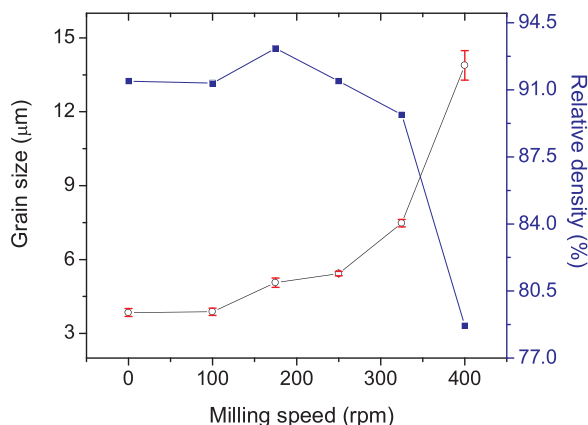


Fig. 6. Plots of average relative density and grain size of BCST ceramics as a function of milling speed.

It is commonly understood that the reduction of the excess surface energy is the macroscopic driving force for sintering, which can occur either through the elimination of solid interfaces leading to densification or through the reduction in the surface area by increasing the average grain size and thus causing coarsening of the sample [36,44]. For milling speeds from 0 to 175-rpm, the finer particles produced activate the atomic diffusion process rate, promoting densification. These diffusion processes increase the transportation of matter from the interior of the grains to the pores, leading to grain growth along with the pore shrinkage. Both these simultaneous effects lead to the densification of the sample as observed in Fig. 5(a–c). However, on further increasing the milling speed above 175-rpm, we see that while the average grain size increases, the inter-granular spacing widens with rising porosity resulting in coarsening of the samples (Fig. 5d–f). This may be attributed to the formation of agglomerates originated from the activation of electrostatic and other surface forces in very fine particles having increased surface/volume ratio [36]. Coarsening of the microstructure occurs upon heating of these agglomerates as they tend to sinter together as partially sintered agglomerates with large pores between them. As coarsening prevails over densification at higher milling speeds, an extremely porous microstructure is anticipated to form as also observed in BCST400 (Fig. 5f) ceramic sample due to the disappearance of driving forces for densification.

3.4. Dielectric studies

Fig. 7 depicts the change in dielectric constant (ϵ_{rt}) measured at room temperature with frequency for BCST0, BCST100, BCST175, BCST250, BCST325 and BCST400 ceramic samples. It is clearly visible that the dielectric constant (ϵ_{rt}) tends to fall with a rise in the frequency,

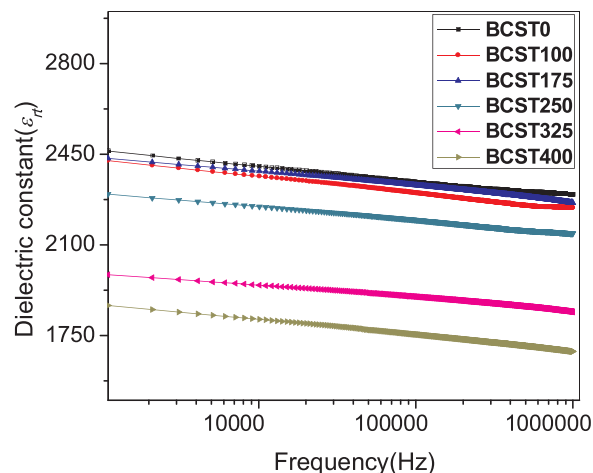


Fig. 7. (a) Frequency variation of dielectric constant (ϵ_{rt}) measured at room temperature for BCST ceramics milled at various milling speeds.

with an increasing rate towards higher frequencies. It is also worth observing that the ϵ_{rt} values for the BCST0, BCST100 and BCST175 remain very close to each other, whereas there is a significant drop in the value for dielectric constant with the rise in the milling speed thereafter. This declining trend with increasing milling speed is also in accordance with the degrading density of the samples (Table 2). The observed high values of dielectric constant for BCST0, BCST100 and BCST175 are attributed to the homogeneity and high density of its microstructure. A similar dependence of ϵ_{rt} on the density of the sample has also been observed in many other such systems [14,45]

The dependence of the dielectric loss ($\tan\delta$) and dielectric constant (ϵ) on temperature, measured at 10 kHz are illustrated in Fig. 8. The measured electrical properties for each sample have been provided in Table 2. It can be observed that ϵ_{rt} at 30 °C slightly increases to 2483 for BCST175 and then rapidly declines on further increasing the milling speed (1500 for 400 rpm); similar to the observations made from Fig. 7. The maximum dielectric constant (ϵ_m) at T_c is found to be the highest (4698) for BCST250 before showing a declining trend. The receding dielectric constant value for BCST175 is a consequence of the dominant role played by increased average grain size (Table 2) in determining the dielectric behavior of the material. As grain size rises, high insulating regions i.e. grain boundary regions with higher values for capacitance linked with them, decrease in proportion as compared to the low resistive grain bulk regions thereby decreasing dielectric properties [46].

On the other hand, the dielectric loss at 30 °C is seen to maximize at the value of 0.0225 for 400-rpm sample (Fig. 8b). This trend for the dielectric loss is in accordance with the porosity of the sample, which also shows the same trend. When BCST400 sample is sintered at high enough temperature, the highly porous microstructure is obtained (Fig. 5f) which is considered as crystal imperfections enhancing extrinsic losses in ceramic systems. These imperfections increase the number of conduction paths for free mobile electrons contributing to conductive losses, hence decreasing the value for dielectric constant. Subsequently, Fig. 8a shows a single peak for the ϵ - T plot for each sample corresponding to T_c or the Curie temperature which is the transition temperature for ferroelectric to paraelectric phase. The effect on T_c as a result of reducing particle size is systematic but confined within a narrow range. T_c is seen to decrease to 70 °C for BCST250 from 79 °C for BCST0 and then increases for higher speeds.

The Curie constant, C is calculated for various BCST ceramics beyond the transition temperature T_c , using Curie-Weiss law, which is given by [47]:

$$1/\epsilon = \chi = C/(T - T_c) \quad (5)$$

where χ is the inverse of dielectric permittivity (electrical

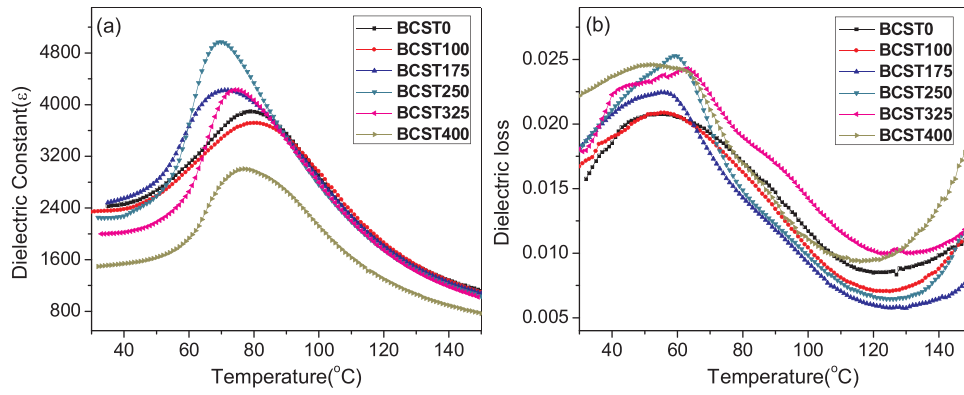


Fig. 8. Plots showing (a) variation of dielectric constant (ϵ) with temperature, and (b) dielectric loss measured for BCST ceramics milled at various milling speeds.

susceptibility) and T is the temperature. The values of parameter C recorded in Table 2 show a systematic decrease from 0.876×10^5 °C for the sample under no milling effect i.e. BCST0 to 0.559×10^5 °C for BCST400 sample.

Further, it can also be noted that the broadening of the dielectric peaks around T_c changes with variation in the milling speed. This is owed to the varying character of the phase transition diffusivity. The degree of diffusivity for the system is calculated using the formula given by Uchino and Nomura as [48]:

$$1/\epsilon - 1/\epsilon_m = (T - T_c)^\gamma / C, \quad (T > T_c) \quad (6)$$

where C is a constant and γ is the degree of diffusiveness of the phase transition at T_c and ranges between 1 and 2. It equals to 1 for a completely structured transition of a system whereas a value of 2 suggests an entirely diffused transition phase.

Fig. 9 shows the plot between $\ln(1/\epsilon - 1/\epsilon_m)$ versus $\ln(T - T_c)$ for various samples. As per the equation given above, we expect to get a straight line for this plot with γ as the slope. The value for γ obtained for each sample exhibits a systematic change with decreasing particle size. As seen in Fig. 9, γ gradually decreases from 1.82 to 1.66 for BCST250 and then increases to 1.74 for BCST400 ceramic sample indicating that the diffuseness of the ferroelectric transition minimizes for BCST250 sample. As the particle size decreases up to 250 rpm milling speed), the microscopic homogeneity in the composition increases due to improved ordered atomic arrangement. However, the introduction of crystal defects such as porosity in the system with further reduction in particle size destabilizes this ordered arrangement and increases diffusiveness around T_c [49].

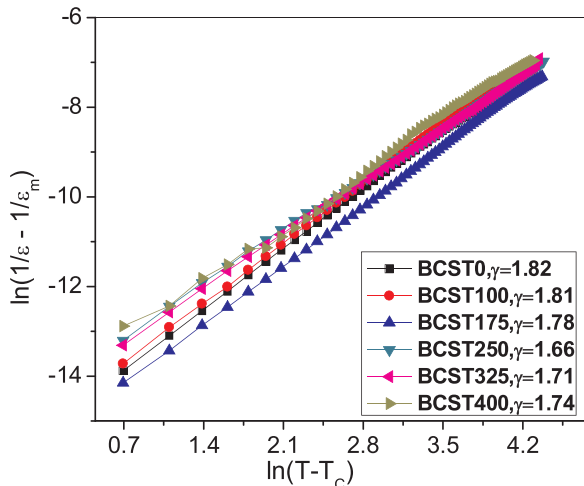


Fig. 9. Variation of $\ln(1/\epsilon - 1/\epsilon_m)$ with $\ln(T - T_c)$ for BCST0, BCST100, BCST175, BCST250, BCST325 and BCST400 ceramics.

3.5. Ferroelectric studies

Fig. 10a depicts the polarization hysteresis loops (P-E loops) measured at 50 Hz and 20 °C for BCST samples, milled at different milling speeds. The P-E loops obtained here clearly suggest the ferroelectric nature of the samples. The variation of the remnant polarization (P_r) and the coercive field (E_c) is shown in Fig. 10b as a function of milling speed for each sample. An escalation in P_r is detected with the increment in the milling speed, showing a peak for BCST325 ($5.09 \mu\text{C}/\text{cm}^2$) sample before rapidly decreasing for BCST400. An inverse trend is seen for E_c , with a decrease in its value up to BCST325 ($1.96 \text{ kV}/\text{cm}$) and an increase for BCST400. Rise in P_r value, and a corresponding drop in E_c suggests the gradual shifting of the samples into soft ferroelectric behavior.

Referring to Fig. 6, it is to be noted that the variations in the values for P_r and E_c with milling speed show a similar trend as that shown by the grain size up to BCST325. This indicates that till the speed of 325-rpm, larger grains experience ease in domain mobility and domain nucleation due to larger domain width which in turn causes the increase in P_r as observed earlier. Also, Arlt et al. [50] reported a “size-effect” present in BaTiO_3 due to which there is a dependency of the width of the domain on the grain size of the material. The domain width is found to be nearly constant for grain size more than $10 \mu\text{m}$ and decreases on a further decline in the grain size. A similar dependency of ferroelectricity on the sample grain size has been reported by numerous other researchers in various ceramic systems [20,21,51,52]. Moreover, it is known that the breaking through of the barrier is required for switching of the ferroelectric domain and an increase in the grain size decreases this energy barrier, making the polarization reversal process of a ferroelectric material much easier in large grains [53,54]. This leads to the rise in the value of P_r with a subsequent drop in the E_c value. However, the aforementioned contribution to ferroelectricity is highly masked in small-sized grains. Large depolarization field effects from these grains having a larger percentage of grain boundaries hinder polarization switching under application of field [55]. Although a deviation is shown for BCST400 sample, which shows a sudden decline in the P_r value, as opposed to the observed increasing trend. This exception can be attributed to the extremely high value for porosity (21.3 %) resulting in a poorer density of the sample which generates large internal stresses during domain switching leading in the decrement in the ferroelectricity [54].

Loop squareness, R_{sq} parameter used to examine the maximum polarization saturation attained by each sample at a certain field value is calculated using the formula:

$$R_{sq} = P_r/P_s + P_{1.1E_c}/P_r \quad (7)$$

where $P_{1.1E_c}$ is the value of polarization at 1.1 times the value of E_c value. R_{sq} is found to be 2 for a completely saturated hysteresis loop. A plot showing the variation of spontaneous polarization (P_s) and

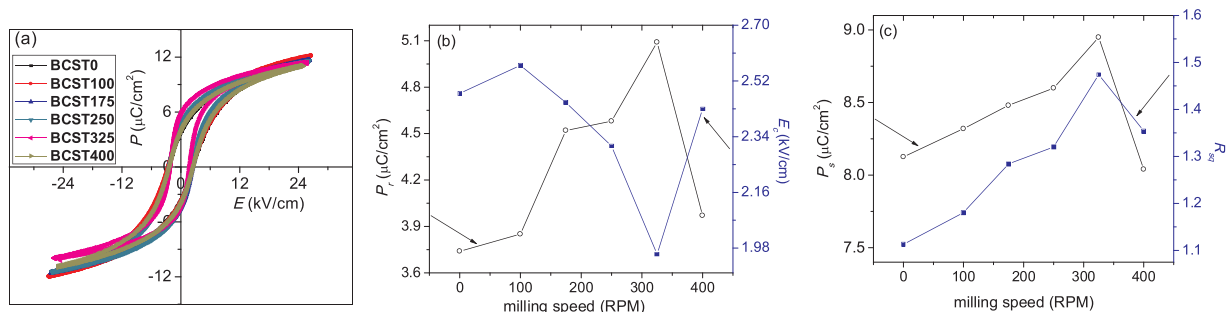


Fig. 10. (a) P-E hysteresis curve obtained at 50 Hz and 20 °C, (b) plots of P_r and E_c and (c) plots of P_s and R_{sq} , versus milling speed, for BCST ceramics.

squareness of the loop (R_{sq}) with the corresponding milling speeds for all the BCST samples is shown in Fig. 10c. Both these parameters can be seen exhibiting a rising trend with the increasing milling speed up to 325-rpm, after which their values can be seen decreasing. The behavior of P_s and R_{sq} illustrates that the ferroelectric nature for the BCST ceramic samples is improved for ceramics prepared from finer starting powders.

3.6. Piezoelectric studies

Fig. 11 shows the variation of the piezoelectric coefficient (d_{33}), which is a measure of charge density per unit stress, along with electromechanical coupling coefficient (k_p) with milling speed for the samples. Both the parameters can be seen increasing up to 175-rpm, having a d_{33} peak at 231 pC/N and k_p peak at 26.1 % for BCST175. Table 2 suggests that the changes observed in d_{33} and k_p values agree with the changes in the density of the samples.

According to the thermodynamic theory, d_{33} can be given by the formula [56]:

$$d_{33} = 2Q_{11}\epsilon_0 \epsilon_r P_s \quad (8)$$

where ϵ_r is the dielectric constant, P_s is the spontaneous polarization, ϵ_0 is the permittivity of free space and Q_{11} gives the electrostrictive coefficient of the substance. However, the influence of Q_{11} on the piezoelectric properties is minuscule as compared to the effects of ϵ_r and P_s . This is due to the development of extremely small magnitude displacements (< 5% of the lattice parameter) from quadratic electrostrictive strains present in the perovskite structures. These small displacements thus obtained, do not strongly affect the potential energy of the ion-pair and the lattice parameters which cause the independency of the piezoelectric properties on electrostrictive parameters [57]. In our present study, however, the parameter P_s does not have a large influence on the d_{33} value due to the degrading ceramic density at higher milling speeds. Therefore it is appropriate to say that the d_{33}

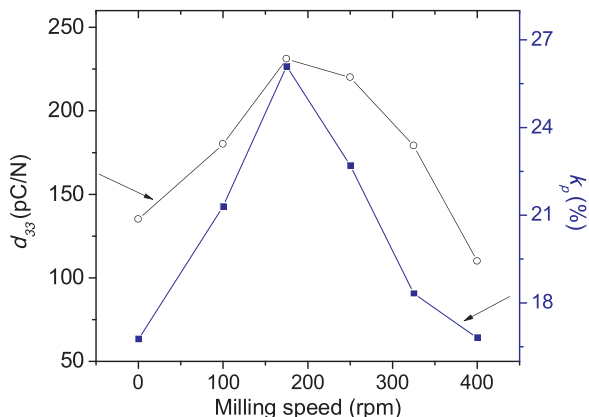


Fig. 11. Variations of k_p and d_{33} as a function of milling speed in BCST system.

value is in accordance with the ϵ_r values or the dielectric properties of the material which can also be confirmed by Table 2.

Table 1 also shows that the obtained trend is also in agreement with the crystalline size of the sample. In general, larger lattice size aids lattice distortions, thereby improving the piezoelectricity of the sample. Apart from this, the increase in the crystallite size decreases processes like pinning of domain walls, further resulting in less hindrance in the domain motion [58]. The increase in the domain mobility, in turn, increases the rate of polarization switching and the piezoelectric properties of the synthesized ceramics. There have been various reports of enhancement of the piezoelectric properties in other perovskite structures with large crystallite sizes [59,60]. However, nucleation of new domains and domain wall movement becomes more difficult with decreasing crystallite size as it forms a stable domain structure with grain size almost comparable to a single domain [43].

It can further be noted that the development of piezoelectric properties is also in accordance with the changes in the lattice strain (Table 1). Larger values of strain result in an anisotropic distortion of the internal structure of the ceramic crystal. Such distortions help in the strengthening of the spontaneous polarization, in turn, improving the piezoelectric properties for the ceramic. Another reason for the higher piezoelectric activity detected may be the ramification of the changing crystal symmetry at room temperature resulting from rising crystallite size as confirmed from the XRD analysis (Section 3.2). For systems with multi-domain orthorhombic symmetry (such as BCST100, BCST175 and BCST250) possessing twelve possible directions of P_s orientation, increase the probable orientation directions under the application of electric field; whereas for systems possessing tetragonal phase are left with six such possible orientation directions thereby suppressing piezoelectric contribution. Similar observation by Lee et al. in PbTiO_3 also suggests that the multi-domain crystallites require less activation energy for domain reorientation due to the absence of any clamping conditions [61].

4. Conclusion

Nanocrystalline powders of lead-free BCST system devoid of unwanted phases were successfully prepared by high energy ball milling technique using solid-state reaction method. The average particle size showed a colossal decline of about 97 % on increasing the milling speed from 0 – 400 rpm, fixing the milling time at 5 h. Further, the grain size rose gradually till 175-rpm sample accompanied by densification, whereas a further rise in milling speed resulted in rapid grain growth along with coarsening. A significant effect of milling conditions was observed in the structural behavior of BCST system. It exhibited an evolution from tetragonal to orthorhombic phase starting from 0 up to 250-rpm milling speed. However, stabilization of tetragonal symmetry was again observed for highest milling speed due to absence of any clamping conditions by neighboring crystallites. Lattice parameters including lattice strain, crystallite size and tetragonality (c/a) peaked for 175-rpm milled BCST ceramic before showing a decreasing trend. Optimum values of dielectric and piezoelectric properties were found

for 175-rpm, which can be attributed to the dense microstructure with orthorhombic phase structure. The systematic enhancement was achieved in piezoelectric properties (by 70 %) solely by decreasing the particle size of the starting powders and without changing the composition of the potential lead-free BCST piezoceramics which can have far-reaching significance in the search for alternatives to replace the far superior lead-based piezoelectric materials. Thus, this study not only revealed the possibilities of tailoring the preferred properties of the ceramic samples for various applications but also provided information about the complex phenomena occurring at nano-scale.

Declaration of Competing Interest

The authors report no declarations of interest.

Acknowledgements

The Department of Science and Technology, India financially supports the present work, under the Research Project No. EMR/2014/284. We would also like to acknowledge the directors of SSPL (solid state physics laboratory), Delhi and sophisticated analytical instrumentation facility (SAIF) AIIMS, Delhi for allowing us to make use of the required facilities for various measurements.

References

- N. Setter, D. Damjanovic, L. Eng, G. Fox, S. Gevorgian, Ferroelectric thin films: review of materials, properties, and applications, *J. Appl. Phys.* 100 (2006) 051606, <https://doi.org/10.1063/1.2336999>.
- T. Takenaka, H. Nagata, Y. Hiruma, Current developments and prospective of lead-free piezoelectric ceramics, *Jpn. J. Appl. Phys.* 47 (2008), <https://doi.org/10.1143/JJAP.47.3787> 3787e3801.
- D. Damjanovic, N. Klein, J. Li, V. Porokhonskyy, What can be expected from lead-free piezoelectric materials? *Funct. Mater. Lett.* 3 (1) (2010), <https://doi.org/10.1142/S1793604710000919> 5e13.
- Y.Q. Lu, Y.X. Li, A review on lead-free piezoelectric ceramics studies in China, *J. Adv. Dielectr.* 1 (03) (2011) 269e88, <https://doi.org/10.1142/S2010135X11000409>.
- J. Rödel, W. Jo, K.T.P. Seifert, E.M. Anton, T. Granzow, D. Damjanovic, Perspective on the development of lead-free piezoceramics, *J. Am. Ceram. Soc.* 92 (2009), <https://doi.org/10.1111/j.1551-2916.2009.03061.x> 1153e1177.
- M. Acosta, N. Novak, V. Rojas, S. Patel, R. Vaish, J. Koruza, G.A. Rossetti, J. Rödel, BaTiO₃-based piezoelectrics: fundamentals, current status, and perspectives, *Appl. Phys. Rev.* 4 (2017) 041305, <https://doi.org/10.1063/1.4990046>.
- W. Cai, C.L. Fu, J.C. Gao, C.X. Zhao, Dielectric properties and microstructure of Mg doped barium titanate ceramics, *Adv. Appl. Ceram.* 110 (2011) 181e185, <https://doi.org/10.1179/1743676110Y.0000000019>.
- X. Liu, M. Zhu, Z. Chen, B. Fang, J. Ding, X. Zhao, H. Xu, H. Luo, Structure and electrical properties of Li-doped BaTiO₃-CaTiO₃-BaZrO₃ lead-free ceramics prepared by citrate method, *J. Alloy. Comp.* 613 (2014) 219e225, <https://doi.org/10.1016/j.jallcom.2014.06.046>.
- T. Takenaka, H. Nagata, Current status and prospects of lead-free piezoelectric ceramics, *J. Eur. Ceram. Soc.* 25 (2005) 2693–2700, <https://doi.org/10.1016/j.jeurceramsoc.2005.03.125>.
- R. Gaur, A. Dhingra, S. Pal, K.C. Singh, Enhanced piezoelectric properties in vanadium-modified lead-free (K_{0.485}Na_{0.5}Li_{0.015})(Nb_{0.88}Ta_{0.1}V_{0.02})O₃ ceramics prepared from Nanopowders, *J. Alloys. Compd.* 625 (2015) 284–290, <https://doi.org/10.1016/j.jallcom.2014.11.134>.
- M. Chen, Z. Xu, R. Chu, Y. Liu, L. Shao, W. Li, S. Gong, G. Li, Polymorphic phase transition and enhanced piezoelectric properties in (Ba_{0.9}Ca_{0.1})(Ti_{1-x}Sn_x)O₃ lead-free ceramics, *Mater. Lett.* 97 (2013) 86–89, <https://doi.org/10.1016/j.matlet.2012.12.067>.
- L.F. Zhu, B.P. Zhang, L. Zhao, High piezoelectricity of BaTiO₃-CaTiO₃-BaSnO₃ lead-free ceramics, *J. Mater. Chem. C* 2 (2014) 4764–4771, <https://doi.org/10.1039/C4TC00155A>.
- Li.F. Zhu, B.P. Zhang, L. Zhao, S. Li, Y. Zhou, X.C. Shi, N. Wang, Large piezoelectric effect of (Ba,Ca)TiO_{3-x}Ba(Sn,Ti)O₃ lead-free ceramics, *J. Eur. Ceram. Soc.* 36 (2016) 1017–1024, <https://doi.org/10.1016/j.jeurceramsoc.2015.11.039>.
- K.C. Singh Chitra, Compositional optimization of lead-free (Ba_{1-x}Ca_x)(Ti_{1-y}Sn_y)O₃ ceramics: a structural and electrical perspective, *J. Alloys Compd.* 765 (2018) 869–877, <https://doi.org/10.1016/j.jallcom.2018.06.273>.
- M. Wu, X. Yuan, H. Lao, H. Chen, C. Chen, K. Zhao, D. Zhang, Enhanced actuation performance of piezoelectric fiber composites induced by incorporated BaTiO₃ nanoparticles in epoxy resin, *Phys. Lett. A* 381 (2017) 1641–1647, <https://doi.org/10.1016/j.physleta.2017.02.025>.
- V.V. Prisedskii, V.M. Pogibko, V.S. Polishchuk, Production and properties of nanostructured metal-oxide lead zirconate titanate piezoceramics, *Powder Metall. Met. C* 52 (2014) 505–513, <https://doi.org/10.1007/s11106-014-9553-y>.
- T. Karaki, K. Yan, T. Miyamoto, M. Adachi, Lead-free piezoelectric ceramics with large dielectric and piezoelectric constants manufactured from BaTiO₃ nanopowder, *Jpn. J. Appl. Phys.* 46 (2007) L97, <https://doi.org/10.1143/JJAP.46.L97>.
- L.B. Kong, T.S. Zhang, J. Ma, F. Boey, Progress in synthesis of ferroelectric ceramics materials via high energy mechanochemical technique, *Prog. Mater. Sci.* 53 (2008) 207–322, <https://doi.org/10.1016/j.pmatsci.2007.05.001>.
- K. Wu, W. Schultz, Aging of the weak-field dielectric response in fine- and coarse-grain ceramic BaTiO₃, *J. Am. Ceram. Soc.* 75 (1992) 3390, <https://doi.org/10.1111/j.1151-2916.1992.tb04439.x>.
- K. Ishikawa, K. Yoshikawa, N. Okada, Size effect on the ferroelectric phase transition in PbTiO₃ ultrafine particles, *Phys. Rev. B* 37 (1988) 5852, <https://doi.org/10.1103/PhysRevB.37.5852>.
- M.H. Frey, D.A. Payne, Grain-size effect on structure and phase transformations for barium titanate, *Phys. Rev. B* 54 (1996) 3158, <https://doi.org/10.1103/PhysRevB.54.3158>.
- D. McCauley, R.E. Newnham, C.A. Randall, Intrinsic size effect in BT glass ceramic, *J. Am. Ceram. Soc.* 81 (1998) 979–987, <https://doi.org/10.1111/j.1151-2916.1998.tb02435.x>.
- A. Testino, T. Buscaglia, M. Viviani, M. Buscaglia, P. Nani, Synthesis of BaTiO₃ particles with tailored size by precipitation from aqueous solutions, *J. Am. Ceram. Soc.* 87 (2004) 79, <https://doi.org/10.1111/j.1551-2916.2004.00079.x>.
- D. Kang, M. Han, S. Lee, S. Song, Dielectric and pyroelectric properties of barium strontium calcium titanate ceramics, *J. Eur. Ceram. Soc.* 23 (2003) 515, [https://doi.org/10.1016/S0955-2219\(02\)00085-7](https://doi.org/10.1016/S0955-2219(02)00085-7).
- H. Xu, L. Gao, J. Guo, Preparation and characterizations of tetragonal barium titanate powders by hydrothermal method, *J. Eur. Ceram. Soc.* 22 (2002) 1163, [https://doi.org/10.1016/S0955-2219\(01\)00425-3](https://doi.org/10.1016/S0955-2219(01)00425-3).
- T. Venugopal, K.P. Rao, B.S. Murty, Synthesis of Cu-W nanocomposite by high-energy ball milling, *J. Nanosci. Nanotechnol.* 7 (2007) 2376, <https://doi.org/10.1166/jnn.2007.418>.
- Y. Wang, Y. Li, C. Rong, P. Liu, Sm-Co hard magnetic nanoparticles prepared by surfactant-assisted ball milling, *J. Nanotechnol.* 18 (2007) 465701, <https://doi.org/10.1088/0957-4484/18/46/465701>.
- L.B. Kong, J. Ma, W. Zhu, O.K. Tan, Preparation and characterization of PLZT ceramics using high-energy ball milling, *J. Alloys Comp.* 322 (1-2) (2001) 290–297, [https://doi.org/10.1016/S0167-577X\(01\)00274-9](https://doi.org/10.1016/S0167-577X(01)00274-9).
- L.B. Kong, J. Ma, W. Zhu, O.K. Tan, Preparation of Bi₄Ti₃O₁₂ ceramics via a high-energy ball milling process, *Mater. Lett.* 51 (2001) 108–114, [https://doi.org/10.1016/S0925-8388\(01\)01256-7](https://doi.org/10.1016/S0925-8388(01)01256-7).
- M. Marutake, Approximate method of calculating electromechanical coupling factor, *Proc. Inst. Radio Eng.* 49 (5) (1961) 967.
- P.Y. Butyagin, Mechanical Disordering and Reactivity of Solids. *Advances in Mechanochemistry, Physical and Chemical Processes Under Deformation*, Harward Acad. Publ. 91, 1998, p. 165.
- A.I. Gusev, A.S. Kurlov, Production of nanocrystalline powders by high-energy ball milling: model and experiment, *Nanotechnology* 19 (2008) 265302, <https://doi.org/10.1088/0957-4484/19/26/265302>.
- C. Dong, PowderX: Windows-95-based program for powder X-ray diffraction data processing, *J. Appl. Crystallogr.* 32 (4) (1999) 838, <https://doi.org/10.1107/S0021889899003039>.
- M. Huang, T. Liu, Y. Deng, H. Geng, Y. Shen, Y. Lin, C.W. Nan, Effect of sintering temperature on structure and ionic conductivity of Li_{7-x}La₃Zr₂O_{12-0.5x} (x = 0.5–0.7) ceramics, *Solid State Ion.* 204-205 (2011) 41–45, <https://doi.org/10.1016/j.ssi.2011.10.003>.
- B.P. Zhang, L.M. Zhang, J.F. Li, X.N. Ding, H.L. Zhang, Effect of sintering temperature on electrical properties of Na_{0.5}K_{0.5}NbO₃ lead-free piezoelectric ceramics prepared by normal sintering, *Ferroelectrics* 358 (1) (2007) 188–195, <https://doi.org/10.1080/00150190701537323>.
- M.N. Rahaman, *Ceramic Processing and Sintering*, second ed., Marcel Dekker, Inc., New York, 2003.
- K.C. Singh, A.K. Nath, O.P. Thakur, Structural, electrical and piezoelectric properties of nanocrystalline tin-substituted barium titanate ceramics, *J. Alloys Comp.* 509 (2011) 2597–2601, <https://doi.org/10.1016/j.jallcom.2010.11.106>.
- B.D. Cullity, *Elements of X-ray Diffraction*, Addison and Wesley Publishing Company Inc., M.A, 1978 pp. 356.
- G.K. Williamson, W.H. Hall, X-ray line broadening from filed aluminium and wolfram, *Acta. Metall.* 1 (1) (1953) 22–31, [https://doi.org/10.1016/0001-6160\(53\)90006-6](https://doi.org/10.1016/0001-6160(53)90006-6).
- C. Wu, W. Duan, X.W. Zhang, Z. Liu, Effects of hydrostatic pressure on Pb(Zr_{1-x}Ti_x)O₃ near the morphotropic phase boundary, *J. Appl. Phys.* 108 (2010) 124102, <https://doi.org/10.1063/1.3520659>.
- J.F. Li, Z.X. Zhu, F.P. Lai, Thickness-dependent phase transition and piezoelectric response in textured Nb-Doped Pb(Zr_{0.52}Ti_{0.48})O₃ thin films, *J. Phys. Chem. C* 114 (2010) 17796, <https://doi.org/10.1021/jp106384e>.
- H.-I. Hsiang, F.S. Yen, Effect of crystallite size on the ferroelectric domain growth of ultrafine BaTiO₃ powder, *J. Am. Ceram. Soc.* 79 (1996) 1053–1060, <https://doi.org/10.1111/j.1151-2916.1996.tb08547.x>.
- M.T. Buscaglia, M. Viviani, V. Buscaglia, L. Mitoseriu, A. Testino, P. Nanni, Z. Zhao, C. Galassi, High dielectric constant and frozen macroscopic polarization in dense nanocrystalline BaTiO₃ ceramic, *Phys. Rev. B* 73 (2006) 064114, <https://doi.org/10.1103/PhysRevB.73.064114>.
- R. Zuo, J. Rodel, R. Chen, L. Li, Sintering and electrical properties of lead-free Na_{0.5}K_{0.5}NbO₃ piezoelectric ceramics, *J. Am. Ceram. Soc.* 89 (6) (2006) 2010, <https://doi.org/10.1111/j.1551-2916.2006.00991.x>.
- R. Gaur, M. Sangal, A. Dwivedi, K.C. Singh, Lead-free vanadium-substituted

- ($K_{0.485}Na_{0.5}Li_{0.015}$)($Nb_{0.9}Ta_{0.1}$) O_3 piezoceramics synthesized from nanopowders, *J. Mater. Sci.: Mater. Electron* 25 (2014) 3195, <https://doi.org/10.1007/s10854-014-2003-2>.
- [46] S. Wang, T.A. Tan, M.O. Lai, L. Lu, Structural and electrical characteristics of dysprosium-doped barium stannatetitanate ceramics, *Mater. Res. Bull.* 45 (2010) 279, <https://doi.org/10.1016/j.materresbull.2009.12.022>.
- [47] F. Jona, G. Shirane, *Ferroelectric Crystals*, Pergamon press, New York, 1993.
- [48] K. Uchino, S. Nomura, Critical exponents of the dielectric constants in diffused-phase-transition crystals, *Integr. Ferroelectr.* 44 (1982) 55–61, <https://doi.org/10.1080/00150198208260644>.
- [49] S.M. Pilgrim, A.E. Sutherland, S.R. Winzer, Diffuseness as a useful parameter for relaxor ceramics, *J. Am. Ceram. Soc.* 73 (1990) 3122, <https://doi.org/10.1111/j.1151-2916.1990.tb06733.x>.
- [50] G. Arlt, D. Hennings, G. de With, Dielectric properties of fine grained barium titanate ceramics, *J. Appl. Phys.* 58 (1985) 1619, <https://doi.org/10.1063/1.336051>.
- [51] J.S. Liu, S.R. Zhang, H.Z. Zeng, C.T. Yang, Y. Yuan, Coercive field dependence of the grain size of ferroelectric films, *Phys. Rev. B* 72 (17) (2005), <https://doi.org/10.1103/PhysRevB.72.172101> 172101.
- [52] S. Huo, S. Yuan, Z. Tian, C. Wang, Y. Qiu, Grain size effects on the ferroelectric and piezoelectric properties of $Na_{0.5}K_{0.5}NbO_3$ ceramics prepared by pechini method, *J. Am. Ceram. Soc.* 95 (4) (2012) 1383–1387, <https://doi.org/10.1111/j.1551-2916.2011.04992.x>.
- [53] C. Leu, C.Y. Chen, C.H. Chien, Domain structure study of $SrBi_2Ta_2O_9$ ferroelectric thin films by scanning capacitance microscopy, *Appl. Phys. Lett.* 82 (2003) 3493, <https://doi.org/10.1063/1.1576308>.
- [54] Z. Zhao, V. Buscaglia, M. Viviani, M.T. Buscaglia, L. Mitoseriu, A. Testino, M. Nygren, M. Johnsson, P. Nanni, Grain-size effects on the ferroelectric behavior of dense nanocrystalline $BaTiO_3$ ceramics, *Phys. Rev. B* 70 (2004) 024107, <https://doi.org/10.1103/PhysRevB.70.024107>.
- [55] Y. Tan, J. Zhang, Y. Wu, C. Wang, V. Koval, B. Shi, H. Ye, R. McKinnon, G. Viola, H. Yan, Unfolding grain size effects in barium titanate ferroelectric ceramics, *Sci. Rep.* 5 (2015) 9953, <https://doi.org/10.1038/srep09953>.
- [56] B.M. Jin, J. Kim, S.C. Kim, Effects of grain size on the electrical properties of $PbZr_{0.52}Ti_{0.48}O_3$ ceramics, *Appl. Phys. A* 65 (1997) 53, <https://doi.org/10.1007/s003390050541>.
- [57] F. Li, L. Jin, Z. Xu, S. Zhang, Electrostrictive effect in ferroelectrics: an alternative approach to improve piezoelectricity, *Appl. Phys. Rev.* 1 (2014) 011103, <https://doi.org/10.1063/1.4861260>.
- [58] K.C. Singh, C. Jiten, R. Laishram, O.P. Thakur, D.K. Bhattacharya, Structure and electrical properties of Li- and Ta-substituted $K_{0.5}Na_{0.5}NbO_3$ lead-free piezoelectric ceramics prepared from nanopowders, *J. Alloys Compd.* 496 (2010) 717, <https://doi.org/10.1016/j.jallcom.2010.02.181>.
- [59] C.A. Randall, N. Kim, J.P. Kucera, W. Cao, T.R. Shrout, Intrinsic and extrinsic size effects in fine grained morphotropic-phase-boundary lead ZirconateTitanate ceramics, *J. Am. Ceram. Soc.* 81 (1998) 677, <https://doi.org/10.1111/j.1151-2916.1998.tb02389.x>.
- [60] H. Takahashi, Y. Numamoto, J. Tani, K. Matsuta, J. Qiu, S. Tsurekawa, Lead-free barium titanate ceramics with large piezoelectric constant fabricated by microwave sintering, *Jpn. J. Appl. Phys.* 45 (2006) L30, <https://doi.org/10.1143/JJAP.45.L30>.
- [61] M.H. Lee, A. Halliyal, R.E. Newnham, Poling studies of piezoelectric composites prepared by co-precipitated $PbTiO_3$ powder, *Ferroelectrics* 87 (1988) 71, <https://doi.org/10.1080/00150198808201370>.

A Study of the Thermoluminescence Properties of Dysprosium doped Li_3PO_4 Phosphor

A Graduation Dissertation Report

by

Mrunmoy Jena

under the supervision of

Dr. Anant Pandey

Submitted to the University of Delhi for the degree of
BACHELOR OF SCIENCE
in Physics



Department of Physics
Sri Venkateswara College
University of Delhi
Dhaura Kuan, New Delhi, Delhi 110021

Certificate

This is to certify that the dissertation project titled “**An Extensive Study of the Thermoluminescence Properties of Dysprosium doped Li_3PO_4 Phosphor**” submitted to the **University of Delhi** for the degree of **Bachelor of Science in Physics**, is the record of bona fide research work done by Mrunmoy Jena under my supervision and guidance.



Dr. Anant Pandey
(Supervisor)

Assistant Professor
Sri Venkateswara College
University of Delhi
New Delhi-110021

Contents

Acknowledgement	v
List of Tables	vi
List of Figures	vii
Abstract	viii
1 Introduction	1
1.1 Overview	1
1.2 Historical Background	2
1.3 Mechanism of Thermoluminescence	3
1.4 Classification of Luminescence	5
1.4.1 On the basis of Characteristic Time	5
1.4.2 On the basis of Mode of Excitation	6
1.5 Models of Thermoluminescence	6
1.5.1 First Order Kinetics Model	7
1.5.2 Second Order Kinetics Model	8
1.5.3 General Order Kinetics Model	8
1.6 Application in Radiation Dosimetry	9
1.6.1 Properties of good TLD Materials	10
1.7 Rationale	11
2 Research Methodology	12
2.1 Methods of Synthesis	13
2.1.1 Co-Precipitation Method	13
2.1.2 Solid State Diffusion Method	13
2.2 Characterization Methods	14
2.2.1 X-Ray Diffraction	14
2.2.2 Fourier Transform Infrared Spectroscopy	15
2.2.3 Scanning Electron Microscopy	16

2.2.4	Transmission Electron Microscopy	17
2.3	Irradiation	18
2.4	Acquisition of TL data	19
2.5	Analysis of TL data	20
3	TL Study of $\text{Li}_3\text{PO}_4 : \text{Dy}$ (Co-Precipitation Method)	22
3.1	Experimental Procedure	22
3.2	Results and Discussion	23
3.2.1	Analysis of XRD Data	23
3.2.2	Analysis of FTIR spectrogram	24
3.2.3	TL Glow Curve Analysis	24
3.2.4	Dose Response	25
3.2.5	Glow Curve Deconvolution and Kinetic Parameters	26
3.3	Conclusion	27
4	TL Study of $\text{Li}_3\text{PO}_4 : \text{Dy}$ (Solid State Diffusion Method)	28
4.1	Experimental Procedure	28
4.2	Results and Discussion	29
4.2.1	Concentration Optimization	29
4.2.2	TL Glow Curve Analysis	30
4.3	Dose Response	31
4.3.1	Deconvolution and Calculation of Kinetic Parameters	32
4.4	Conclusion	34
5	Future Prospects	35

Acknowledgement

I am greatly indebted to my project supervisor, Dr. Anant Pandey whose guidance and patience has enabled me to produce this work. Needless to say, without his constant support and encouragement this would not have been possible. It was his faith in me that motivated me to work fervently on the project.

Further, I express my heartfelt gratitude towards Mr. Chirag Malik who has played an integral role in the project. He devoted a significant portion of his time in the midst of his own PhD completion, helping me master the nuances of experimental research. A large part of the research work was done at the Inter University Accelerator Centre and I am extremely grateful to Mr. Debashish Sen and Mr. Birendra Singh who have been generous enough to provide unhindered access to the Health Physics Lab and the irradiation facilities at IUAC.

This entire work is dedicated to my parents. The hardships that they have endured and overcome in their life have always fuelled me to work diligently towards achieving my goals. It is their incessant moral and emotional support that has enabled the successful completion of this dissertation project.

List of Tables

1.1	Classification of luminescence on the basis of mode of excitation	6
3.1	Kinetic parameters of the deconvoluted peaks of $\text{Li}_3\text{PO}_4 : \text{Dy}$ (co-precipitation method) for 1 kGy of gamma irradiation dose	27
4.1	Kinetic parameters of the deconvoluted peaks of $\text{Li}_3\text{PO}_4 : \text{Dy}$ (solid state diffusion method) for 1 kGy gamma irradiation dose	33
4.2	Kinetic parameters of the deconvoluted peaks of $\text{Li}_3\text{PO}_4 : \text{Dy}$ (solid state diffusion method) for 1 h of UV irradiation	34

List of Figures

1.1	Simplified illustration of TL mechanism	4
1.2	Classification of luminescence on the basis of characteristic time	5
2.1	Flowchart of solid state diffusion method	13
2.2	Schematic representation of x-ray diffraction	14
2.3	Schematic representation of Fourier Transform Infrared Spectroscopy	15
2.4	Schematic diagram of a Scanning Electron Microscope	16
2.5	Schematic diagram of a Transmission Electron Microscope	17
2.6	Schematic diagram of a Gamma Irradiation Chamber	18
2.7	Set up for acquisition of TL data	19
3.1	XRD pattern of $\text{Li}_3\text{PO}_4 : \text{Dy}$ (co-precipitation method)	23
3.2	FTIR spectrogram of $\text{Li}_3\text{PO}_4 : \text{Dy}$ (co-precipitation method)	24
3.3	TL glow curves of $\text{Li}_3\text{PO}_4 : \text{Dy}$ (co-precipitation method)	25
3.4	Dose response of $\text{Li}_3\text{PO}_4 : \text{Dy}$ (co-precipitation method)	25
3.5	Deconvoluted peaks of $\text{Li}_3\text{PO}_4 : \text{Dy}$ (co-precipitation method)	26
4.1	Concentration optimization of dopant in $\text{Li}_3\text{PO}_4 : \text{Dy}$ (solid state diffusion method)	29
4.2	TL glow curves of $\text{Li}_3\text{PO}_4 : \text{Dy}$ (solid state diffusion method) for gamma irradiation	30
4.3	TL glow curves of $\text{Li}_3\text{PO}_4 : \text{Dy}$ (solid state diffusion method) for UV irradiation	31
4.4	TL dose response of $\text{Li}_3\text{PO}_4 : \text{Dy}$ (solid state diffusion method)	31
4.5	Deconvoluted peaks of $\text{Li}_3\text{PO}_4 : \text{Dy}$ (solid state diffusion method)	32

Abstract

Falling under the broad family of luminescence, thermoluminescence is the phenomenon exhibited by certain inorganic phosphors which on absorbing radiation and subsequent heating, emit light. Numerous studies in the last few decades have been conducted on this phenomenon which have led to its applications in diverse fields among which is the field of radiation dosimetry. It has been found that certain phosphors exhibit a linear relationship between the absorbed radiation dose and their thermoluminescence intensity and therefore can be used as dosimeters for measuring unknown doses accurately and reliably in environments that involve human exposure to radiation.

As an effort towards developing such a desirable material for radiation dosimetry, a novel phosphor, Li_3PO_4 doped with a rare earth element, dysprosium is the focus of this study. In the present work, this phosphor has been synthesized using the co-precipitation method with 0.1 mol % dopant concentration and its characterization has been done followed by the analysis of its TL properties when irradiated by gamma rays. Further, as an extension of this study, the same phosphor was also synthesized using a three step solid state diffusion method for various concentrations of the dopant (from 0.1 to 0.5 mol %). The TL characteristics of this sample were then analysed by exposing it to both gamma and UV radiation.

Chapter 1

Introduction

1.1 Overview

Thermoluminescence is a process which involves the absorption of energy carried by radiation and its subsequent emission in the form of light (visible electromagnetic radiation) from certain crystalline solids after being heated. In contrast with the phenomenon of incandescence, this process generally takes place at a lower temperature and requires heat only as a trigger, the initiator of this process being the absorption of radiation. The phenomenon of thermoluminescence then consists of the three basic processes [1]:

- **Irradiation:** The material must have been exposed to electromagnetic or other ionizing radiation.
- **Storage/trapping:** The radiation must be trapped in the material for some time. Therefore, the material must possess an adequate band gap (semiconductor or insulator) and defects/impurities.
- **Thermally stimulated emission:** Heating of the material is required to make it emit the trapped energy.

These luminescent materials are mostly inorganic materials doped with some impurities and are generally known as phosphors. Thermoluminescent materials find applications in a large number of fields including radiation dosimetry, age estimation of archaeological and geological samples, defect analysis in solids and in biochemistry. The historical developments in research on thermoluminescence, its mechanism and application in the field of radiation dosimetry shall be discussed in brief in the subsequent sections.

1.2 Historical Background

The phenomenon of luminescence has aroused interest and been observed for millenia. However, due to the lack of systematic documentation and scientific understanding of the phenomenon, such records are limited in number. Reports of bioluminescence appear in Chinese literature dating back to the first and second century B.C., such as in the work *Hai Neishih Chou Chi* where the author mentions that while travelling on sea, one observes flying sparks when water is stirred, referring to the bioluminescent dinoflagellates present in the sea [2]. In *Naturalis Historia* (77 A.D.), Pliny the Elder gives an account of the 'cold fire' emanating from glow worms and jellyfish in the dark and also of ruby giving off a glow after being exposed to sunlight [3]. There are a few records of medieval alchemists being aware of the glow of certain minerals in the dark on being heated.

The earliest scientific record of thermoluminescence was made by Robert Boyle in 1663. He found that a glow was emitted from a diamond when he placed it in contact with a 'warm part' of his body. He further tried to stimulate light emission using other sources such as a candle, a hot iron and by friction. DuFay in 1738, concluded through his experiments on natural quartz that thermoluminescence was a manifestation of delayed phosphorescence and heat only stimulated the release of energy but was not the primary cause. The astronomer, Alexander Herschel discovered thermoluminescence of extraterrestrial materials by sprinkling dust obtained from a meteorite on a heated iron. In 1895, Weidemann and Schmidt were the first researchers to experimentally induce thermoluminescence in artificially produced phosphors using electron beams. Further work using ionizing radiation (from radium) to produce thermoluminescence in fluorites was done by Marie Curie in 1904 and by Rutherford, Chadwick and Ellis in the late nineteenth century. By and large, these experiments cemented the relationship between radiation and thermoluminescence.

Starting in the late 1940s, a simple mathematical treatment of thermoluminescence was obtained by Randall and Wilkins [4, 5] in 1945 through their first order kinetics model and by Garlick and Gibson [6] who gave a second order kinetics model for thermoluminescence in sulphides and silicates. Following these theoretical developments, thermoluminescence began to be applied in various fields starting with its application in the measurement of internal radiation doses received by cancer patients by Farrington Daniels in the 1950s. He found LiF to be an excellent material for this purpose due to its high sensitivity. A large number of investigations done later on established LiF:Mg,Ti as a standard dosimeter material which was then marketed by the Harshaw Chemical Company as TLD-100.

This dosimeter and other standard material such as TLD-700 (LiF:Mg,Cu,P), TLD-200 (CaF₂:Dy), TLD-900 (CaSO₄:Dy) continue to be used at present.

It became clear after the 1950s that thermoluminescence could be used in a large variety of applications apart from radiation dosimetry such as the study of radiation damage in crystals, age determination of rocks, stratigraphy (study of rock strata and archaeological remains found in them) and measurement of catalytic activity [7]. With the development of modern methods such as luminescence spectroscopy and powerful numerical techniques like the Monte Carlo method, TL phenomena are used to study quantum tunnelling [8], afterglow emitted from persistent phosphors [9] and manipulating the band gap of certain materials [10]. Following the discovery of thermoluminescence in chloroplasts by William Arnold and Helen Sherwood in 1957 [11], TL has become an integral tool in research on photosynthetic systems.

1.3 Mechanism of Thermoluminescence

A simplified explanation of TL [12, 13] based on the band theory of solids discusses the central role of trapping of charge carriers in this phenomenon. In insulators and semi-conductors, almost all the electrons occupy the valence band which is separated from the relatively unoccupied conduction band by an energy difference called the forbidden band gap (E_g). In perfect solids, the electrons cannot occupy energy states lying within this forbidden band. However, it is possible for electrons to do so in solids having natural structural defects or those in which impurities have been deliberately introduced as dopants.

When the thermoluminescent material (phosphor) is exposed to external radiation of energy $h\nu > E_g$, it leads to the ionisation of valence electrons and thereby creates electron-hole pairs (Figure 1.1). These charge carriers are then presented with two possibilities : almost immediate ($< 10^{-8}$ s) recombination or trapping for a longer period of time in the metastable states (defects) lying within the forbidden gap. The defect levels lying closer to the bottom of the conduction band serve as electron traps while those near the top of the valence band function as hole traps (recombination centres). Depending on the trap depth, electrons in some shallow traps can get detrapped even at room temperature, while in the deeper ones require an increase in temperature (by heating the material) to impart them sufficient energy to get detrapped. Each defect level therefore has an activation energy, E_a (the energy required to excite the electron from the trap to the conduction band) and a frequency (attempt to escape) factor, s associated with

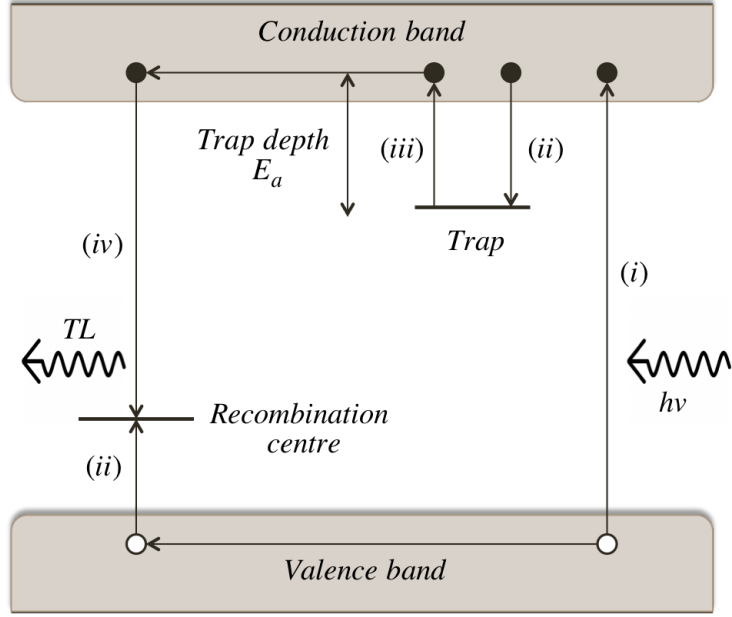


Figure 1.1: Simplified illustration of the mechanism of thermoluminescence: (i) electron-hole pair generation due to absorption of energy; (ii) trapping of electron and hole; (iii) release of electron on thermal stimulation (iv) charge carrier recombination and subsequent emission of light

it. Taking thermodynamic considerations into account, the Arrhenius equation gives the probability per unit time (p) of electron detrapping as:

$$p = s \exp\left(\frac{-E_a}{kT}\right) \quad (1.1)$$

Once the electron has been released from the trap, it reaches the conduction band and moves through it until it recombines with a hole in the recombination centre. If this recombination centre coincides with a luminescent centre, then its subsequent relaxation, emits energy in the form of visible photons. This gives rise to thermoluminescence.

As such the phenomenon of thermoluminescence falls under the broader mechanism of luminescence which involves the absorption of radiation, trapping of charge carriers, followed by detrapping using different modes of excitation and finally re-emission of the absorbed energy as electromagnetic radiation of longer wavelength (Stoke's shift). The different luminescent phenomena have been discussed in the following section.

1.4 Classification of Luminescence

The various luminescent phenomena can be broadly classified on the basis of modes of excitation and the characteristic time (time interval between the absorption of energy and emission of light).

1.4.1 On the basis of Characteristic Time

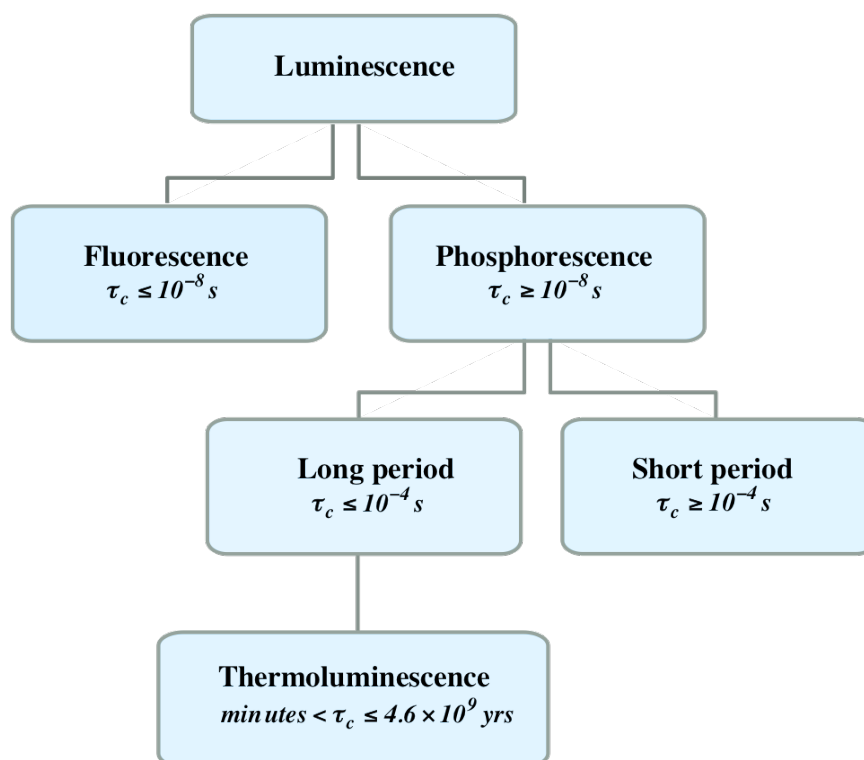


Figure 1.2: Classification of luminescence on the basis of characteristic time

In some luminescent phenomena, the emission of light occurs instantaneously ($\leq 10^{-8}$ s) after absorbing radiation and these fall under the category of fluorescence. In a few other, there is a time lag between absorption and emission of energy ($\geq 10^{-8}$ s) and these are categorized under phosphorescence (Figure 1.2). It is found that fluorescence is independent of temperature while phosphorescence shows a strong temperature dependence. Since phosphorescence covers a broad range of phenomena having characteristic time ranging from less than a second to hundreds of years, it has been further subdivided into short period ($\leq 10^{-4}$ s) and long period ($\geq 10^{-4}$ s) phosphorescence. The phenomenon of thermoluminescence is classified as a type of long period phosphorescence in which energy can be trapped for as long as thousands of years.

1.4.2 On the basis of Mode of Excitation

Although the fundamental mechanism in various luminescence processes remains more or less similar, excitation energy may be supplied to the material in numerous ways. These different types of luminescence, their modes of excitation and uses have been summarised in Table 1.1.

Table 1.1: Classification of luminescence on the basis of mode of excitation [3]

Type	Mode of excitation	Uses/Examples
Photoluminescence	Photons with wavelengths lying in UV or visible region	Detection of defects in certain minerals, characterization of electronic properties of semiconductors, band gap determination in solar cells
Radioluminescence	High energy photons (γ rays, X-rays) or neutrons	Used in scintillators, high energy particle detectors and X-ray radiography films
Crystalloluminescence	Salt crystallization from molten phase and liquid solutions	Used for growing crystallites from solutions such as NaCl, K_2SO_4 and other organic compounds
Chemiluminescence	Energy released from certain chemical reactions	Glowsticks, detection of trace quantities of poison in air, forensic investigation of crime scenes
Triboluminescence	Rubbing or crushing of crystals	Measurement of mechanical stress in devices, development of impact sensors
Electroluminescence	Excitation by an electric field	LEDs, in laser pointers, backlighting for LCD displays, electroluminescent night lamps
Cathodoluminescence	Impact of electrons on phosphors	Cathode ray tubes in televisions, in scanning electron microscopy
Thermoluminescence	Irradiation and subsequent heating at temperature below incandescence	Radiation dosimetry, archaeological and geological dating, stratigraphy, identification of irradiated food samples

1.5 Models of Thermoluminescence

Once the glow curve (variation of intensity with temperature) for a TL material is obtained, it is of essence to extract and study various parameters such as the activation energy, frequency factor and order of kinetics to understand the distribution and nature of the traps present and the physical processes taking place in the material. In order to accomplish this, a number of theoretical models of TL phenomena have been suggested, out of which three principal theories have been discussed in the the present section.

1.5.1 First Order Kinetics Model

Randall and Wilkins, in 1945 formulated a simple first order mathematical treatment of the phenomenon of thermoluminescence [4, 5]. In this model they made the following assumptions [14]

- Detrapping of electrons does not take place during irradiation of the thermoluminescent material.
- Electrons reside in the conduction band for a very short period.
- Charges that get detrapped undergo recombination in luminescent centres.
- None of the electrons released from traps get retrapped.
- The concentration of traps and recombination centres is independent of temperature.

Under these assumptions, the rate of detrapping at temperature, T is :

$$\frac{dn}{dt} = -pn \quad (1.2)$$

where the expression of p , the probability of electron escape per unit time is given by Eq. 1.1. On integration this relation gives us:

$$n = n_0 \exp \left[-s \exp \left(-\frac{E}{kT} \right) t \right] \quad (1.3)$$

At a constant temperature, the intensity (I) of TL is found to be proportional to the detrapping rate:

$$I = -c \left(\frac{dn}{dt} \right) = cpn \quad (1.4)$$

On inclusion of a uniform heating rate β ($= dT/dt$), the first order expression for the intensity as a function of temperature is obtained:

$$I(T) = n_0 s \exp \left(-\frac{E}{kT} \right) \times \exp \left[-\frac{s}{\beta} \int_{T_0}^T \exp \left(-\frac{E}{kT'} \right) dT' \right] \quad (1.5)$$

where n_0 denotes the number of electrons trapped at time $t = t_0$. Further, on maximising intensity at the peak temperature (T_M), the frequency factor is obtained:

$$s = \frac{\beta E}{kT_M^2} \exp \left(\frac{E}{kT_M} \right) \quad (1.6)$$

1.5.2 Second Order Kinetics Model

Garlick and Gibson, in their work on phosphorescence in 1948 [6] suggested an improvement in the theoretical model of Randall and Wilkins by assuming that the probability of free charge carriers getting re-trapped is equal to that of recombination in the luminescent centres. Under the assumption, the probability that a detrapped electron undergoes recombination is:

$$\frac{m}{(N - n) + m} = \frac{n}{N} \quad (1.7)$$

where n is the number of trapped electrons, N is the number of traps, m is the number of recombination centres. To maintain charge neutrality $m = n$. The final second order expression for the intensity is found to be:

$$I(T) = \frac{n_0^2 s' \exp\left(-\frac{E}{kT}\right)}{\left[1 + \frac{s' n_0}{\beta} \int_{T_0}^T \exp\left(-\frac{E}{kT'}\right) dT'\right]^2} \quad (1.8)$$

Here, $s' = s/n_0$ is the pre-exponential factor. In terms of the peak temperature, T_m the expression for s' comes out to be:

$$s' = \frac{1}{n_0} \left[\frac{2kT_M^2 \exp\left(-\frac{E}{kT_M}\right)}{\beta E} - \frac{\int_{T_0}^{T_M} \exp\left(-\frac{E}{kT'}\right) dT'}{\beta} \right]^{-1} \quad (1.9)$$

Here the pre-exponential factor (s') depends on the initial number of trapped electrons (n_0), in contrast to the frequency factor (s) obtained from the first order expression which was independent of n_0 .

1.5.3 General Order Kinetics Model

It was found in many experimental situations that the physical processes associated with TL need not strictly follow the first or second order kinetics. To model such phenomena, May and Partridge in 1964 gave a general order kinetics expression [15]. It assumed that that concentration of charge carriers in an energy level is proportional to n^b , where b

represents the order of kinetics ($1 \leq b \leq 2$). This gives the intensity of TL as:

$$I(T) = s'' n_0 \exp\left(-\frac{E}{kT}\right) \times \left[1 + \frac{s''(b-1)}{\beta} \int_{T_0}^T \exp\left(-\frac{E}{kT'}\right) dT'\right]^{(-\frac{b}{b-1})} \quad (1.10)$$

where $s'' = s' n_0^{(b-1)}$. In terms of the peak temperature (T_M), s'' is found to be:

$$s'' = \left[\frac{kT_M^2 b \exp\left(-\frac{E}{kT_M}\right)}{\beta E} - \frac{(b-1) \int_{T_0}^{T_M} \exp\left(-\frac{E}{kT'}\right) dT'}{\beta} \right]^{-1} \quad (1.11)$$

The corresponding expressions for the first and second order case can be recovered by substituting $b = 1$ and $b = 2$ respectively, in equations 1.10 and 1.11.

1.6 Application in Radiation Dosimetry

One of the most widespread applications of thermoluminescence is in the accurate and reliable measurement of radiation doses in certain environments. These include measurement of doses received by cancer patients undergoing radiotherapy (clinical dosimetry), monitoring radiation exposure in people working in nuclear power plants (personnel dosimetry), detection of radioactive radon gas in buildings (environmental dosimetry) among many other applications.

The fundamental principle in TL dosimetry is that the TL intensity is related to the absorbed dose (ideally, these two quantities are directly proportional over a broad range of doses). First, the dosimeter's variation of intensity with known doses is recorded (calibration). Then, the TL response of this material is recorded when exposed to an unknown radiation dose. On comparison of the TL intensity with the calibration signal, one can easily determine the unknown dose [16]. However, due to the non-ideal properties of TL materials and certain requirements for their applicability in different environments, not all TL materials qualify for use as dosimeters. Broadly, there are a few conditions that a TL material must satisfy in order to be considered as a good dosimetric material. These have been discussed below.

1.6.1 Properties of good TLD Materials

Some of the properties [17, 18] of good dosimetric materials are:

- **Linearity in dose response:** One of the most important requirements for TLDs is that they must exhibit an appreciable linear relationship between the absorbed dose and the emitted TL intensity over a large dose range. If it does not do so, errors might surface in the accurate determination of dose and careful calibration is required.
- **High sensitivity:** It is beneficial for a TL material to produce a high TL intensity in response to the absorbed dose. It can then be used for measuring very low doses, especially in personnel dosimetry.
- **Tissue equivalence:** If the material has an effective atomic number close to human tissue ($Z \approx 7.4$ for tissue) and has an energy response similar to tissues, then it is considered tissue equivalent. This has application in studying radiation effects on vital organs in medical environments.
- **Low fading:** It is essential that TL materials do not emit much light at room temperatures. If that happens, it cannot be further used for dosimetry at higher temperatures. Also, the material must have low optical fading, i.e. it must not give TL signal on exposure to light sources such as sunlight and fluorescent lamps.
- **Batch homogeneity:** Multiple batches of same TL material should give nearly identical TL intensity when exposed to the same dose. This uniformity is essential for the material to qualify as a standard dosimeter and ensure accurate measurement of doses.
- **Reproducibility:** An ideal dosimeter must retain the same sensitivity even after multiple cycles of irradiation and readout of TL. This is of significance especially in medical dosimetry.
- **Simple glow curve:** A material having a simple glow curve structure with a single peak has an advantage of easier computational analysis and accurate estimation of various trap parameters, in contrast to one having complex overlapping TL peaks.
- **Stability against other factors:** Also, it is desirable that such materials do not undergo physical changes in high humidity, react chemically with corrosive agents in the atmosphere or show spurious thermoluminescence (glow arising from causes other than irradiation of specimen).

1.7 Rationale

As an effort towards finding desirable materials for radiation dosimetry, recent works are directed towards investigating luminescence properties of orthophosphates doped with rare earths such as Tb^{3+} [19, 20], Ce^{3+} , Eu^{3+} [21], Eu^{2+} , Sm^{3+} [22]. These studies have found that they exhibit good TL/OSL dosimetric properties such as linear dose response, low fading, reusability and an excellent sensitivity. Also, PL properties of these compounds such as excitation wavelengths lying in near UV region have potential for applications in solid state lighting.

However, no studies reporting the thermoluminescence properties of one such promising orthophosphate, Li_3PO_4 doped with Dy^{3+} could be found in recent literature. Also, lithium phosphate has an effective atomic number ($Z_{\text{eff}} \approx 10.59$) and is considered as a tissue equivalent material. In order to assess the extent to which this material could be applied for dosimetric purposes (especially in the medical field), it is necessary to record and analyse its TL glow curves and extract various important parameters that provide information about the nature and distribution of traps present in the material. Therefore $\text{Li}_3\text{PO}_4:\text{Dy}$ has been chosen as the focus of this study. In the present work, the aforementioned material has been synthesized using two different methods: co-precipitation and solid state diffusion method. Subsequently TL data has been recorded post gamma and UV irradiation and analysis of the glow data has been accomplished using a computerised glow curve deconvolution technique. Based on the results obtained, scope of future applicability is discussed.

Chapter 2

Research Methodology

Research studies on the thermoluminescent properties of inorganic phosphors involve these four basic steps:

- **Synthesis:** The primary step involves weighing stoichiometric quantities of the reactants and the dopant and subsequent preparation of the doped phosphor. Various synthesis techniques include co-precipitation method, sol-gel synthesis, ball milling, solid state diffusion, combustion method and hydrothermal method. Two of these methods : co-precipitation and solid state diffusion, will be discussed here.
- **Characterization:** The characterization techniques give detailed information about the material such its surface morphology, internal structure and composition, size of particles, nature of chemical bonds present, etc. Some of these methods include X-ray Diffraction (XRD), Fourier Transform Infrared Spectroscopy (FTIR), Scanning Electron Microscopy (SEM) and Transmission Electron Microscopy (TEM).
- **Irradiation:** Preceding the TL study, the phosphor has to be exposed to different doses of radiation from an artificial radiation source (a radioactive isotope) such as Co^{60} , Tm^{170} , Ir^{192} and Cs^{137} for gamma radiation [23] and UV irradiation sources such as short wave UV lamps, mercury vapour backlights and excimer lamps [24]
- **Recording of TL data:** The recording of TL for the material by heating it takes place in a TL reader. Parameters such as heating rate, initial temperature and maximum temperature can be set as per the requirements.
- **Analysis of TL data:** The final and most important step is the study of the glow curves obtained by various deconvolution techniques and subsequent determination of trap parameters.

2.1 Methods of Synthesis

2.1.1 Co-Precipitation Method

This method is chosen as it is quite simple to perform, material synthesis takes less time, costly equipment isn't required and it is possible to have greater control over the composition and particle size [25]. In this method, there is a transfer of constituents present in trace quantities (dopant, in this case) to the precipitate along with the deposition of components present in macroscopic quantities in a supersaturated solution [26].

There are three main mechanisms involved in this process: (a) inclusion: the dopant occupies lattice sites in the carrier's crystal structure (b) occlusion: physical trapping of the dopant inside growing crystals (c) adsorption: the impurities get accumulated on the precipitate surface [27]. The products formed in this process are usually insoluble and can therefore be separated out by centrifugation and subsequent drying.

2.1.2 Solid State Diffusion Method

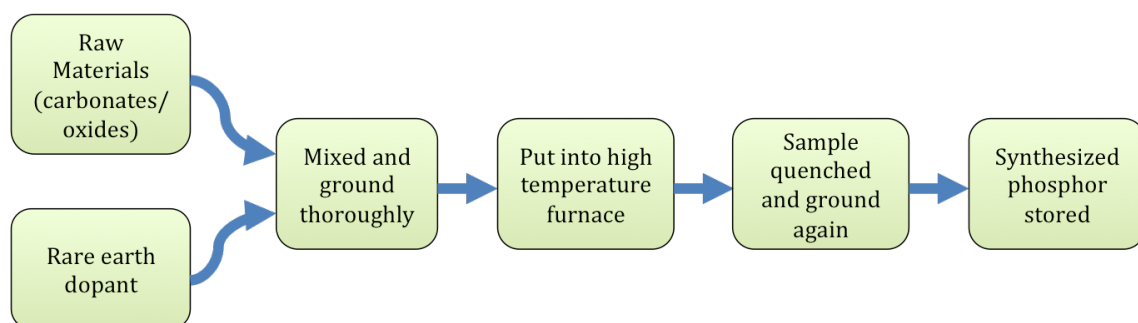


Figure 2.1: Flowchart of solid state diffusion method. Adapted from [28]

In this process, all the raw materials are thoroughly ground, mixed and then subjected to a high temperature. The heat provides thermal energy in order to cause atomic jumps from lattice point to another. This directional diffusion of mass species occurs when a concentration gradient or a gradient in electric, magnetic or chemical potential is present [29]. In the present study, once the starting materials and dopant were mixed and ground thoroughly, they were placed in alumina crucibles inside a high temperature muffle furnace. After heating at the required temperature and for a fixed duration, they are quenched at room temperature.

2.2 Characterization Methods

2.2.1 X-Ray Diffraction

This characterization technique is based on the fundamental principle that crystalline substances act as three dimensional diffraction gratings when x-rays are incident on them (interatomic spacing is of the order of x-ray wavelength). Each atom of the substance acts as a coherent source of secondary wavelets, the interference of which gives a diffraction pattern. The Bragg's law gives the condition for maxima [30] as:

$$2d \sin \theta = n\lambda \quad (2.1)$$

where d is the interplanar spacing of the crystal, n is the order of reflection (an integer), λ is wavelength of incident x-rays and θ is the incident angle. From this equation, it is possible to find the interplanar spacing (d_{hkl}) of all the crystallographic planes present in the sample.

For the characterization of the phosphor presented in this study, the powder XRD technique is used. The powdered sample is placed in the x-ray diffractometer and x-rays produced from a cathode ray tube are incident on it. These x-rays are monochromatic in nature, having a wavelength of 1.54184 Å corresponding to Cu- K_α transition. The diffractogram, a record of the diffracted intensity for each value of θ is made by varying the angle 2θ generally from 10 to 100 degrees in increments of 0.01 degree [31].

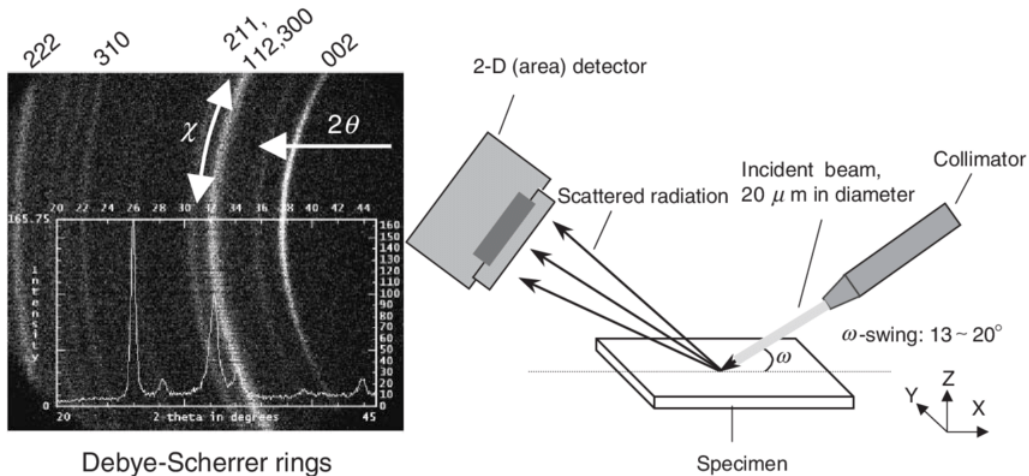


Figure 2.2: Schematic representation of x-ray diffraction [32]

To determine the average crystallite size, the Scherrer's equation [33] is used:

$$L = \frac{K\lambda}{\beta \cos \theta} \quad (2.2)$$

where L is the crystallite size, K is the dimensionless shape factor (≈ 0.89), β is the full width at half maximum, λ and θ have the same meanings as in equation 2.1.

The Williamson-Hall plot method [34] can be used to find the lattice strain along with the crystallite size by making a plot of $\beta \cos \theta$ vs. $\sin \theta$ to get a linear graph with a slope η (the lattice strain) and y-intercept $K\lambda/L$ using the equation:

$$\beta \cos \theta = \frac{K\lambda}{L} + \eta \sin \theta \quad (2.3)$$

In addition to this, XRD data can be used for phase identification, studying the crystallinity of the sample, the lattice parameters (a,b and c) and calculation of the unit cell volume [35].

2.2.2 Fourier Transform Infrared Spectroscopy

The Fourier Transform Infrared Spectroscopy technique serves to provide a unique 'chemical fingerprint' of the sample by giving information about the types of functional groups present and the quantitative concentration of each such compound.

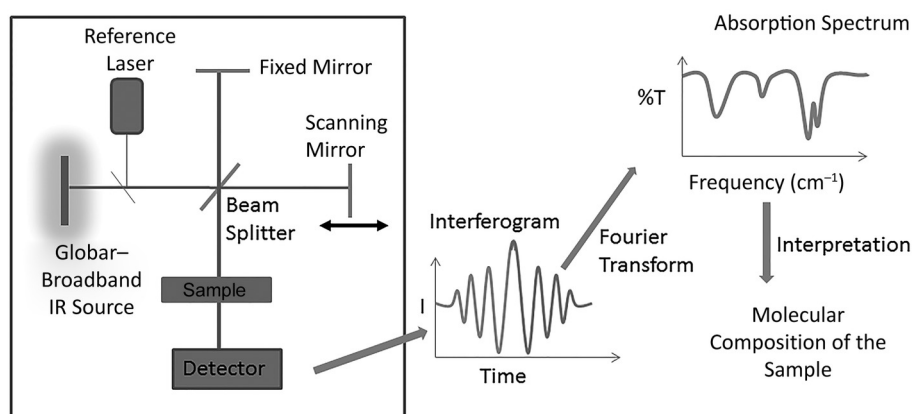


Figure 2.3: Schematic representation of Fourier Transform Infrared Spectroscopy [36]

This method involves an infrared source which emits a broad range of IR wavelengths, which then pass into a Michelson interferometer (see Figure 2.3). Varying the position of the movable mirror in the setup produces a corresponding modulation in the intensity of

different IR wavelengths. When this light exiting from the interferometer is incident on the sample, certain wavelengths excite the vibrational (such as symmetric/anti-symmetric stretching and bending) modes of the functional groups present, and these wavelengths get absorbed. The resultant intensity variation with optical path difference or time (interferogram) is recorded. Finally, a Fourier transform of this data gives a plot of the transmitted intensity/percentage transmission vs the wavenumber (in cm^{-1}). The FTIR spectra are generally obtained in the mid infrared spectrum ($400 - 4000 \text{ cm}^{-1}$) as most functional groups have their vibrational energy states lying in this region [37].

2.2.3 Scanning Electron Microscopy

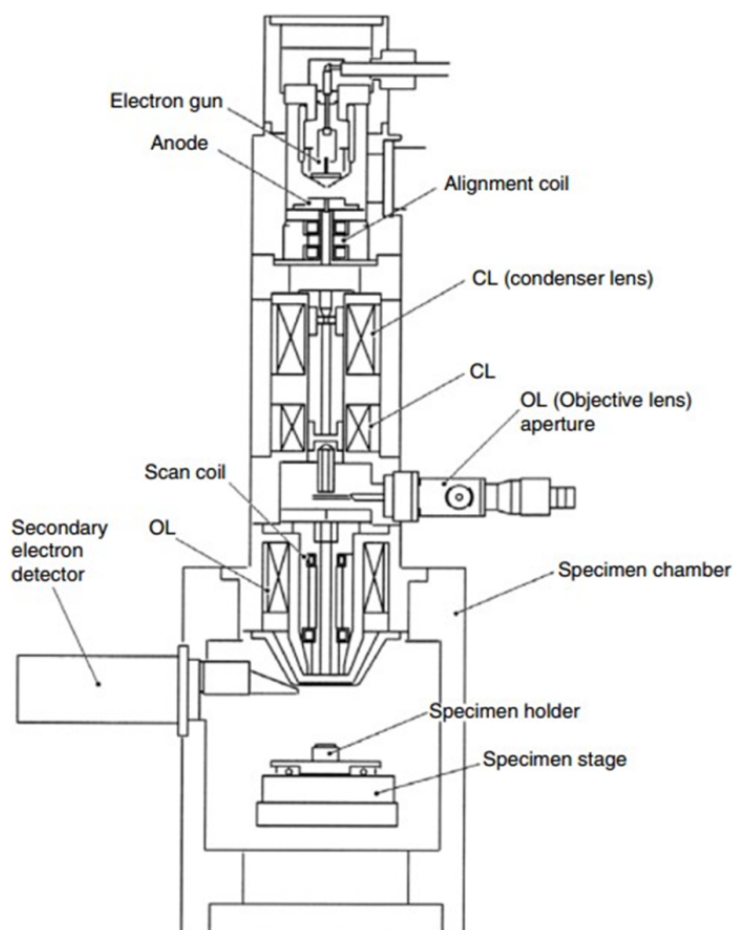


Figure 2.4: Schematic diagram of a Scanning Electron Microscope [38]

This characterization method provides a wealth of information such as the surface topography, chemical properties and composition, crystallographic structure, electrical response and highly magnified (upto 1,000,000x) images of the top layer (of thickness $\sim 1 \mu\text{m}$) of the sample [39]. The underlying principle of this technique is that the wavelength of the

radiation used for sample imaging must be reduced and the beam must be highly focused in order to increase the magnification of the image obtained and to achieve greater depth of field (three dimensional structure can be visualised) [40]. In this method, electrons of energies lying in the range 0.1-30 keV are generated by an electron gun and subsequently passed through a succession of apertures and electromagnetic condenser lenses which produce an extremely narrow beam. Scanning coils direct this beam to scan a selected surface of the sample. The electrons interact in various ways with the material, producing backscattered electrons, secondary electrons and Auger electrons along with characteristic x-rays. Collection of these emissions by the detectors and their analysis yields detailed information about the sample [41].

2.2.4 Transmission Electron Microscopy

This method is used for studying the internal structure of materials such as lattice defects, phase transformations, grain boundaries and analysing damage produced by radiation in the sample [42].

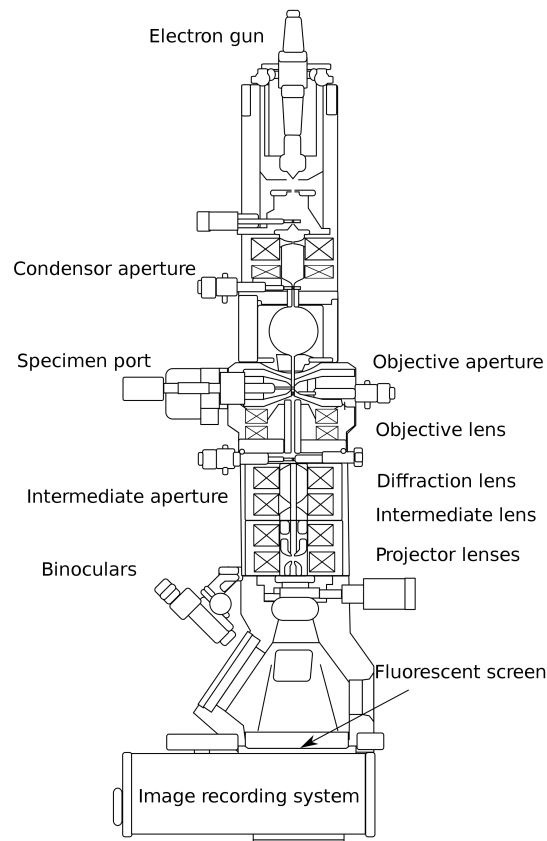


Figure 2.5: Schematic diagram of a Transmission Electron Microscope [43]

The set up of a Transmission Electron Microscope is similar to that of SEM in terms of the mechanism used to high magnification, resolution and excellent depth of field. However, this technique works by passing the focused electron beam through the specimen to be studied. For electrons to penetrate through, they have higher energies (around 100-400 keV) and the sample thickness is kept as small as possible ($< 100\text{nm}$) [44]. Once these electrons pass through the sample, they give a diffraction pattern which is recorded by a CCD (Charge Coupled Device) sensor. Various imaging methods are used in TEM such as bright and dark field imaging and Selected Area Diffraction which can be used to analyse the sample.

2.3 Irradiation

For gamma irradiation of the samples, an equipment called a Gamma Irradiation Chamber is used. This equipment consists of an artificial source of gamma radiation such as Co^{60} or Cs^{137} usually in the form of pellets, rods or metal slugs.

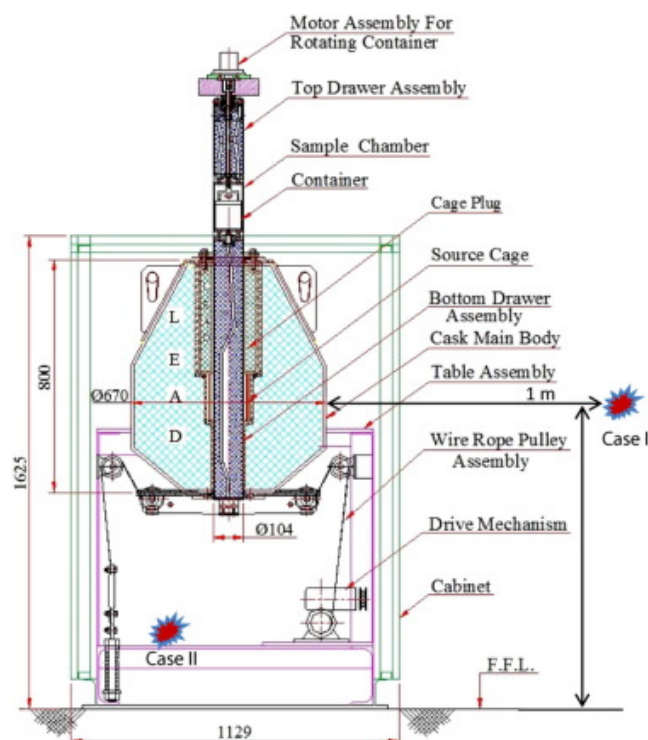


Figure 2.6: Schematic diagram of a Gamma Irradiation Chamber [45]

These sources are doubly encapsulated in stainless steel which is placed inside a source cage assembly. To protect the users from radiation, these are shielded by lead and another

layer of stainless steel [46]. For irradiation of phosphors presented in this study, a 1200 BRIT Gamma Irradiation Chamber available at the Inter University Accelerator Centre was used. This gamma chamber uses a Co^{60} source. A uniform dose delivery rate can be set in this instrument and the corresponding irradiation time is set automatically.

2.4 Acquisition of TL data

After irradiation of the sample, a TLD Reader is used to record the TL data. In this study, the TL data is collected with a Harshaw TLDTM Model 3500 Manual Reader. It has a sample drawer consisting of a contact planchet heater onto which a small quantity of the powdered sample is loaded. The heating rate, initial and maximum temperature upto which sample is to be heated and other parameters can be set through the programmable heating system provided in the instrument. Once the heating starts, the TL light signal is captured by the photomultiplier tube and sent to the ScientificTM WinREMSTM software which creates an ASCII file containing the variation of TL intensity with temperature [47]. For the present study, 5 mg of the material was loaded onto the planchet, a linear heating rate of $5^{\circ}\text{C}/\text{s}$ and temperature range of 50°C to 400°C was selected.

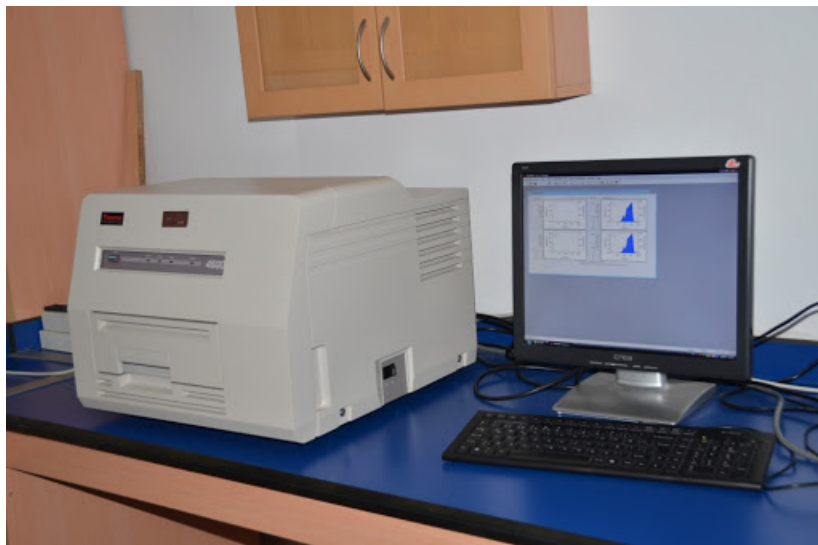


Figure 2.7: Set up for acquisition of TL data [48]

2.5 Analysis of TL data

Following the recording of TL glow curves for different radiation doses, the analysis of TL data can be done through various methods such as initial rise method [6], variable heating rate method [49] and isothermal decay method [15]. However, the thermoluminescence analyses presented in this study are done using the Computerised Glow Curve Deconvolution Method (CGCD) due to its ease of use and higher accuracy, as demonstrated in many studies [50–53]. To carry out curve fitting and deconvolution of TL data, GlowFit software [54] is used in the present work. Initially, the guess number of peaks is entered and approximate positions of the peaks are selected manually. The software then performs curve fitting using an iterative method based on the Levenberg–Marquardt method. After a satisfactory number of iterations (such that the χ^2 function is minimized), the fitted curve along with the deconvoluted peaks is present as the result, with the temperature and intensity of each peak. Additionally, a Figure of Merit (FOM) value is also generated:

$$FOM = \frac{\sum_i |y_i - y(x_i)|}{\sum_i y_i} \times 100\% \quad (2.4)$$

where y_i is the recorded value of the function at the i^{th} point and $y(x_i)$ is the value of fitted function at the i^{th} point. A good fit is generally indicated by a FOM value less than 2.5 % [55]. Subsequently to compute other trap parameters such as the frequency factor (s), activation energy (E) and order of kinetics (b), the peak shape method devised by R.Chen [56] is used. In this method, the values of τ (half width of low temperature portion), δ (half width of high temperature portion) and ω (total half width) are first computed for each deconvoluted peak:

$$\tau = T_m - T_1; \quad \delta = T_2 - T_m; \quad \omega = T_2 - T_1 \quad (2.5)$$

where T_1 is the low temperature at half intensity, T_2 is the high temperature at half intensity and T_m is the peak temperature. A geometrical shape factor $\mu'_g = \delta/\omega$ is then calculated. Further three more parameters are computed:

$$c_\tau = 1.51 + 3.0 (\mu'_g - 0.42); \quad b_\tau = 1.58 + 4.2 (\mu'_g - 0.42) \quad (2.6)$$

$$c_\delta = 0.976 + 7.3 (\mu'_g - 0.42); \quad b_\delta = 0 \quad (2.7)$$

$$c_\omega = 2.52 + 10.2 (\mu'_g - 0.42); \quad b_\omega = 1 \quad (2.8)$$

The activation energy is then found by using:

$$E_\alpha = c_\alpha(kT_m^2/\alpha) - b_\alpha(2kT_m) \quad (2.9)$$

where α can be τ , δ or ω depending on whether equation 2.6 , 2.7 or 2.8 is used. It is found that the equation 2.6 gives minimal error in the calculation of activation energy, so E is calculated using $\alpha = \tau$. Further the frequency factor (s) is calculated using:

$$s = \frac{\beta E}{kT_m^2[1 + (l - 1)\Delta]} \cdot \exp(E/kT_m) \quad (2.10)$$

where l is the order of kinetics and $\Delta = 2kT_m/E$. The order of kinetics is calculated from a graphical relationship between l and μ'_g provided in [56].

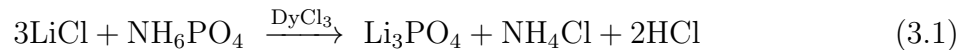
Chapter 3

TL Study of $\text{Li}_3\text{PO}_4 : \text{Dy}$ (Co-Precipitation Method)

3.1 Experimental Procedure

For the preparation of $\text{Li}_3\text{PO}_4 : \text{Dy}$, the chemical co-precipitation method was used. The starting materials: lithium chloride (LiCl), ammonium dihydrogen phosphate (NH_6PO_4) and 0.1 mol % of dysprosium chloride (DyCl_3) were first weighed in stoichiometric quantities, using a dividing factor of 10 to limit the amount of reactants used.

Lithium chloride was dissolved in 100 ml of distilled water and 0.1 mol % of dysprosium chloride was added to it. Subsequently, another solution of ammonium dihydrogen phosphate in distilled water was added to it. This process was done slowly, drop by drop while stirring the LiCl solution concurrently using a magnetic stirrer. Lithium phosphate doped with dysprosium was precipitated from the solution. This process can be represented as:



The solution was kept undisturbed for a while to allow the prepared material to be completely precipitated. It was then separated out by centrifugation at a rate of 2000 rpm for a duration of 10 minutes, carried out twice. Subsequently, the collected sample was dried on a heating mantle at a moderate temperature, to evaporate the water and other dissolved impurities. Annealing of the phosphor was carried out at a temperature of 900°C for a period of 1 hour, after which it was thermally quenched at room temperature. The prepared phosphor was then collected.

The collection of XRD data was carried out by the Bruker AXS D8 ADVANCE diffractometer that uses a graphite monochromator and produces Cu-K α x-rays of wavelength 1.54184 Å. The Perkin Elmer Fourier Transform Spectrometer was used to record the FTIR spectrum (4000 – 400 cm $^{-1}$). The 1200 BRIT Gamma Irradiation Chamber was used to carry out γ -irradiation of this material in the dose range of 10 Gy to 4 kGy. For the acquisition of TL data, the Harshaw TLDTM Model 3500 Manual Reader was used.

3.2 Results and Discussion

3.2.1 Analysis of XRD Data

The x-ray diffraction pattern for Li₃PO₄ : Dy has been shown in Figure 3.1. The sharp, intense peaks found in the XRD pattern show that the sample was formed in crystalline phase [57]. It was found from analysis of the XRD data that the phosphor has an orthorhombic crystal structure, i.e. all three edge lengths are unequal ($a \neq b \neq c$) and they are mutually orthogonal ($\alpha = \beta = \gamma$). The cell edge lengths are: $a = 13.18$ Å, $b = 7.04$ Å and $c = 5.43$ Å. The cell volume was calculated to be 503.83 Å³. The average crystallite size was computed to be 71.9 nm using the Scherrer's equation (equation 2.2).

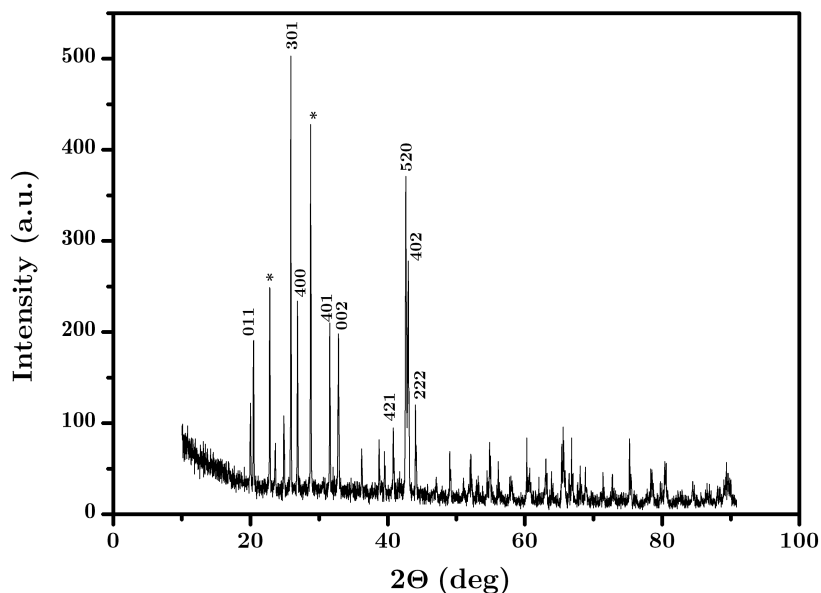


Figure 3.1: X-ray diffraction pattern of Li₃PO₄ : Dy

3.2.2 Analysis of FTIR spectrogram

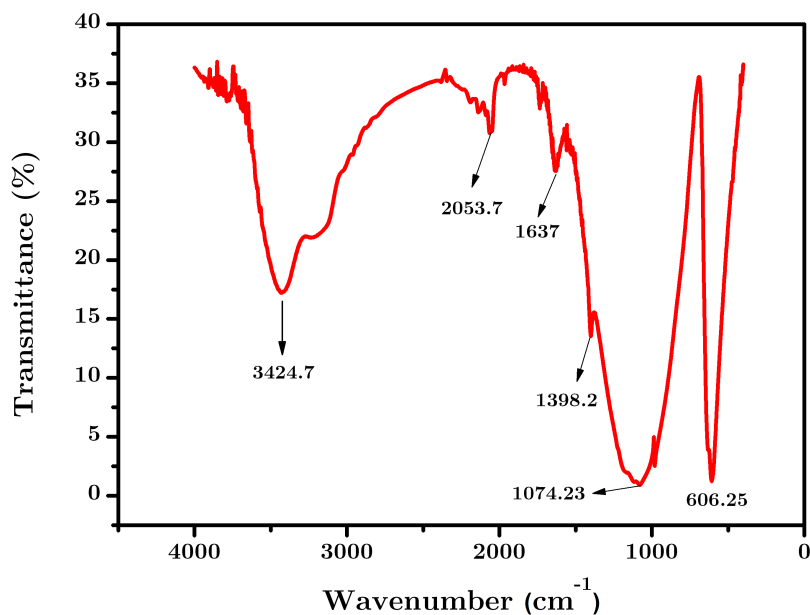


Figure 3.2: Fourier Transform Infrared spectrogram of Li₃PO₄ : Dy

Figure 3.2 shows the Fourier Transform Infrared spectrogram of Li₃PO₄ : Dy. Due to the O-P-O bending mode, a vibrational band is present at 606.25 cm⁻¹. Also, a band around 1074.23 cm⁻¹ is observed due to the P-O stretching mode [58, 59]. These two bands present in the FTIR spectrogram confirm phosphate bonding in the material. Further, the peaks observed at 3424.7 cm⁻¹, 2053.7 cm⁻¹, 1637 cm⁻¹ and 1398.2 cm⁻¹ show the presence of moisture and OH groups.

3.2.3 TL Glow Curve Analysis

The glow curves of Li₃PO₄ : Dy for gamma irradiation doses starting from 10 Gy to 4 kGy and in the range of 50 to 400°C are shown in Figure 3.3. For each of them, it is found on preliminary observation that there are two peaks, a minor peak at low temperature and the main dosimetric peak around 250°C. It is considered advantageous for a TL phosphor to exhibit a peak at high temperature (around 200-250°C) so as to minimize thermal fading and at the same time being low enough to circumvent infrared emission which happens at higher temperatures [1].

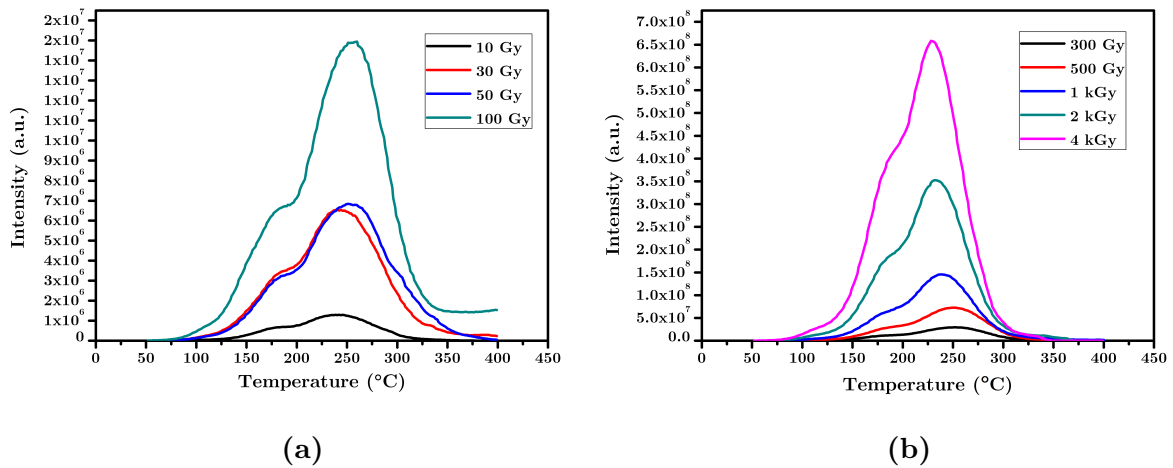


Figure 3.3: TL glow curves of $\text{Li}_3\text{PO}_4 : \text{Dy}$ for doses in the range of (a) 10 Gy to 100 Gy and (b) 300 Gy to 4 kGy

3.2.4 Dose Response

A log-log plot of the peak TL intensity v/s dose (10 Gy - 4 kGy) is shown in Figure 3.4. It is found that the linear fit for this plot has an R^2 value of 0.93449 which is quite high. It can therefore be seen that the phosphor exhibits a good linearity between intensity and dose throughout this range.

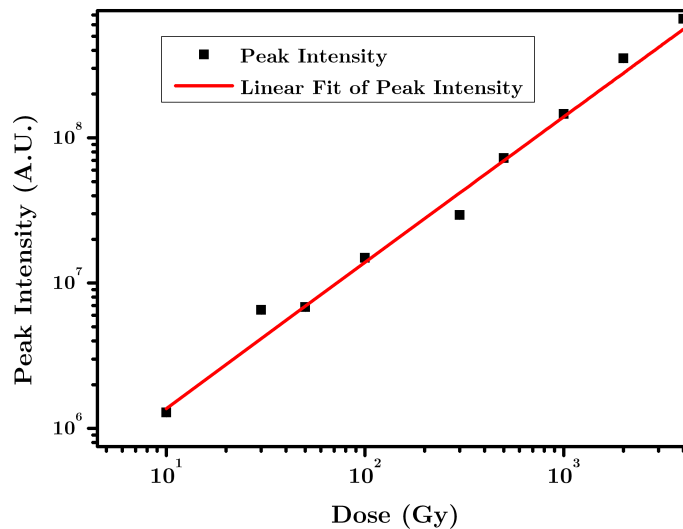


Figure 3.4: Dose response of $\text{Li}_3\text{PO}_4 : \text{Dy}$

On increasing irradiation dose up to 100 Gy, it is found that the prominent peak tends to

shift towards higher temperatures (from 239°C to 260°C). This can be possibly explained by the fact that the retrapping happens more often as compared to recombination at low temperature. This is because of the greater contribution of deeper traps. For doses higher than 100 Gy, it is found that the peaks shift towards lower temperature (from 260°C to 228°C). This kind of behaviour has been observed for peaks exhibiting second order kinetics [60].

3.2.5 Glow Curve Deconvolution and Kinetic Parameters

The curve fitting and deconvolution to find the constituent peaks was done using the computerized glow curve deconvolution technique (CGCD). For an irradiation dose of 1 kGy, it was found that the glow curves consists of two peaks: a prominent peak at $T_m = 239^\circ\text{C}$ and a minor peak at $T_m = 176^\circ\text{C}$, which have been shown in Figure 3.5. A good Figure of Merit value of 2.127 % was obtained for the fitted curve. As discussed in Section 2.5, the peak shape analysis devised by R. Chen [56] was used for calculation of the activation energy, order of kinetics and frequency factor for the constituent peaks. The kinetic parameters are given in Table 3.1.

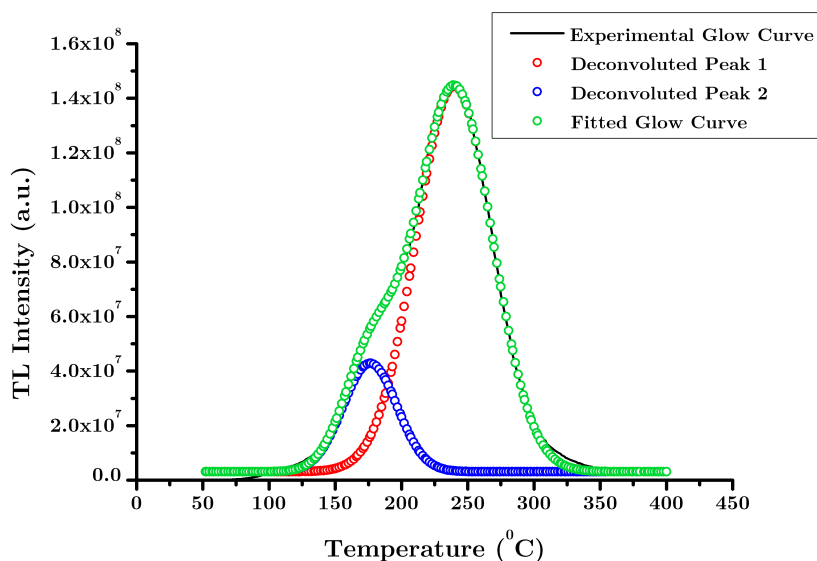


Figure 3.5: Deconvoluted peaks of $\text{Li}_3\text{PO}_4 : \text{Dy}$ for 1 kGy dose

Table 3.1: Kinetic parameters of the deconvoluted peaks of $\text{Li}_3\text{PO}_4 : \text{Dy}$ for 1 kGy gamma dose

Peak	Peak Temperature $T_m(^{\circ}\text{C})$	Geometrical shape factor μ_g	Order of Kinetics b	Frequency Factor $s(\text{sec}^{-1})$	Activation Energy $E(\text{eV})$
1	176.005	0.505	1.9	3.73×10^{11}	1.078
2	239.006	0.511	1.9	2.842×10^9	1.028

3.3 Conclusion

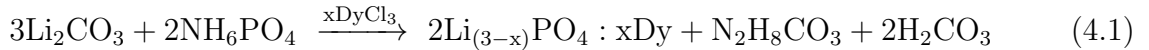
In this study, synthesis of Li_3PO_4 with 0.1 mol % Dysprosium as the dopant was done by the co-precipitation method. Confirmation of the nanocrystallinity of the sample was done through XRD analysis and it was found that the phosphor has an orthorhombic structure. Preliminary observations showed that there are two TL peaks, a minor peak at low temperature and the dosimetric peak at high temperature ($\approx 250^{\circ}\text{C}$). A good linearity was exhibited by the phosphor over the range of measured doses. The computation of trap parameters confirmed the presence of two peaks: the smaller one at 176°C and the intense TL peak at 239°C . Further, both peaks were found to exhibit second order kinetics.

Chapter 4

TL Study of $\text{Li}_3\text{PO}_4 : \text{Dy}$ (Solid State Diffusion Method)

4.1 Experimental Procedure

For this study, $\text{Li}_3\text{PO}_4 : \text{Dy}$ was prepared using the solid state diffusion method. Initially, lithium carbonate (Li_2CO_3), ammonium dihydrogen phosphate (NH_6PO_4) and different concentrations of dysprosium chloride (0.1, 0.2, 0.3, 0.4 and 0.5 mol %) were weighed in stoichiometric ratio (using a dividing factor of 40). These were then mixed thoroughly using a mortar and pestle along with the addition of acetone to form a thick paste. This paste was dried on a hot plate at a temperature of 50°C for 30 minutes. It was then subjected to a three step diffusion process by annealing it in a muffle furnace at 200°C for 1 h, 400°C for 2 h followed by 800°C for a duration of 3 h. Subsequently, the prepared phosphor was quenched at room temperature and collected. The same procedure was followed for all concentrations of the dopant. This process can be represented as:



where $x = 0.001, 0.002, 0.003, 0.004, 0.005$ mol (different concentrations of the dopant) The 1200 BRIT Gamma Irradiation Chamber was used to carry out γ -irradiation of this material in the dose range of 10 Gy to 6 kGy. UV irradiation was done at a wavelength of 254 nm, for irradiation duration ranging from 0.5 to 5 h, using a UV lamp. For the acquisition of TL data, the Harshaw TLDTM Model 3500 Manual Reader was used. The TL was acquired within the temperature range of 50 to 400°C with a heating rate of $5^\circ\text{C}/\text{s}$. 5 mg of the sample was taken for each of the TL readings.

4.2 Results and Discussion

4.2.1 Concentration Optimization

The effect of concentration of dopant on the TL intensity was studied for both gamma and UV irradiation. This variation has been shown in Figure 4.1 for gamma dose of 1 kGy and for UV irradiation at wavelength of 254 nm for 1 hr.

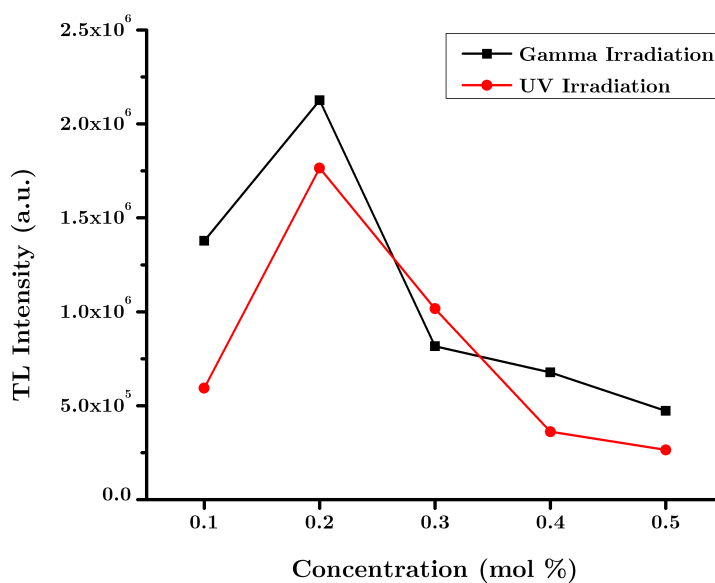


Figure 4.1: Concentration optimization of dopant in $\text{Li}_3\text{PO}_4 : \text{Dy}$ for 1 kGy dose of gamma radiation and UV irradiation for 1 hr

It is found that for both gamma and UV irradiation, the TL intensity first increases from 0.1 mol % and reaches a maximum at 0.2 mol %. There is a sharp decrease beyond that upto 0.3 mol % and 0.4 mol % in the case of gamma irradiation and UV irradiation respectively. At higher concentrations, the TL intensity keeps decreasing gradually. This is due to the well known phenomenon of concentration quenching. On initially increasing the concentration, the number of traps/luminescent centres increases thereby leading to a rise in the TL intensity which reaches a maximum at a particular concentration. However on further increase of concentration, a large number of traps are present in close proximity with each other due to which detrapped electrons are again trapped by these defect levels. This leads to a drop in TL intensity on increasing concentration beyond a certain limit [61]. For further study of TL properties, the phosphor with the optimum concentration (0.2 mol %) is chosen as it gives maximum TL intensity.

4.2.2 TL Glow Curve Analysis

The glow curves for $\text{Li}_3\text{PO}_4 : \text{Dy}$ for gamma irradiation doses in the range of 10 Gy to 6 kGy and in the range of 50 to 400°C are shown in Figure 4.2 while those for UV irradiation at 254 nm wavelength and for irradiation time varying from 0.5 h to 5 h are shown in Figure 4.3.

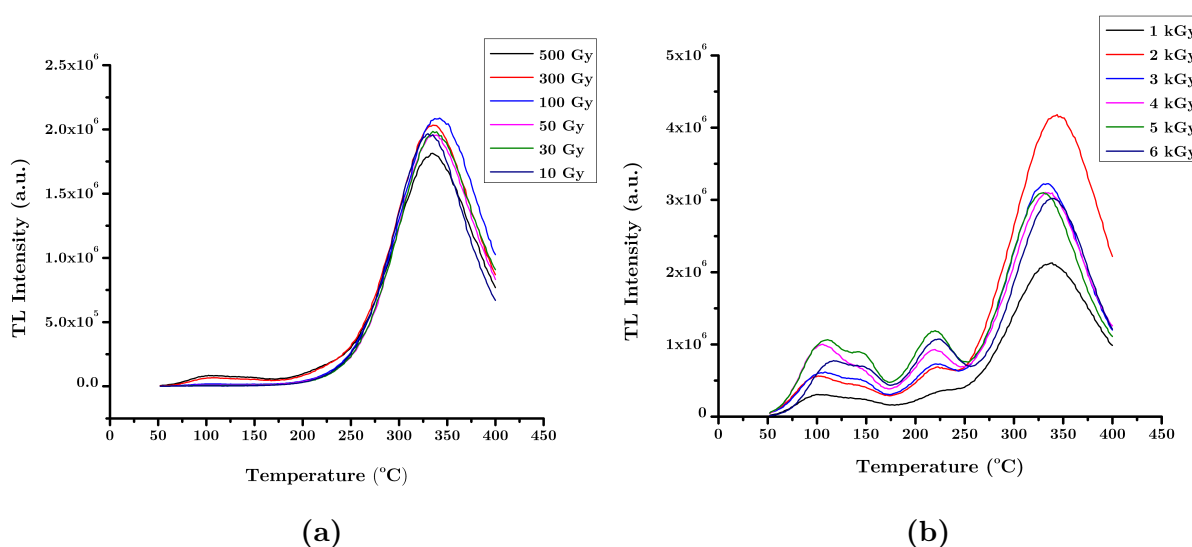


Figure 4.2: TL glow curves of $\text{Li}_3\text{PO}_4 : \text{Dy}$ for gamma doses in the range of (a) 10 Gy to 500 Gy and (b) 1 kGy to 6 kGy

It is found on preliminary observation that the glow curves for gamma irradiation in the range of 10 to 100 Gy show only one prominent peak at $\sim 325^\circ\text{C}$. For 100-500 Gy, three extremely small peaks at approximately 100°C , 150°C and 225°C start showing up. For higher doses in the range of 1 kGy to 6 kGy, four peaks can be clearly observed: three minor low temperature peaks at the positions mentioned earlier while the major peak is found around 335°C . It can be clearly seen that at high irradiation doses, shallow traps start to contribute more towards TL intensity as compared to lower doses.

For UV irradiation it is found that there are only two visible peaks: a major peak at 340°C and a very small peak at around 100°C .

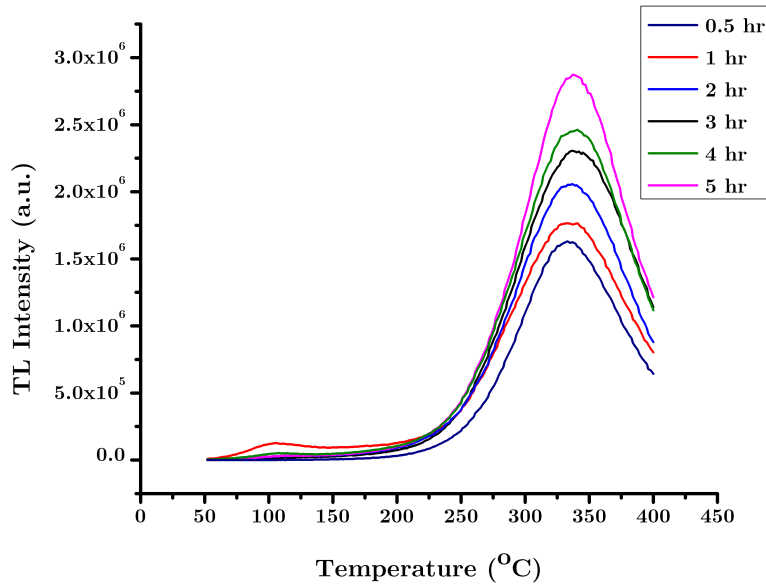


Figure 4.3: TL glow curves of $\text{Li}_3\text{PO}_4 : \text{Dy}$ for UV irradiation time ranging from 0.5 h to 5 h

4.3 Dose Response

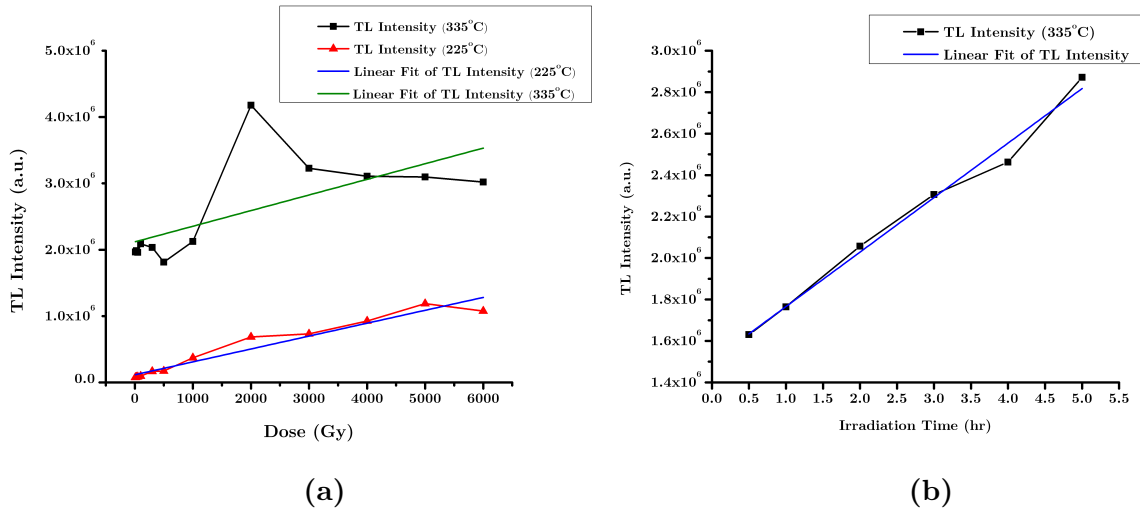


Figure 4.4: TL dose response of $\text{Li}_3\text{PO}_4 : \text{Dy}$ for (a) peaks at 225°C and 335°C when subjected to gamma irradiation and (b) peak at 335°C when subjected to UV irradiation

Figure 4.4a shows the dose response for the major peak (at 335°C) and one minor peak (at 225°C) for gamma irradiation doses in the range of 10 Gy to 6 kGy. It is found that the peak at 225°C shows excellent linear behaviour upto 5 kGy and a small dip at 6 kGy.

This is confirmed by the R^2 value of the fit which comes to be 0.97184, i.e very close to 1. However for the high temperature peak, a very erratic behaviour is observed. The TL intensity shows a dip at 500 Gy, then rises sharply upto 2 kGy and then drops at 3 kGy and further continues to decrease gradually upto 6 kGy. A plausible explanation for the sublinearity beyond 2 kGy is that there might be a preferential radiation damage of the deeper trap at high irradiation doses. This reduces the trapping efficiency of such traps, thereby leading to lower TL intensity than is expected, as shown in a study on non-linearity in dosimeters [62]. Further, as the peak occurs at high temperature, the blackbody radiation component and the effect of thermal quenching (decrease in TL intensity at high temperatures) [63] may in part explain the irregular dose response shown by the major peak.

The dose response of the same phosphor when irradiated by UV rays (irradiation time from 0.5 h to 5 h) is shown in Figure 4.4b. In this case it is observed that the peak at 335°C shows a linear response upto the measured irradiation duration of 5 h. A high R^2 value of 0.98212 is found from the linear regression analysis.

4.3.1 Deconvolution and Calculation of Kinetic Parameters

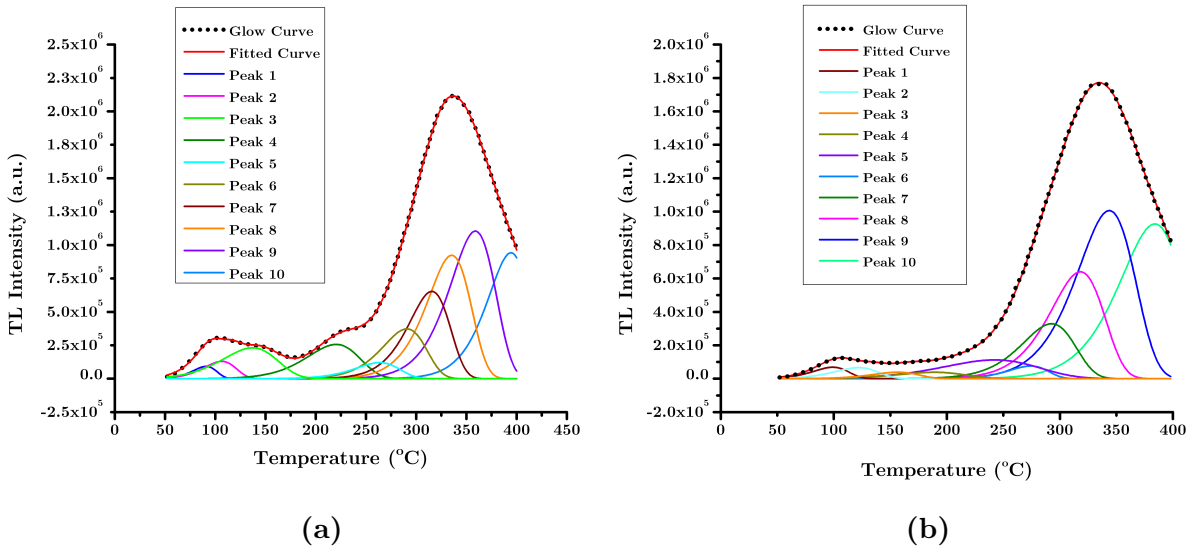


Figure 4.5: Deconvoluted peaks of $\text{Li}_3\text{PO}_4 : \text{Dy}$ for (a) 1 kGy dose of gamma exposure (b) UV irradiation at 254 nm for a duration of 1 h

Using the computerised glow curve deconvolution method, the glow curves were fitted and the constituent peaks were identified. The deconvoluted peaks for a gamma irradiation dose of 1 kGy are shown in Figure 4.5a and those for a UV irradiation time of 1 h

are displayed in Figure 4.5b. For both gamma and UV glow curves, 10 constituent peaks were identified. This is contrast with preliminary observations, in which only four peaks were found for gamma irradiation and two peaks for UV irradiation. Therefore, the glow curve deconvolution recovered a number of hidden peaks which could not be identified only by qualitative observations.

For the fitted curves, Figure of Merit (FOM) values of 0.0072 and 0.0057 were obtained for 1 kGy of gamma exposure and 1 h of UV exposure respectively. Both these values indicate that a good fit was achieved for both the glow curves.

Similar to the previous study, trap parameters were calculated for all the constituent peaks present in the glow curves using the Chen's peak shape method. The peak temperature (T_m), geometrical shape factor (μ_g), order of kinetics (b), frequency factor (s) and activation energy (E) are given for gamma irradiation dose of 1 kGy in Table 4.1. The same values for peaks corresponding to UV irradiation for 1 h are given in Table 4.2.

Table 4.1: Kinetic parameters of the deconvoluted peaks of $\text{Li}_3\text{PO}_4 : \text{Dy}$ for 1 kGy dose

Peak	Peak Temperature $T_m(^{\circ}\text{C})$	Geometrical shape factor μ_g	Order of Kinetics b	Frequency Factor $s(\text{sec}^{-1})$	Activation Energy $E(\text{eV})$
1	90.8	0.419	1.0	6.060×10^{12}	0.9291
2	106.4	0.423	1.0	5.248×10^9	0.7482
3	137.1	0.434	1.0	4.815×10^5	0.5
4	220.3	0.428	1.0	2.031×10^7	0.7585
5	263.7	0.422	1.0	5.854×10^9	1.0787
6	290.7	0.421	1.0	3.329×10^{10}	1.2163
7	315.6	0.419	1.0	6.281×10^{11}	1.4157
8	335.4	0.419	1.0	3.085×10^{11}	1.4290
9	358.9	0.419	1.0	2.626×10^{11}	1.4777
10	394.4	0.420	1.0	2.127×10^{13}	1.8082

For the glow curve corresponding to gamma dose of 1 kGy, it is found that all the separated peaks follow first order kinetics. Also, it can be seen that the shallower traps (those having smaller values of activation energy) occur at lower temperatures while the deeper traps are found at high temperatures (beyond 260°C). This is because the shallower traps can be excited by providing less amount of thermal energy and this corresponds to heating at low temperatures, while the deeper ones need more thermal energy and hence give TL glow at high temperatures.

Table 4.2: Kinetic parameters of the deconvoluted peaks of $\text{Li}_3\text{PO}_4 : \text{Dy}$ for 1 h of UV irradiation

Peak	Peak Temperature $T_m(^{\circ}\text{C})$	Geometrical shape factor μ_g	Order of Kinetics b	Frequency Factor $s(\text{sec}^{-1})$	Activation Energy $E(\text{eV})$
1	99.1	0.423	1.0	5.17×10^9	0.7328
2	121.9	0.426	1.0	1.73×10^8	0.6694
3	156.7	0.425	1.0	2.91×10^8	0.7495
4	189.2	0.433	1.0	8.59×10^5	0.5895
5	242.3	0.441	1.1	1.79×10^4	0.5023
6	274.2	0.417	1.0	1.23×10^{13}	1.4483
7	292.6	0.422	1.0	4.68×10^9	1.1288
8	318.1	0.422	1.0	1.10×10^{10}	1.2235
9	343.7	0.423	1.0	4.48×10^9	1.233
10	384.1	0.423	1.0	2.61×10^9	1.2878

It is found that all the constituent peaks of the glow curve corresponding to UV irradiation for 1 h also exhibit first order kinetics. Further the peaks with lower activation energy are found at lower temperatures upto $\sim 242^{\circ}\text{C}$ and those with comparatively higher activation energies at temperatures above 270°C due to the reason explained above.

4.4 Conclusion

In this study, the phosphor Li_3PO_4 was synthesized by a three step solid state diffusion technique using different concentrations of the dopant, Dy and its thermoluminescence properties were studied. It was found that the phosphor gives maximum TL intensity at 0.2 mol % concentration for both UV and gamma irradiation. For gamma irradiation, it was found that the high temperature peak shows an irregular non linear dose response while the peak at around 225°C showed good linearity upto a dose of 5 kGy. For UV irradiation, the high temperature peak at 335°C also showed linearity through the full range of irradiation time from 0.5 h to 5 h. Finally, through glow curve deconvolution, 10 constituent peaks were identified for both gamma and UV irradiation and all of them are found to follow first order kinetics.

Chapter 5

Future Prospects

In the present work it was shown that this novel phosphor, $\text{Li}_3\text{PO}_4 : \text{Dy}$ when synthesised by the co-precipitation method and solid state diffusion method exhibited some good TL properties for application in radiation dosimetry. This includes presence of traps at high temperatures, excellent linearity for the dosimetric peaks and the tissue equivalence of this material. In the light of this promising evidence, it would be of interest to further study the repeatability and fading of this phosphor which would be conclusive in deciding whether it can be used as a reliable dosimeter, especially in medical applications.

Also, the dose response of this phosphor can be studied for other types of irradiation such as by proton beams or by ^{16}O and ^{12}C ion beams which are being used in ion beam radiotherapy. In recent years, this field has amassed great attention as these ion and proton beams deposit a larger fraction of their dose at certain depth after entering the body, therefore selectively targeting the cancerous growth without causing much damage to surrounding healthy tissues [64, 65]. This is in contrast with conventional X-ray radiation which delivers most of its dose as soon as it enters the body. This phosphor, due to its tissue equivalence may serve as a phantom that imitates the response of body tissues to such irradiation. An ion beam dose deposition profile can then be analysed to find out what fraction of the dose is delivered at a particular depth in body tissues.

Further photoluminescence properties such as its PL emission and excitation spectra may be studied along with the analysis of its CIE (International Commission on Illumination) plot in order to assess its scope of applicability in white LEDs.

Bibliography

- [1] S. W. S. McKeever, in *Thermoluminescence of solids* (Cambridge University Press, May 1985), pp. 1–19.
- [2] A. Roda, in *Chemiluminescence and bioluminescence* (Royal Society of Chemistry, Cambridge, Oct. 2010), pp. 1–50.
- [3] R. Capelletti, *Luminescence*, Jan. 2017.
- [4] J. T. Randall, M. H. F. Wilkins, and M. L. E. Oliphant, *Proceedings of the Royal Society of London. Series A. Mathematical and Physical Sciences* **184**, 365 (1945).
- [5] J. T. Randall, M. H. F. Wilkins, and M. L. E. Oliphant, *Proceedings of the Royal Society of London. Series A. Mathematical and Physical Sciences* **184**, 390 (1945).
- [6] G. F. Garlick and A. F. Gibson, *Proceedings of the Physical Society* **60**, 574 (1948).
- [7] F. Daniels, C. A. Boyd, and D. F. Saunders, *Science* **117**, 343 (1953).
- [8] V. Pagonis and P. Truong, *Physica B: Condensed Matter* **531**, 171 (2018).
- [9] Y. M. Yang, Z. Y. Li, J. Y. Zhang, Y. Lu, S. Q. Guo, Q. Zhao, X. Wang, Z. J. Yong, H. Li, J. P. Ma, Y. Kuroiwa, C. Moriyoshi, L. L. Hu, L. Y. Zhang, L. R. Zheng, and H. T. Sun, *Light: Science and Applications* **7**, 1 (2018).
- [10] M. Fasoli, A. Vedda, M. Nikl, C. Jiang, B. P. Uberuaga, D. A. Andersson, K. J. McClellan, and C. R. Stanek, *Physical Review B - Condensed Matter and Materials Physics* **84**, 81102 (2011).
- [11] W. Arnold and H. Sherwood, *Journal of Physical Chemistry* **63**, 2 (1959).
- [12] A. J. Bos, *Materials* **10** (2017) 10.3390/ma10121357.
- [13] A. J. Bos, *Radiation Measurements* **41**, 45 (2006).
- [14] C. Furetta and G. Kitis, *Journal of Materials Science* **39**, 2277 (2004).
- [15] C. E. May and J. A. Partridge, *The Journal of Chemical Physics* **40**, 1401 (1964).
- [16] R. Chen and S. W. S. McKeever, in *Theory of thermoluminescence and related phenomena* (World Scientific, Sept. 1997), pp. 283–315.
- [17] S. W. S. McKeever, in *Thermoluminescence of solids* (Cambridge University Press, May 1985), pp. 205–252.

- [18] T. Rivera, *Applied Radiation and Isotopes* **71**, 30 (2012).
- [19] C. B. Palan, N. S. Bajaj, and S. K. Omanwar, *Bull. Mater. Sci* **39**, 1619 (2016).
- [20] C. B. Palan, N. Bajaj, A. Soni, M. Kulkarni, and S. Omanwar, *Rare Metals* **36**, 758 (2017).
- [21] A. K. Sahu, B. P. Kore, P. S. Chowdhary, V. Nayar, and S. J. Dhoble, *Luminescence* **29**, 58 (2014).
- [22] J. Sun, X. Zhang, Z. Xia, and H. Du, *Journal of Applied Physics* **111**, 013101 (2012).
- [23] “Chapter 31 - Non-Destructive Testing”, in *Instrumentation reference book (fourth edition)*, edited by W. Boyes, Fourth Edition (Butterworth-Heinemann, Boston, 2010), pp. 567–592.
- [24] Wikipedia contributors, *Ultraviolet — Wikipedia, the free encyclopedia*, <https://en.wikipedia.org/w/index.php?title=Ultraviolet&oldid=959067966>, [Online; accessed 27-May-2020], 2020.
- [25] A. V. Rane, K. Kanny, V. Abitha, and S. Thomas, in *Synthesis of inorganic nanomaterials*, edited by S. M. Bhagyaraj, O. S. Oluwafemi, N. Kalarikkal, and S. Thomas, Micro and Nano Technologies (Woodhead Publishing, 2018), pp. 121–139.
- [26] *Co-precipitation — Article about Co-precipitation by The Free Dictionary*, <https://encyclopedia2.thefreedictionary.com/Co-precipitation>, [Online; accessed 27-May-2020], 1970-1979.
- [27] D. Harvey, *Modern analytical chemistry* (McGraw-Hill, 1999).
- [28] K. N. Shinde and S. J. Dhoble, *Radiation Protection Dosimetry* **152**, 463 (2012).
- [29] P. Shewmon, *Diffusion in Solids* (Springer International Publishing, Cham, 2016).
- [30] W. H. Bragg and W. L. Bragg, *Proceedings of the Royal Society of London. Series A, Containing Papers of a Mathematical and Physical Character* **88**, 428 (1913).
- [31] J. P. Patel and P. H. Parsania, in *Biodegradable and biocompatible polymer composites*, edited by N. G. Shimpi, Woodhead Publishing Series in Composites Science and Engineering (Woodhead Publishing, 2018), pp. 55–79.
- [32] J.-W. Lee, T. Nakano, S. Toyosawa, Y. Tabata, and Y. Umakoshi, *Journal of the Japan Institute of Metals and Materials* **72**, 85 (2008).
- [33] P. Scherrer, *Nachrichten von der Gesellschaft der Wissenschaften zu Göttingen, Mathematisch-Physikalische Klasse* **1918**, 98 (1918).
- [34] G. Williamson and W. Hall, *Acta Metallurgica* **1**, 22 (1953).
- [35] S. Misture and R. Snyder, in *Encyclopedia of materials: science and technology*, edited by K. J. Buschow, R. W. Cahn, M. C. Flemings, B. Ilschner, E. J. Kramer, S. Mahajan, and P. Veyssi re (Elsevier, Oxford, 2001), pp. 9799–9808.

- [36] A. McClelland and M. Mankin, in *Optical measurements for scientists and engineers* (Cambridge University Press, Apr. 2018), pp. 110–188.
- [37] P. R. Griffiths and J. A. de Haseth, in *Fourier transform infrared spectrometry* (John Wiley & Sons, Inc., Hoboken, NJ, USA, Apr. 2007), pp. 19–55.
- [38] O. Tursunov, J. Dobrowolski, K. Klima, B. Kordon, J. Ryczkowski, G. Tylko, and G. Czerski, *World Journal of Environmental Engineering* **3**, 58 (2015).
- [39] K. Vernon-Parry, *III-Vs Review* **13**, 40 (2000).
- [40] J. I. Goldstein, D. E. Newbury, P. Echlin, D. C. Joy, C. E. Lyman, E. Lifshin, L. Sawyer, and J. R. Michael, “Introduction”, in *Scanning electron microscopy and x-ray microanalysis: third edition* (Springer US, Boston, MA, 2003), pp. 1–20.
- [41] D. A. Boiko, E. O. Pentsak, V. A. Cherepanova, and V. P. Ananikov, *Scientific Data* **7**, 101 (2020).
- [42] F. W. C. Boswell and G. D. Pappas, *Science* **142**, 686 (1963).
- [43] W. Commons, *File:scheme tem en.svg — wikimedia commons, the free media repository*, [Online; accessed 29-May-2020], 2015.
- [44] D. B. Williams and C. B. Carter, “The transmission electron microscope”, in *Transmission electron microscopy: a textbook for materials science* (Springer US, Boston, MA, 2009), pp. 3–22.
- [45] D. Sahoo, P. Dewan, P. Srivastava, A. Kohli, I. Sandhu, R. Kumari, D. Saroha, A. Guha, A. Tewari, and R. Singh, *Annals of Nuclear Energy* **105**, 240 (2017).
- [46] *Gamma irradiation chambers/blood irradiators*, <https://www.aerb.gov.in/english/regulatory-facilities/radiation-facilities/application-in-research/gamma-irradiation-chambers>, [Online; accessed 29-May-2020], 2017.
- [47] *Harshaw TLDTM model 3500 manual readers*, <https://www.thermofisher.com/order/catalog/product/3500TLDDS3/>, [Online; accessed 29-May-2020], 2020.
- [48] *Personal dosimetry laboratory*, <http://ins.en.ankara.edu.tr/personal-dosimetry-laboratory/>, [Online; accessed 29-May-2020], 2013.
- [49] M. S. Rasheedy, *Journal of Fluorescence* **15**, 485 (2005).
- [50] A. Delgado and J. M. Gómez Ros, *Radiation Protection Dosimetry* **96**, 127 (2001).
- [51] S. Basun, G. F. Imbusch, D. D. Jia, and W. M. Yen, *Journal of Luminescence* **104**, 283 (2003).
- [52] Y. S. Horowitz and D. Yossian, *Radiation Protection Dosimetry* **60**, 1 (1995).
- [53] C. Furetta, G. Kitis, and C.-H. Kuo, *Nuclear Instruments and Methods in Physics Research Section B: Beam Interactions with Materials and Atoms* **160**, 65 (2000).
- [54] M. Puchalska and P. Bilski, *Radiation Measurements* **41**, 659 (2006).
- [55] H. G. Balian and N. W. Eddy, *Nuclear Instruments and Methods* **145**, 389 (1977).

- [56] R. Chen, [Journal of The Electrochemical Society](#) **116**, 1254 (1969).
- [57] B. D. Cullity and S. R. Stock, in *Elements of x-ray diffraction* (Pearson, Harlow, United Kingdom, 2014), pp. 101–102.
- [58] M. Klähn, G. Mathias, C. Kötting, M. Nonella, J. Schlitter, K. Gerwert, and P. Tavan, [The Journal of Physical Chemistry A](#) **108**, 6186 (2004).
- [59] R. L. Frost, Y. Xi, R. Scholz, A. López, and F. M. Belotti, [Vibrational Spectroscopy](#) **66**, 69 (2013).
- [60] R. Chen, [Journal of Physics D: Applied Physics](#) **16**, L107 (1983).
- [61] D. L. Dexter and J. H. Schulman, [The Journal of Chemical Physics](#) **22**, 1063 (1954).
- [62] A. R. Lakshmanan, R. C. Bhatt, and S. J. Supe, [Journal of Physics D: Applied Physics](#) **14**, 1683 (1981).
- [63] Z. Liu, Y. Huang, X. Yi, B. Fu, G. Yuan, J. Wang, J. Li, and Y. Zhang, [Scientific Reports](#) **6**, 32033 (2016).
- [64] C. K. Ying, D. Bolst, A. Rosenfeld, and S. Guatelli, eng, [Journal of medical physics](#) **44**, 263 (2019).
- [65] O. Sokol, E. Scifoni, W. Tinganelli, W. Kraft-Weyrather, J. Wiedemann, A. Maier, D. Boscolo, T. Friedrich, S. Brons, M. Durante, and M. Krämer, [Physics in Medicine & Biology](#) **62**, 7798 (2017).

Topic of Dissertation Project: TERAHERTZ EMISSION BY BEATING TWO LASERS IN THE PRESENCE OF MAGNETIZED PLASMA VIA PONDEROMOTIVE NONLINEARITY

Student Details: Srishti Kunwar, B.Sc. (H) Physics, Semester VI, session 2020-21

Supervisor: Dr. Narender Kumar

Affiliation: Department of Physics, Sri Venkateswara College, University Of Delhi, Dhaula Kuan, New Delhi-110021

Introduction: Terahertz radiation emission has been in vogue for its applications in medical imaging, imaging of biological tissues, spectroscopy, explosive detection, material characterization, outer space communications, non-destructive testing etc. These radiations occur between high frequency microwaves and far infrared regions in the electromagnetic spectrum. However, these radiations require high conversion efficiencies and therefore, cannot be obtained using semiconductors, photoconductive antennas, or electro-optic crystals due to their breakdown limit. Different new techniques have been introduced to construct high power THz emitters, namely, coherent synchrotron radiation, coherent undulator radiation, and free-electron lasers. These emitters work on ultra-relativistic electron acceleration.

Methodology: The technique used in my work utilizes the beating of two Lasers in magnetized plasma in the presence of an ion-acoustic wave. Herein, the X-mode lasers exert a beat ponderomotive force on plasma electrons and impart them an oscillatory velocity with both transverse and longitudinal components in the presence of transverse static magnetic field present in the plasma. Phase- matching conditions need to be satisfied for resonance. The density perturbation in the plasma due to the Ion acoustic wave provides the necessary phase condition. Ion acoustic wave plays a significant role in compensating for the momentum mismatch in the nonlinear mixing process.

This oscillatory velocity couples with density ripples and produces a nonlinear current that resonantly excites the THz radiation. Ripples are the same as electron-ion density perturbations in plasma. The point to be noted is that the magnetized plasma already has been introduced to the ion-acoustic wave which gets excited to THz radiation.

The temporal and spatial density profile of laser pumps affect the generation of THz radiation.

The procedure followed here is only possible when the spot size of laser is greater than the wavelength of THz wave. Basically, the low frequency IAW is responsible for modulating the density of plasma and creating a time-varying periodic structure. This density modulation of plasma accounts for phase-matching. The strength of the magnetic field induced into plasma affects the yield of THz radiation generated via excitation due to resonance.

Objectives:

- To study the laser-plasma interaction theory.
- To develop the theoretical model of THz radiation generation when two free electron lasers are pumped into magnetized plasma coupled with density perturbation by pre existing ion acoustic wave.
- Analyzing the resultant normalized amplitude of THz generated with changing varying magnetic field.

Skills expected to be acquired:

- To conduct literature review and convey results of present work through scientific writing.
- To learn making analytical mathematical models and obtaining computational graphs using Desmos.

References:

- C. S. Liu, V. K. Tripathi and Bengt Eliasson 2019 "*High Power Laser-Plasma Interaction*"
- Strong terahertz radiation generation by beating of extraordinary mode lasers in a rippled density magnetized plasma, Prateek Varshney, Vivek Sajal, K.P. Singh, Ravindra Kumar, and Navneet K. Sharma, *Laser and Particle Beams*, Volume 31, Issue 2, June 2013, pp. 337 - 344
- R. P. Sharma and R. K. Singh, *Phys. Plasmas* 21, 073101 (2014).
- M. Kumar, L. Bhasin, and V. K. Tripathi, *Phys. Scr.* 81, 045504 (2010).
- V. L. Ginzburg, *The Propagation of Electromagnetic Waves in Plasmas* (Pergamon, New York, 1970).

List of Examiner for the Dissertation Viva-Voce:

1) Dr. Agam Kumar Jha

Department of Physics

Kirori Mal College

University of Delhi

Email id: agamjha_2001@yahoo.co.in; Tel: 9899392894

2) Dr. Bipin Singh Koranga

Department of Physics

Kirori Mal College

University of Delhi

Email id: bipinkmcit@gmail.com; Tel: 9990751460

3) Dr. Subhash Kumar

Department of Physics

Acharya Narendra Dev College

University of Delhi

Email id: subhashkumar@andc.du.ac.in; Tel: 9810926151

4) Dr. Indra Sen Ram

Department of Physics

Dyal Singh College

University of Delhi

Email id: indra77dsc@gmail.com; Tel: 9868655692

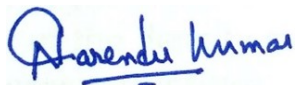
DISSERTATION PROJECT TITLE:

TERAHERTZ EMISSION BY BEATING TWO LASERS IN THE PRESENCE OF MAGNETIZED PLASMA VIA PONDEROMOTIVE NONLINEARITY

Student Details: Srishti Kunwar, B.Sc. (Hons.) Physics Semester VI, Session: 2020-21

Supervisor: Dr. Narender Kumar

Affiliation: Department of Physics, Sri Venkateswara College, University of Delhi, Dhaula Kuan, New Delhi-110021



Dr. Narender Kumar

Supervisor



Dr. K. C. Singh

Teacher-in-Charge

Topic of Dissertation Project: SUPERWASP Variable Stars: Cataloging and Identifying Rare Periodic Variable stars

Student Details: Aarushi Rawat, B.Sc. (H) Physics, Semester VI, session 2020-21 (INSPIRE Scholarship)

Supervisor: Dr. Anunay Kr. Chaudhary

Affiliation: Department of Physics, Sri Venkateswara College, University of Delhi, Dhaula Kuan, New Delhi-110021

Introduction: Stars are the building blocks of the baryonic universe. And a star's whose brightness seen from the Earth (i.e., its apparent magnitude) fluctuates is known as a variable star. Research on variable stars is important because it provides information about stellar properties, such as mass, radius, luminosity, temperature, internal and external structure, composition and evolution. This project aims to identify and classify the folded light curves of all objects with measured periods as either eclipsing binary stars, pulsating stars, rotationally modulated stars, or simply junk. Under the Zooniverse's Citizen Science project 'SUPERWASP VARIABLE STARS' one will be identifying large catalogues of objects of a similar type which can then be studied en masse to determine characteristics of the population. One can also aim to identify rare objects displaying unusual behavior, which can offer unique insights into stellar structure and evolution. SuperWASP is the world's most successful ground-based survey for transiting exoplanets – used wide – field robotic telescopes to continuously image the night sky. To make the light curves for each star, it uses brightness measurements from 10^5 stars per image, every few minutes, every night.

Methodology: The Zooniverse science platform contains data of about 2 million variable objects which can be attempted to identify and classify them. The light curves which are measurements of brightness as a function of time are provided. Analyzing each light curve on the basis of time period of folding and its shape of whether it is sinusoidal, our symmetric or have a larger increasing slope than decreasing slope one can classify these starts into various given categories. On coming upon unusual light curves, one could further analyze them to discover unusual variable objects.

Objectives:

- To study about variable stars and timing analysis of variable objects.
- Perform data analysis on large data sets and categorize and draw conclusions about the nature of variable objects in the night sky.

Skills expected to be acquired:

- To conduct literature review and convey results of present work through scientific writing.
- To learn data analysis and studying light curves how to extract information from them.

References:

- Thiemann, H.B., Norton, A.J., Dickinson, H.J, McMaster, A., Kolb, U.C, 2021, MNRAS, 502, 1299–1311
- www.imagine.gsfc.nasa.gov.com
- Variable Star Classification and Light Curves, An AAVSO course for the Carolyn Hurless Online Institute for Continuing Education in Astronomy (CHOICE)
- On the periods of variable stars by W.J. Miller

List of Examiner for the Dissertation Viva-Voce:

1) **Dr. Agam Kumar Jha**

Department of Physics

Kirori Mal College

University of Delhi

Email id: agamjha_2001@yahoo.co.in; Tel: 9899392894

2) **Dr. Bipin Singh Koranga**

Department of Physics

Kirori Mal College

University of Delhi

Email id: bipinkmcit@gmail.com; Tel: 9990751460

3) **Dr. Subhash Kumar**

Department of Physics

Acharya Narendra Dev College

University of Delhi

Email id: subhashkumar@andc.du.ac.in; Tel: 9810926151

4) **Dr. Indra Sen Ram**

Department of Physics

Dyal Singh College

University of Delhi

Email id: indra77dsc@gmail.com; Tel: 9868655692

DISSERTATION PROJECT TITLE:

SUPERWASP Variable Stars: Cataloging and Identifying Rare Periodic Variable stars

Student Details: Aarushi Rawat, B.Sc. (Hons.) Physics Semester VI, Session: 2020-21

Supervisor: Dr. Dr. Anunay Kr. Chaudhary

Affiliation: Department of Physics, Sri Venkateswara College, University of Delhi, Dhaula Kuan, New Delhi-110021

Dr. A.K Chaudhary
Supervisor

Dr. K. C. Singh
Teacher-in-Charge

Topic of Dissertation Project: ***“Investigation of optical properties of layered 2D materials i.e. MoS₂”***

Student Details: Lakshita Bageja, B.Sc. (Hons.), Physics - Semester VI, Session: 2020-21

Supervisor: Dr. Chandrabhan Dohare

Affiliation: Department of Physics, Sri Venkateswara College, University of Delhi, Dhaulta Kuan, New Delhi 110021

Introduction: Recently, there has been a growing interest in atomically thin two dimensional (2D) transition metal dichalcogenides (TMDC) i.e. MoS₂, for potential applications in next generation nano- and optoelectronic devices [1]. In particular, when TMDC thinned down to a monolayer, they become direct band gap semiconductors with large exciton binding energies which make them excellent candidates for various applications including ultrathin and flexible devices. TMDC switch over from an indirect band gap semiconductor at multilayer to a direct band gap at monolayer are sensitive in the visible frequency range and show strong optical absorption [2]. Recently, experiments have confirmed that molybdenum disulfide (MoS₂) has high electron mobility, making more appropriate for sensible devices.

For optoelectronic device applications of TMDC, spectroscopic ellipsometry (SE) is a powerful non-destructive technique to measure the optical properties of thin films. In SE, the wavelength dependent optical constants and the thickness of thin films can be determined by analyzing the change in the polarization state of the reflected light from the film surface and developing an optical dispersion model of the film material [3].

Reports on high quality transition metal dichalcogenides (i.e MoS₂) and the studies of its optical properties have been limited. Therefore, we have intended to investigate the optical properties of MoS₂.

Objectives:

The concept of mentioned summary in term of aim or object is specified as: -

- (1) Synthesis of MoS₂ (TMDs) thin films by *chemical vapour deposition* (CVD) technique
- (2) Study of *optical transition* using *spectroscopic ellipsometry* (SE)
- (3) Analysis of *Excitons* through *UV-Visible spectroscopy*

Methodology:

Synthesis of high quality large-size MoS₂ thin layer is still a challenge; however, chemical vapour deposition (CVD) has been one of the most realistic methods to synthesize. The sulfurization of Molybdenum (Mo) /MoO₃ on Si/SiO₂ substrate using the CVD method have been adopted to synthesize MoS₂. The optical analysis (optical transitions) would be done through Ellipsometry and UV-Visible spectroscopy.

Skills expected to be acquired:

- (1)** LaTeX software
- (2)** 'Easy Plot' for graph analysis
- (3)** 'ORIGIN' software for data analysis
- (4)** To conduct literature review and convey results of present work through scientific writing

References:

- [1]** Xingli Wang & Pulickel M. Ajayan et al., Chemical vapour deposition growth of crystalline monolayer MoSe₂, ACS Nano, 5 (2014) 5125.
- [2]** Di Xiao et al., Coupled Spin and Valley Physics in Monolayers of MoS₂ and Other Group-VI Dichalcogenides, Physical Review letter, 108 (2012) 196802.
- [3]** Chanyoung Yim, et al., Investigation of the optical properties of MoS₂ thin films using spectroscopic ellipsometry, Applied Physics Letters, 104, (2014) 103114.

List of Examiner for the Dissertation Viva-Voce:

1) Dr. Satya Prakash Yadav

Department of Physics, Acharya Narendra Dev College, University of Delhi

Email id: satyaprakashyadav@andc.du.ac.in

Tel: 9454105522

(2) Dr. Ajit Mahapatra

Department of Physics, University of Delhi

Email id: akm.nanolab.du@gmail.com

Tel: 9871074984

3) Dr. Indra Sen Ram

Department of Physics, Dayal Singh College, University of Delhi

Email id: indra77dsc@gmail.com

Tel: 9868655692

4) Dr. Agam Kumar Jha

Department of Physics, Kirori Mal College, University of Delhi

Email id: agamjha_2001@yahoo.co.in

Tel: 9899392894

DISSERTATION PROJECT TITLE: *"Investigation of optical properties of layered 2D materials i.e. MoS₂"*

Student Details: Lakshita Bageja, B.Sc. (Hons.), Physics -Semester VI, Session: 2020-21

Supervisor: Dr. Chandrabhan Dohare

Affiliation: Department of Physics, Sri Venkateswara College, University of Delhi, Dhoola Kuan, New Delhi 110021



Dr. Chandrabhan Dohare
(Supervisor)



Dr. K.C. Singh
(Teacher-in-Charge)